Development of an Iterative Irradiation Setup and Online Beam Monitor for Silicon Sensor Irradiation Studies

(Entwicklung einer Iterativen Bestrahlungsvorrichtung und eines Online-Strahlmonitors für Bestrahlungsstudien an Siliziumsensoren)

Master Thesis

by

Umut Elicabuk

Reviewer:	Prof. Dr. Thomas Müller	Institut für Experimentelle Teilchenphysik
Second Reviewer:	Prof. Dr. Ulrich Goerlach	Institut Pluridisciplinaire Hubert Curien
Advisor:	Dr. Alexander Dierlamm	Institut für Experimentelle Teilchenphysik
Second Advisor:	Dr. Stefan Maier	Institut für Experimentelle Teilchenphysik

Review and Declaration

This thesis has been accepted by the first reviewer of the master thesis.

Karlsruhe, 9 November 2021

_____

Prof. Dr. Thomas Müller

I declare that the work in this thesis was carried out in accordance with the requirements of the university's regulations and that it has not been submitted for any other academic award. Except where indicated by specific reference in the text, the work is the candidate's own work. Work done in collaboration with, or with the assistance of, others is indicated as such.

Karlsruhe, 9 November 2021

_____

Umut Elicabuk

Contents

Contents

1

Introduction

Collaboration of theory and experiment in the field of particle physics over the years culminated in a deep insight into nature's basic building blocks: the Standard Model of Particle Physics. The last missing piece of the particle puzzle has been found with the discovery of the Higgs boson in 2012. Necessary data was gathered with the ATLAS[1] and CMS[2] experiments at the CERN[3] *Large Hadron Collider* (LHC). Ever since the construction of the LHC, CERN's goal has been to discover new physics beyond the Standard Model. To accomplish this goal, until 2027, the LHC will be upgraded to the *High-Luminosity* LHC (HL-LHC). With the HL-LHC, the CERN collaboration aims to increase the luminosity of the machine which will increase the likelihood of the discovery of new physics phenomena and increase the precision on known processes.

As a consequence of the HL-LHC upgrade, the CMS detector has to be upgraded as well in order to cope with improved demands with regard to i.e. radiation exposure and granularity. During this *Phase-2 Upgrade*, CMS's whole silicon tracker has to be fully replaced. In order to characterize the effects of increased radiation exposure and development of radiation hard sensor designs, irradiation campaigns are performed. In these irradiation campaigns, test structures are irradiated with hadrons and annealing is performed.

The first setup presented in this thesis, the *Iterative Irradiation Setup* (IIS), aims to reproduce the annealing and irradiation scenario that will be faced at the real CMS experiment. Past irradiation studies pursued the concept of consecutive annealing scenarios, where the silicon sensor under test is irradiated to a target fluence and the effects of annealing are studied consecutively, post-irradiation. An approach that models the real CMS measurement scenario more closely is accomplished by usage of the IIS, where the sensor is iteratively irradiated and annealed. Section 5.1 will introduce the concept of the iterative irradiation scenario and compare it to consecutive annealing plans. Chapters 5 and 6 will discuss the development of the design and concept validation of the setup as well as experimental results that have been collected during the course of a beam test.

The second setup that will be discussed in this thesis is an online beam monitoring device that is intended for the use at irradiation facilities. Past experiences with regard to current stability during irradiation procedures have emphasized the need for non-destructive online beam monitoring. While various possibilities are eligible to accomplish this goal, this thesis pursues the usage of an air ionization chamber with consecutive amplification and digitization of the amplified signal. Chapter 9 describes the design process and the concept validation of this setup, while chapter 10 discusses obtained experimental data at two different irradiation facilities where X-ray and proton irradiations have been carried out.

Machines, systems, software and irradiation facilities that were used in this thesis are described in chapter 3. A more detailed description of the LHC, the CMS experiment as well as its Phase-2 Upgrade can be found in chapter 2. Theoretical concepts of particle detection with silicon and gas detectors are elaborated in chapters 4 and 8.

---

[1]**A T**oroidal **LHC A**pparatu**s**
[2]**C**ompact **M**uon **S**olenoid
[3]french: **C**onseil **E**uropéenne pour la **R**echerche **N**ucléaire (European Organization for Nuclear Research)

The Large Hadron Collider and the Compact Muon Solenoid Experiment
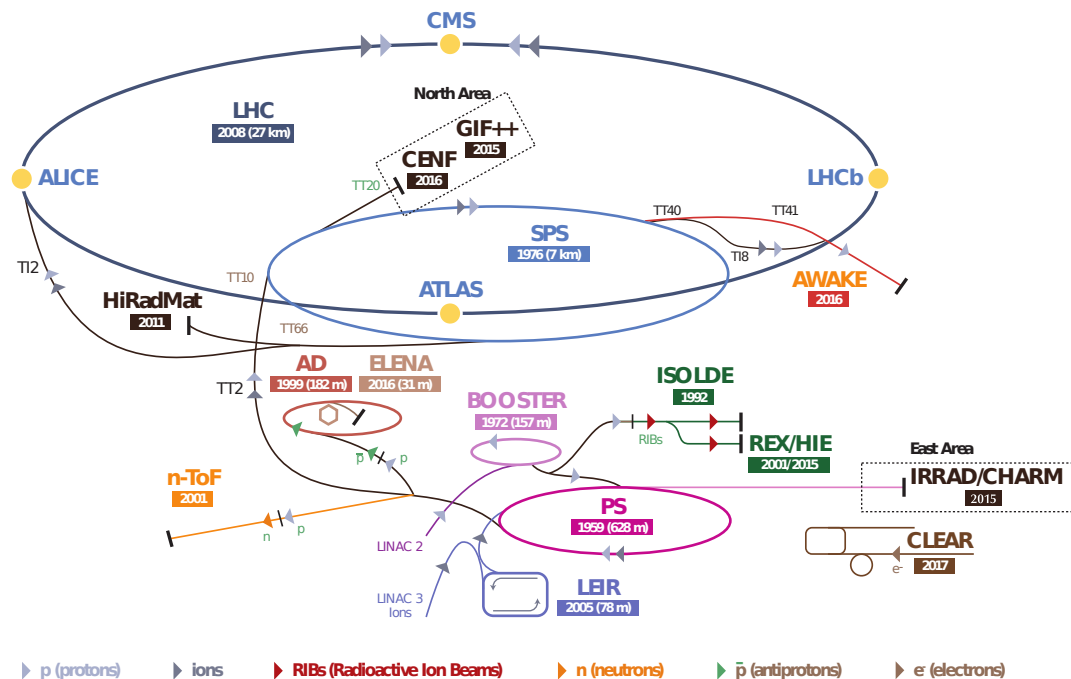
Figure 2.1.: Schematic view of the CERN accelerator complex. Protons are injected into the Linear Collider 2 (LINAC 2). After passing three circular accelerators (BOOSTER, PS and SPS), the protons are injected into the LHC [Mob19].

This chapter introduces the Large Hadron Collider (LHC) and the Compact Muon Solenoid Experiment (CMS). The work done in this thesis deals with research and development concerning these subjects.

2.1. The Large Hadron Collider

The LHC is the biggest particle accelerator known to mankind. It is part of the accelerator complex at the *European Organization for Nuclear Research* (CERN), located 100 m deep under the borders of France and Switzerland, nearby Geneva. The construction of the accelerator complex was completed in the late 1980s.

In contrast to its predecessor LEP (*Large Electron-Positron Collider*), the LHC does not accelerate electrons and positrons but two beams of protons or heavy ions. It consists of a storage ring with a circumference of roughly 27 km. Two bunched beams are accelerated along

two beam pipes in opposite directions. Each proton beam is accelerated to an energy of up to 7 TeV.

A schematic diagram of the CERN accelerator complex is shown in fig. 2.1. The protons necessary for the experiment are extracted from hydrogen atoms using an electric field. After extraction, the protons are injected into the Linear Collider 2 (LINAC 2) bunch-wise and begin their journey through the accelerator complex. In the last pre-accelererator, the SPS (**S**uper **P**roton **S**ynchrotron), the beams have already reached a kinetic energy of 0.45 TeV, which is sufficient for injection into the LHC. After acceleration in the LHC, the bunches collide at a center of mass energy of up to $\sqrt{s} = 14$ TeV.

The bunches are collided in a controlled manner at so-called *interaction points* (IP). All major experiments are located at these IPs. In total, there are seven experiments. The four biggest experiments are ATLAS, ALICE, LHCb, and last — but not least — CMS, which is the subject of this thesis.

Apart from the center of mass energy $\sqrt{s}$, a very important quantity describing the performance of a particle collider is the instantaneous luminosity $\mathcal{L}$. It is a measure for the rate of collisions $\mathrm{d}R/\mathrm{d}t$ at a fixed cross section σ_P of a process P

$$\frac{\mathrm{d}R}{\mathrm{d}t} = \mathcal{L} \cdot \sigma_\mathrm{P}.$$

For a circular particle collider, it holds that

$$\mathcal{L} = f \cdot \frac{N_1 N_2 N_\mathrm{b}}{4\pi \sigma_x \sigma_y},$$

where N_1 and N_2 denote the number of particles per bunch, N_b is the number of bunches, f denotes the bunch crossing frequency and σ_x and σ_y are the beam cross sections in the x- and y-direction, respectively.

Integration of the instantaneous luminosity $\mathcal{L}$ over time

$$N_\mathrm{e} \propto L = \int \mathrm{d}t\ \mathcal{L}, \tag{2.1}$$

yields the (integrated) luminosity L, which is proportional to the number of events N_e. The typical unit of luminosity is the inverse femtobarn (fb^{-1}). Because of the relation in eq. (2.1), the (integrated) luminosity contains information about how many particles have passed through the detector.

2.2. The Compact Muon Solenoid Experiment

The CMS experiment is a general purpose particle detector that is suitable to discover all potential kinds of new physics the LHC might offer. The Higgs boson is one of its most important discoveries.

Particle detection is accomplished by the usage of different detector subsystems. The combination of all information gathered by each individual subsystem yields a complete picture of the event and reconstruction of all particles that are involved. This approach is called *particle flow*. The subdetectors are arranged in cylindrical layers around the beam pipe with the IP located in the center of the detector. Additional end caps at both sides of the barrel cover particles emitted in the forward and backward direction. A large, superconducting solenoid with a steel joke encompasses all subdetectors. A schematic overview over the detector is shown in fig. 2.2 [CMS18].
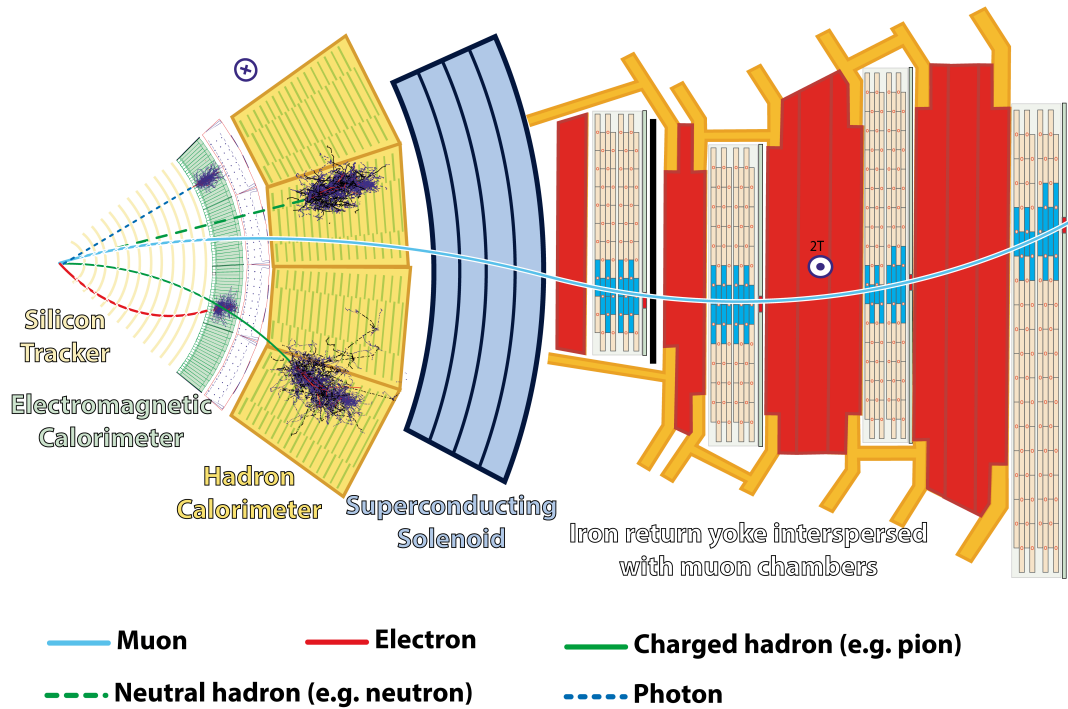
Figure 2.2.: Cross section of the CMS experiment. All subdetectors are annotated. Interactions and tracks of different particle types are shown by colored lines. Tracks of charged particles bend inside of the magnetic field, which allows for momentum reconstruction [CMS18].

The silicon tracker is located at the innermost region of the detector. It is used as a vertex detector. Trajectories of charged particles originating from the interaction point and secondary vertices are reconstructed.

The energy of particles interacting via the electromagnetic force is determined with the electromagnetic calorimeter (ECAL). Scintillating lead tungsten crystals produce light in proportion to the particle's energy.

Energies of hadrons are determined with the hadronic calorimeter (HCAL). The sampling calorimeter is made up of interleaved brass absorber plates and plastic scintillators shaped in a wedge-like manner.

Because most of the muons are minimum ionizing particles at energies encountered at the LHC, they need dedicated detection systems. Therefore, muons are detected in the so-called *muon chambers* located outside of the superconducting solenoid encompassing the other sub-detectors. A steel return yoke is incorporated inbetween the muon chambers to guide the magnetic field lines on the outside of the solenoid [CMS18].

2.3. The HL-LHC Upgrade

Investigating physics beyond the standard model and precision measurements require an increase in luminosity. To accomplish this, the LHC will be upgraded to the *High-Luminosity LHC* (HL-LHC) until 2027. All detector systems need to be able to cope with the increased radiation exposure, which requires them to be upgraded as well.

The main goal of the HL-LHC upgrade is to increase the rate, at which interactions happen. This is accomplished by narrowing down the beam cross section in x- and y-direction $\sigma_{x/y}$.
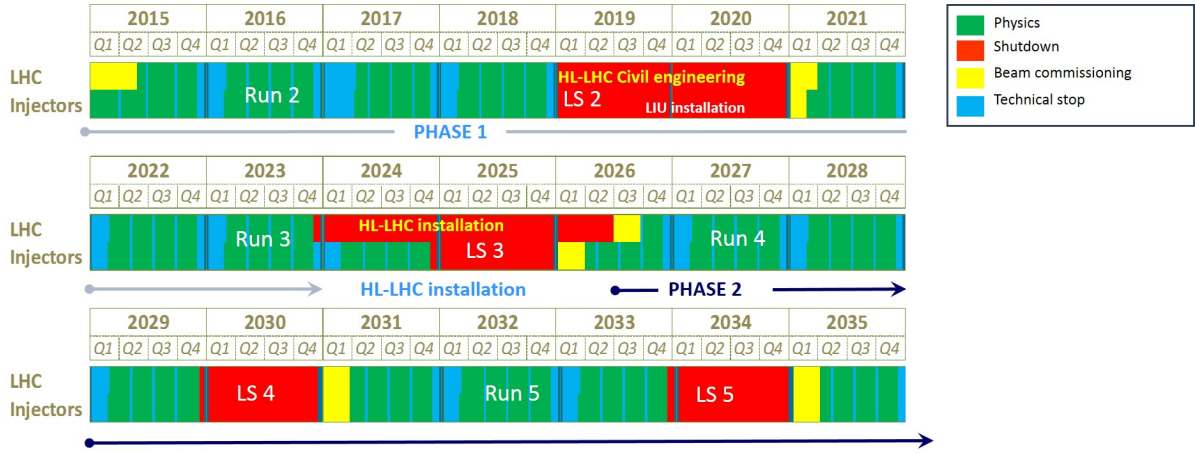
Figure 2.3.: Time table of the (HL)-LHC project until 2035. Between physics *runs*, either *technical stops* (TS) or *Long Shutdowns* (LS) represent measurement intermissions during which the upgrade of new detector (sub)systems is possible [CMS18].

By doing this, the instantaneous luminosity $\mathcal{L}$ increases fivefold, to a maximum value of $7.5 \times 10^{34}\,\mathrm{cm}^{-2}\,\mathrm{s}$ [CMS18].

Figure 2.3 shows a time schedule of measurement plans of the (HL)-LHC project. LS3 is planned to be used for main parts of the HL-LHC upgrade until 2027.

2.4. The CMS Phase-2 Outer Tracker

Currently, CMS's silicon tracker is built to withstand an integrated luminosity of $500\,\mathrm{fb}^{-1}$. Over the course of 10 years of runtime, an integrated luminosity of $3000\,\mathrm{fb}^{-1}$ is expected. Furthermore, the interaction rate increases to up to 200 collisions per bunch crossing. Increased demands to pattern recognition and granularity to keep the detector occupancy as low as 1% emerge. A low occupancy is needed to cope with increased pile-up [CMS18].

A central property that can be determined with the silicon tracker is the transverse momentum p_T of charged particles

$$p_\mathrm{T} = r \cdot q \cdot B,$$

which is dependent on the particle trajectory radius r, the electromagnetic charge q and the solenoid's magnetic field B. The p_T-modules of Phase-2 will make it possible to reduce data throughput by constraining the accepted trajectory radius for high momentum particles. They consist of either two consecutive strip sensors (2S) or one macro pixel and one strip sensor (PS). Apart from contribution to the level 1 trigger, binary signal readout will decrease data throughput and latency immensely [CMS18].

A schematic diagram of the tracker design that will be used in Phase-2 is shown in fig. 2.4. While the Inner Tracker consists of pixel modules, marked in yellow and green, the Outer Tracker consists of 2S and PS modules, marked in red and blue, respectively. Depending on their position in the CMS tracker, different radiation fluences for the modules are expected. CMS FLUKA[1] simulations estimate the radiation environment that is related to this deliberation. Figure 2.5 shows the expected fluences for the CMS tracker. These fluences were simulated at an integrated luminosity $3000\,\mathrm{fb}^{-1}$, a center of mass energy of $14\,\mathrm{TeV}$ and a total cross section of $\sigma_\mathrm{P} = 80\,\mathrm{mb}$. The fluences in fig. 2.5 are rounded and related to other sensor studies in [ABB20] to obtain the expected fluences with respect to regions of the Outer Tracker. They

---

[1] **Flu**ktuierende **Ka**skade (german for *fluctuating cascade*)
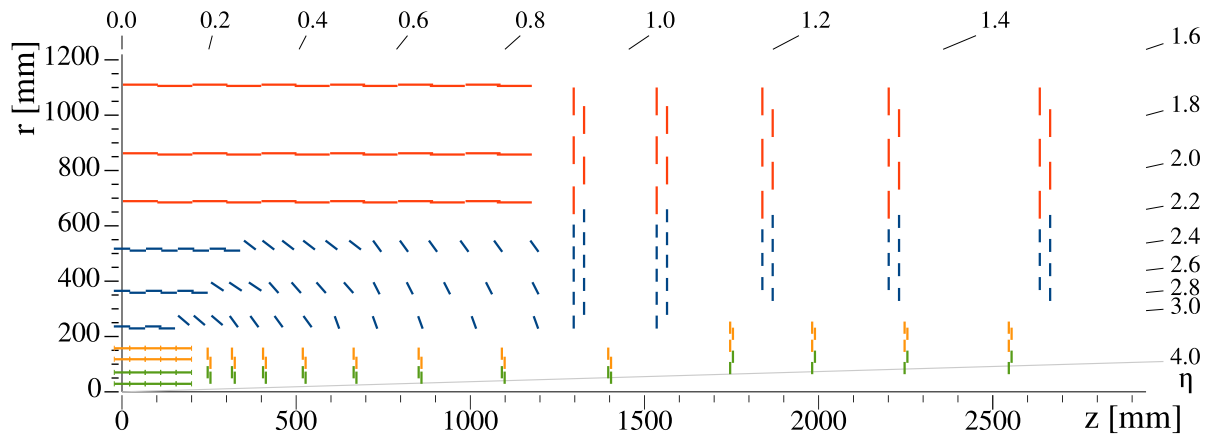
Figure 2.4.: Schematic illustration of the CMS Phase-2 tracker design. A quarter cross-section shows the modules arranged around the interaction point located at the origin. Silicon pixel modules of the Inner Tracker are marked in yellow and green. PS modules and 2S modules of the Outer Tracker are shown in blue and red, respectively [CMS18].
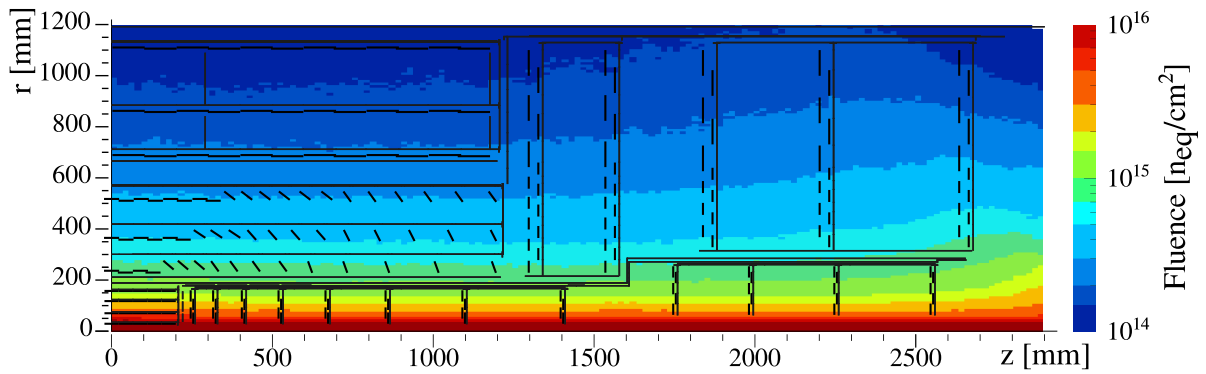
Figure 2.5.: Monte carlo simulation of expected particle fluences at an integrated luminosity of $3000\,\mathrm{fb}^{-1}$ [CMS18].

Table 2.1.: Overview over expected particle fluences at an integrated luminosity of $3000\,\mathrm{fb}^{-1}$ for regions of the Outer Tracker according to the FLUKA simulation shown in fig. 2.5.

region	neutrons ($10^{14}\ \frac{n_{\mathrm{eq}}}{\mathrm{cm}^2}$)	protons ($10^{14}\ \frac{n_{\mathrm{eq}}}{\mathrm{cm}^2}$)	total ($10^{14}\ \frac{n_{\mathrm{eq}}}{\mathrm{cm}^2}$)
min. inner	1	2	3
nom. inner	4	6	10
max. inner	5	10	15
min. outer	0.75	0.25	1
nom. outer	2.5	0.5	3
max. outer	5	1	6

are listed in table 2.1. Depending on the radial position inside of the tracker, the particle composition that contributes to the total fluence varies.

In order to remain efficient over the course of its runtime, the CMS tracker needs to be sufficiently radiation hard. This requirement needs to be met for the whole runtime of the detector. This can be accomplished by emplyoment of improved sensor designs and module topologies. Irradiation campaigns investigate properties of the sensors used in the CMS tracker with regard to radiation exposure. The work in this thesis focuses on this aspect of the Phase-2 upgrade.

Test Stations and Irradiation Facilities

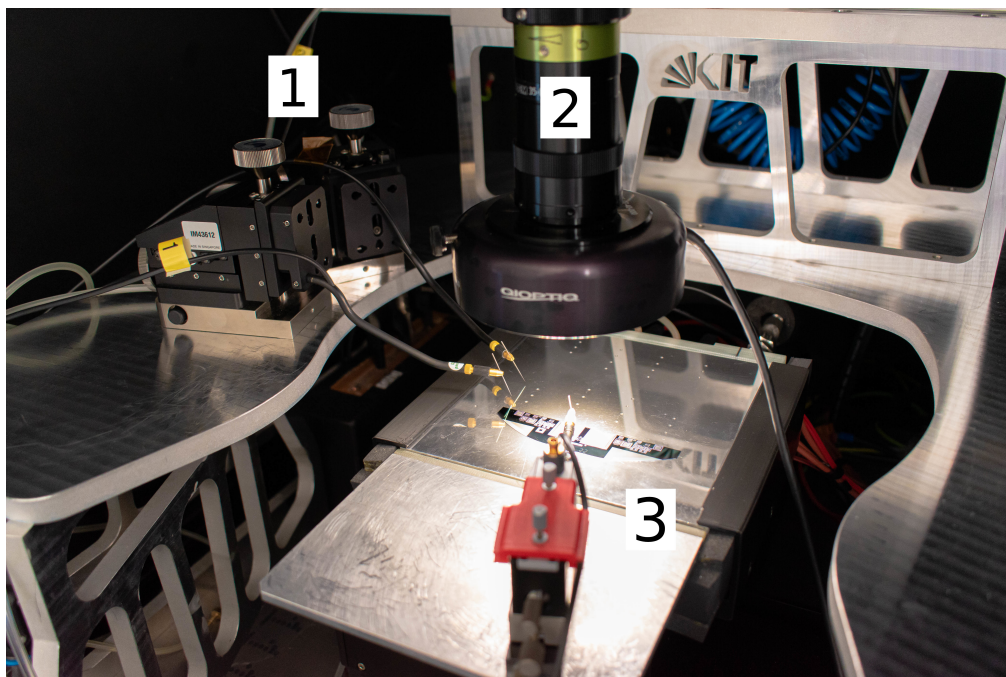**Figure 3.1.: A *probe station*.** 1: holder for strip needles, 2: high resolution binoculars with camera, 3: biasing chuck with bias needle holder

Many different software frameworks, hardware, test stations and irradiation facilities were used for the work in this thesis. They will be listed and explained in the following chapter.

3.1. Probe Station

The Institute of Experimental Particle Physics (ETP) provides two stations for electrical characterization of sensors. These so-called *probe stations* are able to semiautomatically measure IV (total leakage current over bias voltage), CV (total capacitance over bias voltage) and strip parameter curves. In fig. 3.1, an annotated illustration of such a probe station can be seen.

As established in section 4.4, sensors have to be measured inside of a dark environment to prevent photons from generating electron-hole pairs and falsify current measurements. Irradiated sensors have to be measured at a temperature of $T = -20\,°\mathrm{C}$ to prevent formation of dew on the sensor under test.

An important aspect of these measurements is a sufficiently light and air tight environment with sufficiently high cooling power and dry air inflow (for low temperature measurements, i.e. for irradiated sensors). It is only by following these standards that the dew point in the station can be adjusted to low enough values to make measurements at $T = -20\,°\mathrm{C}$ possible.
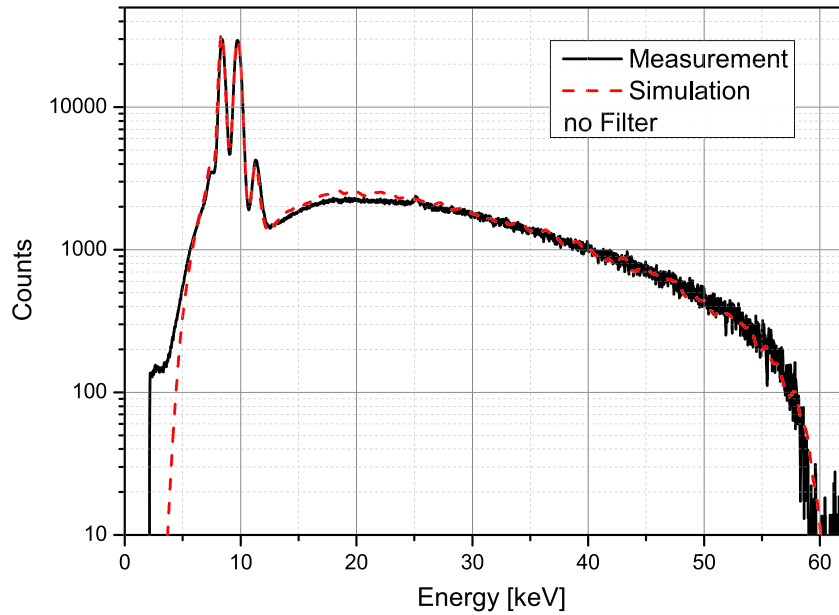
Figure 3.2.: Simulation and measurement of the tungsten X-ray tube spectrum at ETP for tube settings of 60 kV and 33 mA. Recorded from a distance of 155 mm [Gut+12].

The probe station chassis is made of aluminium that acts as a Faradey cage and protects the sensor from stray electromagnetic fields that could throw off any measurements.

Sensors to be characterized are held in place on an aluminium chuck via a vacuum. A negative high voltage is applied to the sensor back side via the aluminium chuck. Pads and rings on the sensor are contacted with micro needles that are connected to either a test voltage or ground. The sensor is biased by contacting the bias ring with a grounded *bias needle*.

Measurements of strip parameters are conducted by the use of two additional needles that contact either two neighboring DC pads or the DC and AC pad of one strip implant. High resolution stepper motors translate the aluminium chuck on 3 axes to enable strip scans.

The temperature of the aluminium chuck is controlled using Peltier elements mounted underneath it. A PID controller controls the voltage of said Peltier elements. Peripheral devices are placed outside of the probe station, cables are routed in via small inlets in the chassis.

3.2. X-Ray Setup

X-ray irradiations in this thesis are carried out with the tungsten X-ray tube that is present at ETP. It is located inside of an aluminium-lead interleaved housing, shielding the outside (and operator for that matter) from stray radiation. A kill switch that is connected to the housing lid closes the X-ray tube shutter when the lid is opened. This protects the user from radiation in case of human error.

Simulated and measured spectra for typical tube settings are depicted in fig. 3.2. Although filters can be inserted to suppress the low-energetic part of the spectrum, this has not been done for this work. X-ray tube specific adjustments, such as the tube voltage and current, beam spot size and distance to the collimator will be specified along with other measurement specific details in section 10.1.1.
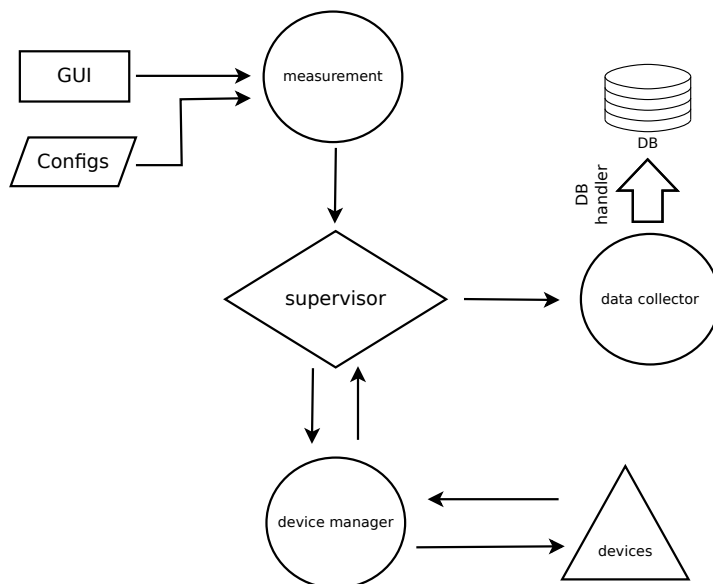
Figure 3.3.: Diagram of the MeasurementControl back end

3.3. MeasurementControl

A software package used at several measurement setups at ETP is the *MeasurementControl* (MC) back end. MC is a modular back end framework written in Python. A schematic diagram of the MC back end is shown in fig. 3.3. The central module that controls most of other modules is the *supervisor* module. The supervisor implements a finite state machine iterating over the internal data structure of the *measurement* module. Measurements are defined by specifying configuration files for any type of measurement that needs to be conducted.

Hardware that needs to be used for each measurement is interfaced by the *device manager* module. *Devices* may be added to the device manager by specifying them via configuartion files. The supervisor communicates with the device manager whenever a device needs to be accessed to conduct measurements.

Telemetry is saved via the *data collector* module to either a file, real-time plots or the the internal ETP database. Front ends may interface the MC back end via HTTP requests. Every module exposes HTTP endpoints for this purpose.

The MC framework has been presented in a vastly simplified version. For further information, please consider [Nür18].

3.4. The ALiBaVa Readout System

The following subsection introduces the LHCb Beetle chip and ALiBaVa readout system by ALiBaVa systems used for charge collection measurements of silicon strip sensors in this thesis [ALi21].

3.4.1. The Beetle Chip

The *Beetle readout ASIC* has been developed for usage at the LHCb experiment at CERN. It integrates 128 channels. Each channel consists of a programmable low-noise charge-sensitive preamplifier, an active pulse shaper and a subsequent current-buffer. A comparator discriminates the output pulse shape. Four adjacent comparator channels are ORed, multiplexed and routed off board via LVDS. The comparator output is sampled with the LHC bunch-crossing frequency
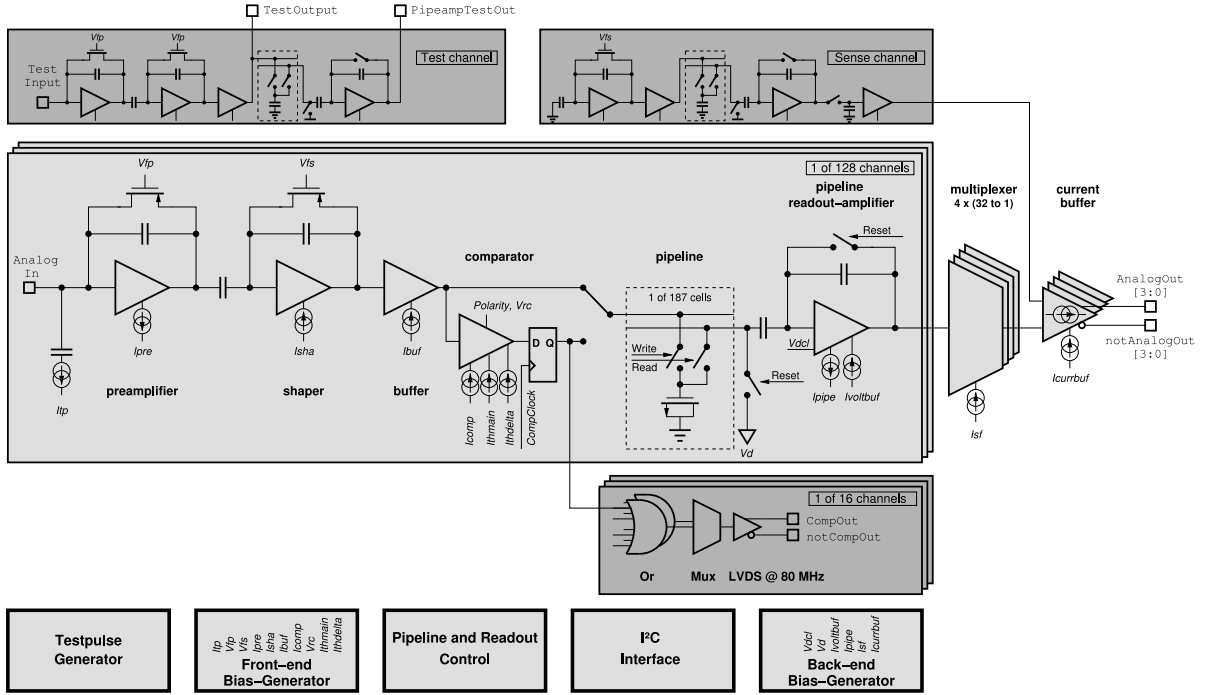
Figure 3.4.: Schematic block diagram of the *Beetle chip*. It integrates 128 channels, each equipped with charge-sensitive preamplifiers [LS06].

of 40 MHz into an analog pipeline with an adjustable latency of 160 sampling intervals. To account for common mode effects, the output of an unconnected dummy channel is subtracted from the analog data.

The equivalent noise charge is strongly dependent on internal Beetle chip parameters and the input capacitance of all channels. Additionally, variations from channel-to-channel occur and make it difficult to estimate an uncertainty on charge collection measurements. An estimation of 1000 e⁻ will be used for the uncertainty on cluster signals with reference to [Met20].

3.4.2. Data Acquisition

Data acquisition for charge collection measurements is done using the *ALiBaVa* readout system. The daughter board encorporates two beetle chips, totaling 256 analog readout channels.

The sensor to be examined is wirebonded to the beetle chips via fan-out pitch adapters and externally biased. A Sr-90 β-source is used to produce electron-hole pairs inside of the sensor and is mounted in front of it. Sr-90 undergoes pure β^--decay into Y-90 with a decay energy of 546 keV. The short-lived daughter nuclide decays with an end point energy of 2.2 MeV and, thus, represents a MIP source. Therefore, it may be used for charge collection measurements. When an ionizing particle traverses the sensor bonded to the ALiBaVa readout ASIC, the scintillator below the sensor triggers data acquisition. The adjusted latency value in combination with a fixed output buffer size defines an event.

Every channel is equipped with an internal charge injector with variable pulse height for calibration purposes. The ALiBaVa readout chip yields a signal in units of internal ADC counts. In order to calculate the conversion factor between this arbitrary unit into the physical signal in electrons, a so called calibration run is recorded. Depending on the input capacitance of the readout channels — which is dependent on i.e. wire bonding length and sensor size — different gain values are possible. Therefore, a calibration run is performed before every charge collection measurement. A known amount of charge is injected into all channel capacitances
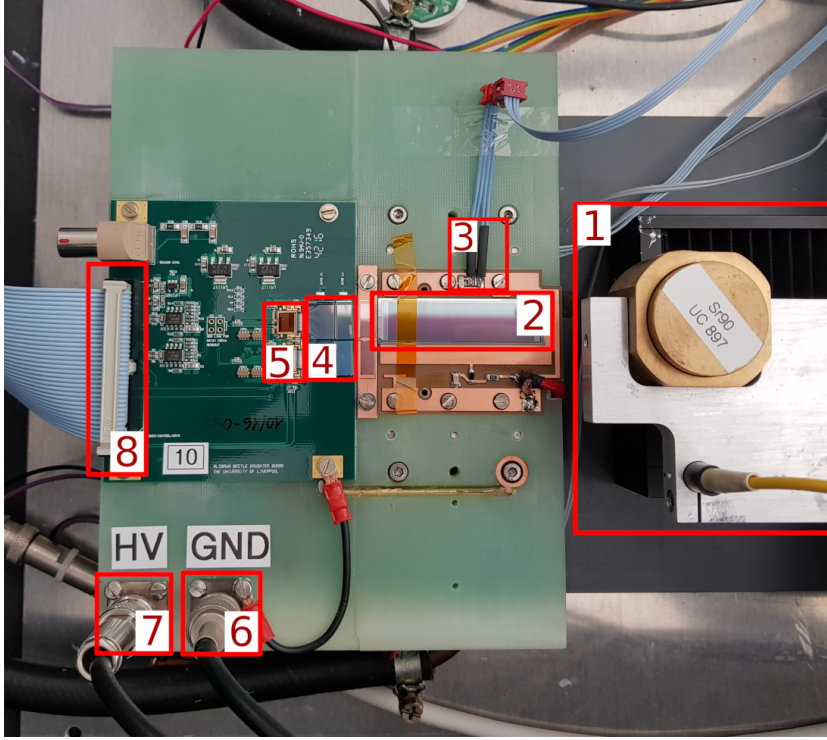
Figure 3.5.: The ALiBaVa station at ETP. 1: Controllable xyz stage holding the β-source, 2: sensor, 3: Pt1000 temperature sensor, 4: pitch adapater, 5: Beetle chip, 6 + 7: ground and HV connections, 8: flat ribbon cable connecting to the mother board

and discharged. A discharge time delay scan is performed. Its maximum yields the gain in electrons/ADC.

The read out analog data is digitized using a mother board connected to the daughter board via a flat ribbon cable and sent to a readout PC.

The ETP provides a station built solely for ALiBaVa charge collection measurements and is depicted in fig. 3.5.

3.5. ALiBaVa Analysis

In order to analyze digitized data of the ALiBaVa system, a dedicated software solution is needed. A self-written Python framework has been developed not only for this thesis but also for the sake of ALiBaVa data analysis at the ETP [EN20]. The necessity for clean and comprehensive code as well as ease of extensibility and maintenance are the main drivers of a modular structure. Individual parts of signal processing are located in dedicated modules.

When a charged particle passes through the sensor wirebonded to the readout ASIC, the corresponding signal can be divided into three distinct parts

$$\text{ADC}(i, k) = P(i, k) + CM(k) + S(i, k), \tag{3.1}$$

where

$\text{ADC}(i, k)$ denotes the total signal for a strip i in arbitrary ADC counts of an event with number k,

P is the pedestal noise,

CM denotes common mode noise and

S is the actual signal induced by the charged particle.

Pedestal noise values are recorded in a separate pedestal run by reading out at random times while no signal is injected. The pedestal value of each individual readout channel is an effective signal offset and is different for every channel.

Common mode affects all readout channels in the same way. It is mainly caused by external influences like stray EM fields. It can therefore — by definition — only be different from event to event, not from channel to channel.

By usage of this signal definition, the software extracts the physically relevant signal from each event using the `signal` module and clusters hits using a seeded clustering definition. Seed strips are defined as strips whose signal level is above a so-called *seed threshold*. Neighboring strips are defined as strips whose signal level is above a so-called *neighbor threshold*. These thresholds are calculated as multiples of the CM subtracted noise value with the respective factors denoted as *seed* and *neighbor* cuts. A cluster is made up of seeds and neighbors. Relevant cluster properties such as (total) cluster signals, sizes, noise and characterstic functions are obtained and depicted using the `clustering` and `plotting` modules respectively.

The `fitting` module is able to fit functions to the histograms obtained by the clustering algorithm. It is mainly used to obtain the best fit on cluster signal data using a Gauss convoluted Landau distribution (using `pylandau` [PHS14]). The `gain` module handles extraction of the gain value for each channel by means of fitting a polynomial function to the calibration curve, yielding its maximum value. The utility class `database` provides an easy way to upload analyzed data into the internal ETP database.

An typical, exemplary output plot is shown in fig. A.1.

3.6. The Karlsruhe Compact Cyclotron

The Karlsruhe Compact Cyclotron accelerates a proton beam to an energy between $18\,\mathrm{MeV}$ and $40\,\mathrm{MeV}$ at a maximum beam current of $100\,\mathrm{\mu A}$ [Fur05]. Primary uses of the facility include production of radioisotopes and irradiation of samples for research and development. An H^- ion source is used for generation of protons by accelerating H^- ions towards a stripping foil. The generated electron current in the stripping foil is proportional to the proton beam current which can be used to monitor the beam intensity at the location of the stripping foil. For irradiations in this thesis, a beam energy of $23\,\mathrm{MeV}$ and a beam current of $2\,\mathrm{\mu A}$ is adjusted. The same magnetic field can be used to extract the protons via beam lines and acceleration.

A scanning procedure is used for irradiation of samples as described in [Die03].

3.7. The CYRCé Cyclotron (Cyclotron pour la Recherche et l'Enseignement)

Most of the data presented in this thesis has been obtained by usage of the CYRCé cyclotron located in Strasbourg, France. It has been developed in order to produce radioisotopes, medical drug monitoring and medical applications but ultimately is suitable for general purpose applications [IPH14].

For the measurements in this thesis, the cyclotron accelerates a bunched proton beam to an energy of $23\,\mathrm{MeV}$ at an extraction frequency of $42.5\,\mathrm{MHz}$. At its maximal energy of $25\,\mathrm{MeV}$, the emittances have been measured to be between $\epsilon_x^{\mathrm{rms}} = 1.4(2)\,\pi\cdot\mathrm{mm\,mrad}$ to $3.03(22)\,\pi\cdot\mathrm{mm\,mrad}$ in horizontal direction and $\epsilon_y^{\mathrm{rms}} = 3.7(14)\,\pi\cdot\mathrm{mm\,mrad}$ to $5.96(16)\,\pi\cdot\mathrm{mm\,mrad}$ in vertical direction [Bou+19]. Therefore, the beam has a preferred oval beam profile.
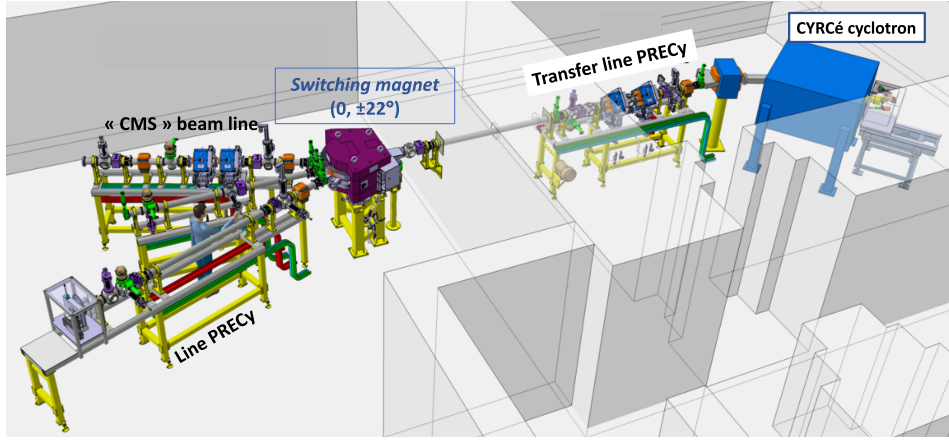
Figure 3.6.: Schematic illustration of CYRCé and its beamlines. Two beamlines are used for extraction, one of which is used in this thesis: the CMS beamline [Goe20].

With finely adjustable intensities of up to 120 nA, the provided beam allows for extraordinarily fine irradiation steps.

A dedicated *CMS beamline* has been built, servicing research connected to CMS. A fairly air and light tight irradiation box with aluminium profiles is used to mount the samples to be irradiated and the machinery to control said samples. Ionized air is sucked out of the box with a dedicated exhaust line. A beam dump made of tantalum is placed in forward direction of the beam, behind the sample. Patch panels at the side of the box allow for connection of all necessary electronic devices that need to remain outside. A schematic illustration of CYRCé and its beamlines is presented in fig. 3.6.

As is the case for the KAZ, a scanning procedure is used for irradiation of samples as described in [Die03].

3.8. Introduction to Finite Element Analysis for Thermal Simulations

Simulating the thermal performance of a given system is done by solving thermodynamical equations for the system. Depending on the complexity of the given system, numerous differential equations with vast parameter spaces have to be solved, which is unpractical and time-consuming. Instead, a geometry may be divided into a set of elements of finite size for which numerical approximations need to be found and a temperature needs to be computed at the vertex of every element.

Interpolation of temperatures among these so-called *nodes* gives an approximation of a geometry's total temperature field. This method is called *finite element analysis* (FEA).

There are mainly three different mechanisms of heat transfer, that need to be considered:

- **Thermal conduction** is the local transfer of vibrational energy within a body and occurs in all phases. According to the second law of thermodynamics, heat may flow from a warmer to the colder region of a body spontaneously. Thermal conductivity λ is used as a parameter to characterize the ability of a material to conduct heat. It is connects the heat flux density $\vec{q}$ with a temperature gradient ∇T in Fourier's law

$$\vec{q} = -\lambda \cdot \vec{\nabla} T.$$

- **Thermal convection** describes heat transfer in a body or bath by moving particles. Convection plays a dominant role in the heat transfer of gases i.e. in air. The transferred

heat per unit area is given by

$$J_{\text{heat}} = \alpha \cdot \Delta T,$$

where ΔT denotes the temperature gradient and α is called the *heat transmission coefficient* in W/m^2.

- **Thermal radiation** describes the loss of internal energy by emission of electromagnetic radiation. Since vibrational energy of all matter with a temperature greater than zero is non-vanishing, all matter emits thermal radiation. For bodies that are not black bodies, the *emissivity* ϵ characterizes their ability to emit energy in form of thermal radiation by their surface. The emitted spectral power law is given by

$$P(\nu) = \sigma A \cdot \epsilon(\nu) T.$$

The FEA needs to calculate the influence of these mechanisms on the system.

All steady-state thermal analyses presented in this thesis are performed using the *Ansys* software framework [Ans21].

Part I.

The Iterative Irradiation Setup

<div style="text-align: right; font-size: 4em; color: gray;">4</div>

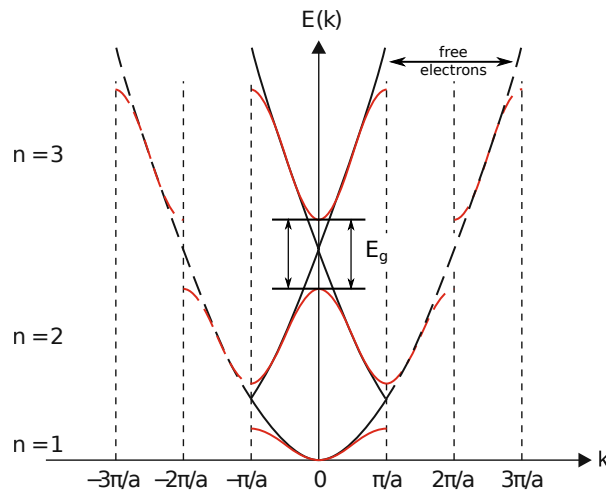# Theory of Particle Detection with Silicon Sensors

Figure 4.1.: Formation of the band structure. The quadratic dispersion relation is either lowered or raised at the edges of the first Briollouin zone, forming a zone with forbidden electronic states which is called the *band gap*. Picture abridged from [Dem16].

The following chapter will elaborate theoretical concepts behind particle detection using silicon sensor devices.

4.1. The Electronic Band Structure

The band theory offers an explanation to many physical properties of solids including, but not limited to, electrical conductivity. The formation of an electronic band structure can best be understood when considering a one-dimensional, periodic atomic lattice. Neglecting all electronic interactions, each electron inside such a lattice can be treated as free, leading to a quadratic dispersion relation

$$E(k) = \frac{\hbar \vec{k}_n^2}{2m},$$

where $\vec{k}_n$ denotes the n-th discrete momentum vector [Dem16].

Using standard quantum dynamics it is straight-forward to show, that there are two possible solutions for the electronic probability density function. In order to satisfy the Bragg condition, the parabolic dispersion relation is either lowered or raised at the edges of the first Brillouin zone, as can be seen in fig. 4.1. Consequently, a zone with forbidden electronic states, the so-called *band gap* is forming, separating the *valence band* (energetically) below from the *conduction band* above. Due to the large number of atoms inside a macroscopic solid, the

density of possible energy states is sufficiently high, hence justifying the assumption of a continuous energy *band* [Dem16].

The Pauli exclusion principle states, that no two fermions may occupy the same quantum-mechanical state. Obeying this principle, states within the bands are filled beginning from the ground state. Since electrons are fermions, they must obey *Fermi-Dirac statistics.* For the occupation probability $\overline{n_\lambda}$ of state λ with energy ϵ_λ and chemical potential μ, it holds that

$$\overline{n_\lambda} = \frac{1}{\exp\left(\frac{\epsilon_\lambda - \mu}{\mathrm{k_B} T}\right) - 1}. \tag{4.1}$$

At $T \to 0\,\mathrm{K}$, the energy of the last state that is occupied is called *Fermi energy* E_F with an occupation probability of $n\,(E_\mathrm{F}) = \frac{1}{2}$. Depending on the level of the Fermi energy, some bands are filled completely while others are occupied partly or not at all [Dem16].

Taking the low-temperature limit of eq. (4.1), $\overline{n_\lambda}$ approaches a Heaviside step function, strictly forbidding any states above the Fermi level to be occupied. However, for non-zero temperatures, electrons may occupy states above the Fermi level while some states below may not be occupied.

In this band model, electrical conduction is only possible, if a band is neither full nor empty, since electrons need to be mobile. The absence of an electron from a particular band is called a *hole*, representing an effective positive charge and therefore contributing to electrical conduction. Depending on the occupation of said bands, solids can be classified into three groups:

- **Isolators** with full valence bands and empty conduction bands. Isolators typically have a rather large band gap, preventing electrons to be excited into the conduction band by mere thermal excitations.

- **Semiconductors** with full valence bands and empty conduction bands. However, unlike isolators, semiconductors typically have a small band gap, making it possible to excite electrons into the conduction band by external energy input (such as light or temperature).

- **Metals** with full valence bands and non-empty conduction bands. Generally speaking, the valence and conduction bands of metals overlap. Therefore, electrons are easily excited into higher energy states, contributing to electrical conduction.

4.2. Doping of Semiconductors

An ideal atomic lattice, as it is described in section 4.1, is devoid of any unwanted features such as impurities or defects in the crystal structure. The reality, however, looks quite different. Taking these imperfections into account makes the physical description of macroscopic crystals vastly more difficult. Albeit complexification, impurities can be useful for many different aspects, such as electrical conduction. Artificially introducing foreign atoms into a semiconducting crystal lattice is called *doping* [Dem16].

Silicon provides a very useful example. With its four valence electrons, it crystallizes into a cubic diamond structure. Introducing foreign atoms from the third or fifth main group into its crystal structure changes its electrical properties.

If atoms from the third main group, such as arsenic, are used as dopants, silicon will become *p-doped*, as can be seen in fig. 4.2b. The vacancy resulting from a missing valence electron creates a hole in the electronic configuration of the crystal lattice. These so-called *acceptors* create allowed energy states in the vicinity of the valence band within the band gap.

If atoms from the fifth main group, such as phosphorous, are used as dopants, silicon will become *n-doped*, as shown in fig. 4.2a. Atoms with excess valence electrons become so-called *donors*, creating energy states in the vicinity of the conduction band within the band gap.
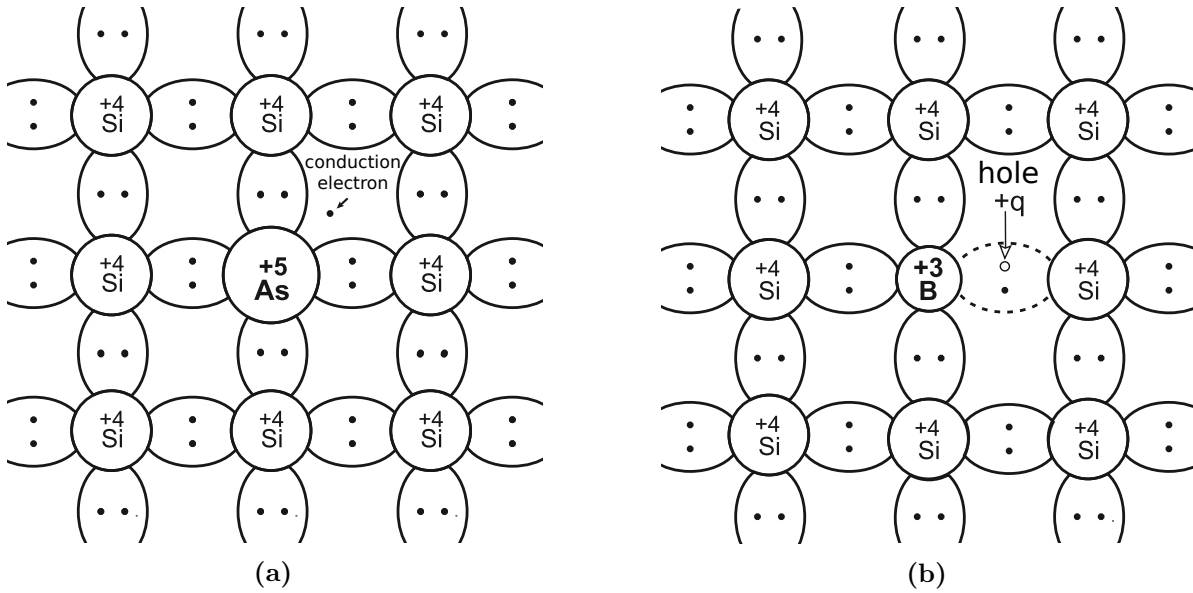
Figure 4.2.: Doping a silicon crystal. a) Arsenic is used as an n-dopant. b) Boron is used as a p-dopant. [KW16]
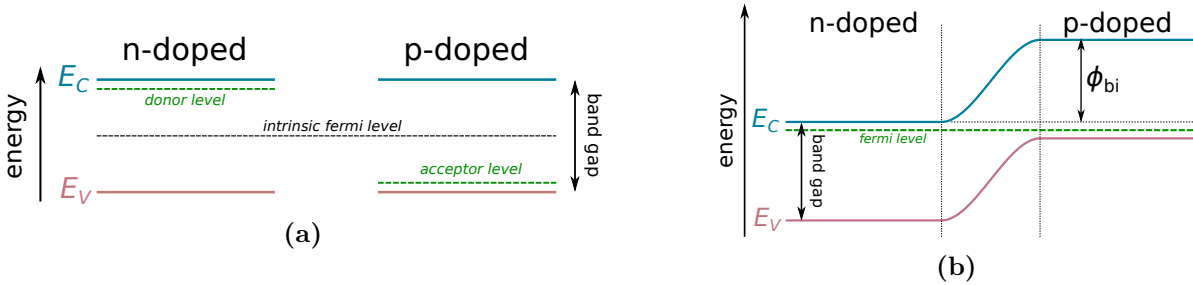

Figure 4.3.: Energy schema for a pn-junction. a) Band structure before contact of p- and n-doped materials. b) Band structure post-contact of p- and n-doped materials.

Typical doping concentrations for sensors used in this thesis are $n_A \approx 5 \times 10^{12}/\text{cm}^3$ for acceptors and $n_D \approx 1 \times 10^{19}/\text{cm}^3$ for donors. This means that for a sensor with a p-bulk and n-strips, the doping concentration of the strips is several orders of magnitude larger.

These new energy states are readily available for electrons from an energy band to be excited into. Compared to the band gap energy, a relatively small amount of energy is needed to accomplish this.

4.3. The pn-junction

The importance of doped materials becomes apparent when considering an n- and p-doped semiconductor in direct electrical contact, which is called a *pn-junction*. The simplest form of a pn-junction is called a *diode* and consists of exactly one junction. Figure 4.3b depicts an energy schema of such a pn-junction.

When p-doped and n-doped semiconductors are brought together, their respective majority charge carriers diffuse to the other side of the interface due to a concentration gradient. On the other side of the interface, holes from the p-doped side recombine with electrons from the n-doped side.

As a consequence of this diffusion, regions on the n-doped side in close vicinity to the interface now contain effective positive charge and vice versa. The region of recombination is called *space-charge region* or *depletion zone* because of its effective electrical charge and the absence of free charge carriers. Diffusion takes place until the opposing electric field is strong enough to establish an equilibrium state, in which the current caused by diffusion is opposed by the opposing field current. In silicon, the electric potential V_{bi} (*built-in voltage*) caused by this opposing field roughly amounts to 0.7 V.

The width of the depletion zone w can be increased or decreased by applying an external voltage to the pn-junction depending on its polarity. Applying a positive voltage to the p-doped side of the junction decreases the opposing field, the diode is operated in *forward direction.* The diode's resistance becomes low, allowing current to flow.

Applying a negative voltage to the p-doped side increases the opposing field, the diode is operated in *reverse direction.* Only a small flow of current is possible, which is called the *reverse leakage current.* It is caused by minority charge carriers being "pushed" through the depletion zone and thermally generated charge carriers. Solving Laplace's equation for this configuration yields the relation

$$w = \sqrt{\frac{2\epsilon}{q_0 \left| N_{eff} \right|} V_{bias}} \tag{4.2}$$

for the width of the depletion zone, where $\epsilon = \epsilon_0 \cdot \epsilon_{Si}$ denotes permittivity of the material and V_{bias} denotes the applied, external bias voltage. At a certain V_{bias}, the depletion zone permeates the entirety of the semiconductor. This voltage is called *full-depletion voltage V_{dep}*.

The quantity N_{eff} is called the *effective doping concentration* and is the difference between the concentration of ionized donors and acceptors within the space charge region. N_{eff} is an important quantity for sensor operation since it characterizes the full depletion voltage of the silicon bulk

$$V_{dep} = \frac{q_0}{2\epsilon} \left| N_{eff} \right| d^2,$$

where d denotes the width of the pn-junction which is equal to the width of the depletion zone in full depletion.

4.4. Interactions of Particles With Matter

The central idea of direct particle detection is to measure signals different particles generate by interaction with the measurement device. The following section will give an overview of different particle interaction mechanisms in matter.

4.4.1. Heavy, Charged Particles

Assuming that heavy, charged particles lose their energy by means of electromagnetic interactions with a medium's shell electrons, the *Bethe formula* provides an adequate description for the stopping power $-\left\langle \frac{dE}{dx} \right\rangle$ of charged particles in different media.

$$-\left\langle \frac{dE}{dx} \right\rangle = 4\pi N_A r_e^2 m_e c^2 \frac{Z z^2}{A} \frac{1}{\beta} \left(\frac{1}{2} \log \left[\frac{2 m_e c^2 \beta^2 \gamma^2 T_{max}}{I^2} \right] - \beta^2 \right), \tag{4.3}$$
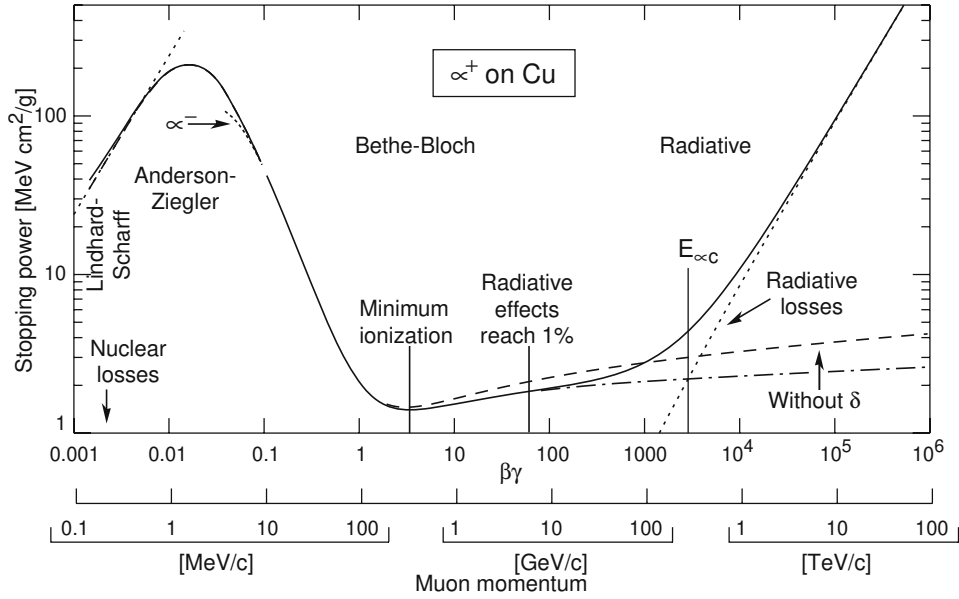
where

Figure 4.4.: Mean ionizing energy loss of muons in copper. The Bethe formula only applies for a certain part of this curve. For high and low energies, further corrections have to be made [Har17].

N_A is Avogadro's constant,

r_e is the classical electron radius,

m_e is the electron mass,

Z is the medium's atomic number,

z denotes charge of the incident particle,

A is the medium's mass number,

β denotes the relativistic beta factor,

γ is the Lorentz factor,

$T_{\max}$ denotes the maximum kinetic energy transferred in a single collision and

I is the mean excitation energy of the medium.

In eq. (4.3) it is assumed, that the incident particle loses its energy by multiple inelastic scattering processes, ionizing the atoms along its path. Per collision, the maximal kinetic energy that can be transferred to the medium is $T_{\max}$.

As an example, the mean energy loss of muons in copper is illustrated in fig. 4.4. The Bethe formula describes the mean ionizing energy loss with respect to the properties of the incident particle and the medium. It is valid for a projectile momentum ranging from $0.1 \leq \beta\gamma \leq 1000$. Particles with momenta around $\beta\gamma = 3$ deposit the least energy in the medium and, thus, are called *minium ionizing particles* (MIPs). For higher momenta, radiative losses like bremsstrahlung dominate over energy loss by ionization. For lower momenta, corrections due to nuclear losses have to be applied.

A good detector design has to be able to detect MIPs with a sufficiently large signal-to-noise ratio (SNR). Therefore, detector noise has to be significantly lower to ensure detection of said MIPs with sufficiently high confidence.

The energy loss by ionization, characterized by the Bethe equation, results in the generation of electron-hole pairs in silicon. As will be discussed in section 4.5, these electron-hole pairs can be separated by an electric field, which is used to detect a signal.

Equation (4.3) only describes the *mean* energy loss of heavy, charged particles. However, the statistical nature of ionizing energy losses allows for rather large fluctuations of a particle's
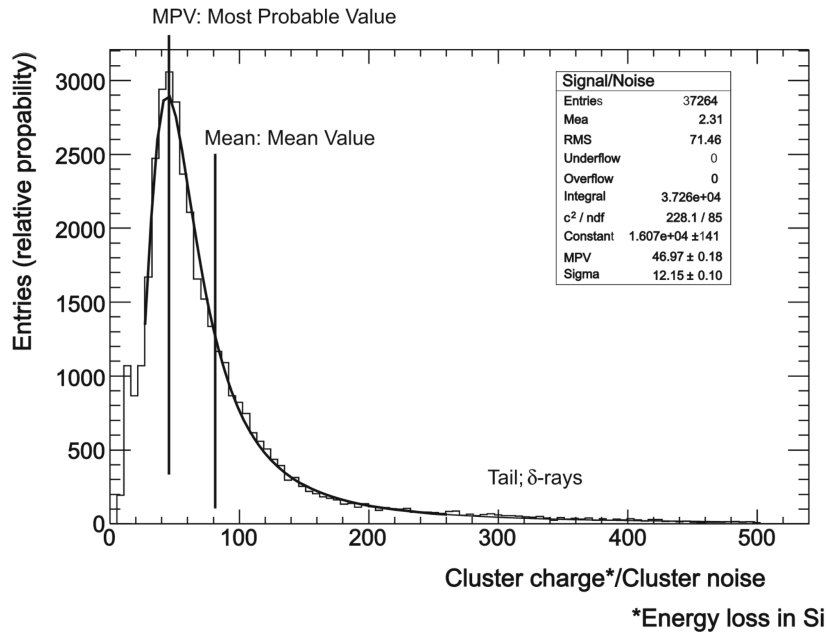
Figure 4.5.: Landau distributed signal in silicon. The *most probable value* (MPV) is about 30% lower than the average value of the distribution [Har17].

energy deposition. On one hand, the number of collisions of an incoming particle in a finite-sized medium varies. It can be modeled as a Poisson process.

On the other hand, the amount of energy deposited into the medium may vary. It can empirically be modeled by a Landau distribution, which takes δ-electrons into account. They are created by head-on collisions of the incident particle with the medium's shell electrons. As a consequence of the rather high energy deposition for head-on collisions, δ-electrons result in an asymmetry of the distribution for higher energies.

Taking these effects into account results in a *most probable value* (MPV) that is about 30% lower than the average value of the distribution [Har17]. An exemplary Landau distribution is shown in fig. 4.5.

4.4.2. Uncharged Particles and Electrons

As mentioned in section 4.4.1, charged particles may lose energy not only via ionization but also via radiation. The underlying process is called *bremsstrahlung*. Using classical electrodynamics, it is easy to show that the radiated energy is $\propto m^{-2}$. Therefore, bremsstrahlung only has a significant effect on particles with small masses, such as electrons.

As the gauge bosons of the electromagnetic interaction, photons can interact with matter in three different ways: The photoelectric effect, Compton scattering and pair production, each relevant in different momentum domains.

Pair production is relevant in the high momentum regime ($> 10\,\text{MeV}$) and produces two charged particles of opposite charge, each being able to lose energy radiatively. At high enough energies, these processes may cascade. This phenomenon is called *electromagnetic shower* and is used in electromagnetic calorimeters.

4.5. Working Principle and Fabrication of Silicon Strip Sensors

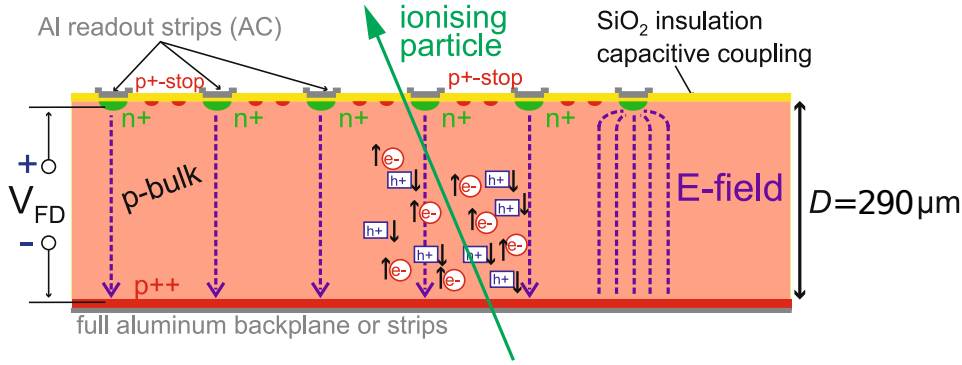The following section will introduce silicon as a detector material.

Figure 4.6.: An ionizing particle traversing a silicon strip sensor. The incident particle generates electron-hole pairs along its path through the sensor. For n-doped strips, electrons drift towards the readout strips and are detected as a signal. Graphic adapted from [Har17].

4.5.1. The pn-junction as a Detector

Depletion

When an ionizing particle traverses a silicon sensor electron-hole pairs are generated along its path. The average energy to create a single electron-hole pair in silicon I is 3.6 eV. With an average value of 387 eV/µm for energy loss in silicon, this amounts to roughly 108 eh/µm. Therefore, for a sensor with an active thickness of $d = 290$ µm, a single ionizing particle will induce a signal of around

$$N = \frac{\mathrm{d}E}{\mathrm{d}x} \cdot \frac{d}{I} \cdot \sigma_\mathrm{L} = 387 \, \frac{\mathrm{eV}}{\mathrm{µm}} \cdot \frac{290 \, \mathrm{µm}}{3.6 \, \mathrm{eV}} \cdot 0.7 = 21\,992 \text{ electrons,}$$

where the constant factor σ_L takes statistical Landau-distributed fluctuations into account. Comparing this to the number of free charge carriers at room temperature — which lies at about 10^{10} — it is easy to see that without intervention, the signal induced by incident particles would be superimposed by thermal noise [Har17].

There are two options to reduce the thermal noise in order to make practical use of the sensor: Either cool it down or operate a pn-junction sensor in reverse bias in order to deplete it of any thermally excited charge carriers. Cooling the sensor down to a cryogenic level is technically unfeasible, therefore, the second option is used in practice.

Signal Formation

The basic principle of a silicon strip sensor is demonstrated in fig. 4.6. Ionizing particles traverse a fully depleted, p-doped silicon bulk. Electron-hole pairs are generated along its path. Electrons drift towards the n-doped strips, following the electric field created by the bias voltage, while holes drift towards the backplane.

As established with eq. (4.2), the sensor needs to be operated at at least V_dep for the depletion zone to encompass the whole silicon bulk. As will be discussed in section 4.5.2, for a standard n-in-p strip sensor with an active thickness of 290 µm, this full depletion voltage V_dep lies at about 300 V. In practice, such sensors are operated at a bias voltage that is several hundreds of volts higher in order to ensure that

- full depletion is reached and

- the electric field is sufficiently high to enable a fast readout and sufficient signal height.
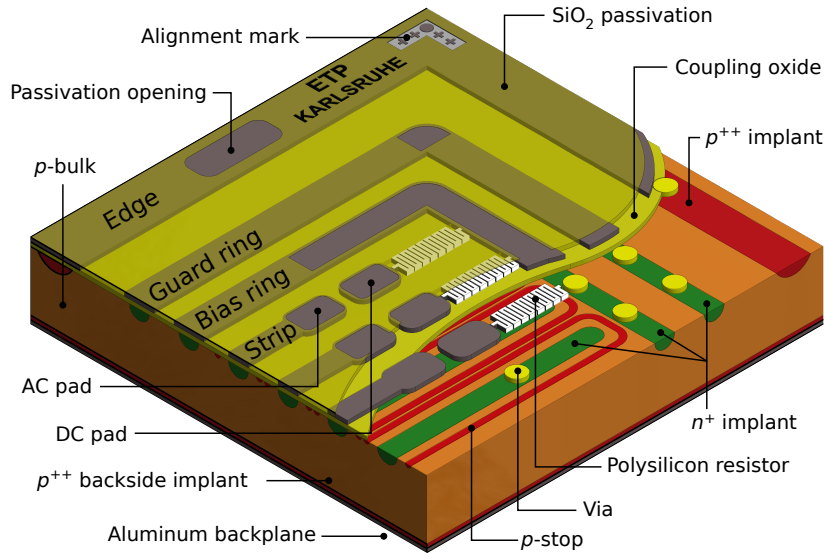
Figure 4.7.: An n-in-p silicon strip sensor. Polysilicon resistors connect DC pads to the bias ring. AC pads are AC coupled to the silicon strips and represent readout channels.

For a so-called *n-in-p* design, electrons are read out at n-doped strips at the top of the sensor. This electron signal is then amplified and shaped by a custom ASIC, which may also implement baseline corrections and analog-to-digital conversion. The concept of signal formation has first been established by Shockley and Ramo in the late 1930's [Sho38; Ram39]. Using classical electrostatics, it can be shown that the induced signal

$$i_{\text{sig}} \propto -q\vec{E}_{\text{w}} \cdot \vec{v}, \tag{4.4}$$

where $\vec{v}$ denotes the velocity vector of generated electrons. $\vec{E}_{\text{w}}$ is the so-called *weighting field*, which is dependent on detector geometry. According to eq. (4.4) and contrary to intuition, a signal is not measured when electrons reach the strips but rather *before* the charges reach the strips. This is due to induction caused by this drifting electric charge. As soon as the charges reach the strips, their velocity is zero and hence they do not induce any signal anymore.

4.5.2. The n-in-p Sensor Design

The technical implementation of deliberations established in section 4.5 is the n-in-p silicon strip sensor design. Figure 4.7 shows a schematic illustration of the design. Spatial resolution is accomplished by an arrangement of multiple parallel n-doped silicon strips embedded into a p-doped bulk all acting as multiple pn-junctions next to each other. Strip implants are connected to aluminium *DC pads* by *vias*. These DC pads are used to contact strip implants directly e.g. via probing needles for electrical characterization of the sensor. Polysilicon resistors connect the DC pads with a so-called *bias ring* which surrounds all strips.

An oxide layer separates the so-called *AC pads* from the strip implants. The AC pads are therefore AC-coupled to the strip implants by the dielectric's capacitance C_{ox}.

In order to electrically contact the back side of the sensor, it is coated with aluminium. Biasing the sensor works by applying a high negative voltage to the back side while grounding the bias ring. Highly p-doping the interface between bulk and aluminium backplane prevents formation of a Shottky barrier that would make it non-ohmic.

The bias ring is encompassed by a guarding structure called the *guard ring*. The guard ring ensures that all strips - including strips at the edge of the sensitive area - are on a defined and

homogeneous potential. It minimizes edge effects and for all measurements in this thesis **the guard ring is left floating**.

In practice, the DC-coupled DC pads can be used to directly probe the silicon strips using probing needles, which contact the pads. AC pads represent contacts for external readout circuitry in signal measurements.

Leakage Current

For a sensor made up of an ideal crystal lattice, as discussed in section 4.3, there should not be any measurable current. Under real conditions, however, there will always be a small current, which arises by thermally excited charge carriers. This current is called *leakage current* I_{leak}. Naturally, this leakage current

$$I(T_0, I_0, T) = I_0 \cdot \left(\frac{T}{T_0}\right)^2 \cdot \exp\left[-\frac{E_{\text{eff}}}{2k_{\text{B}}}\left(\frac{1}{T} - \frac{1}{T_0}\right)\right] \tag{4.5}$$

scales with temperature T, where

I_0 denotes the current flowing at a specific temperature T_0 and

E_{eff} is the effective band gap of $1.21\,\text{eV}$ for silicon [Chi13].

According to eq. (4.2), bulk leakage current also scales with the depth of the depletion zone. So it holds that

$$I_{\text{leak}} \propto \sqrt{V_{\text{bias}}}.$$

Real conditions are, once again, responsible for deviations from this behavior. Surface currents can significantly alter the course of the leakage current with respect to V_{bias}.

AC Coupling

An increasing leakage current leads to increasing noise which needs to be minimized in order to detect MIPs with sufficiently high confidence (see section 4.4).

To increase the SNR, as discussed in section 4.5.2, AC pads are AC coupled to the strip implants via an oxide layer acting as a dielectric. The high impedance path for lower frequencies effectively eliminates the DC component of all strip signals and therefore lowers the power input of subsequent amplifier stages.

Bulk Capacitance

Considering opposing sides of the space-charge region as plates of a capacitor, it is easy to see that

$$C(V_{\text{bias}}) = \begin{cases} A\sqrt{\dfrac{\epsilon}{2\rho\mu V_{\text{bias}}}}, & V_{\text{bias}} \leq V_{\text{dep}} \\ A\dfrac{\epsilon}{d} = \text{const.}, & V_{\text{bias}} > V_{\text{dep}}. \end{cases} \tag{4.6}$$

Therefore, plotting $\frac{1}{C^2}(V_{\text{bias}})$ ideally yields a linear behavior which kinks at the depletion voltage V_{dep} and assumes a constant value for voltages higher than V_{dep}.
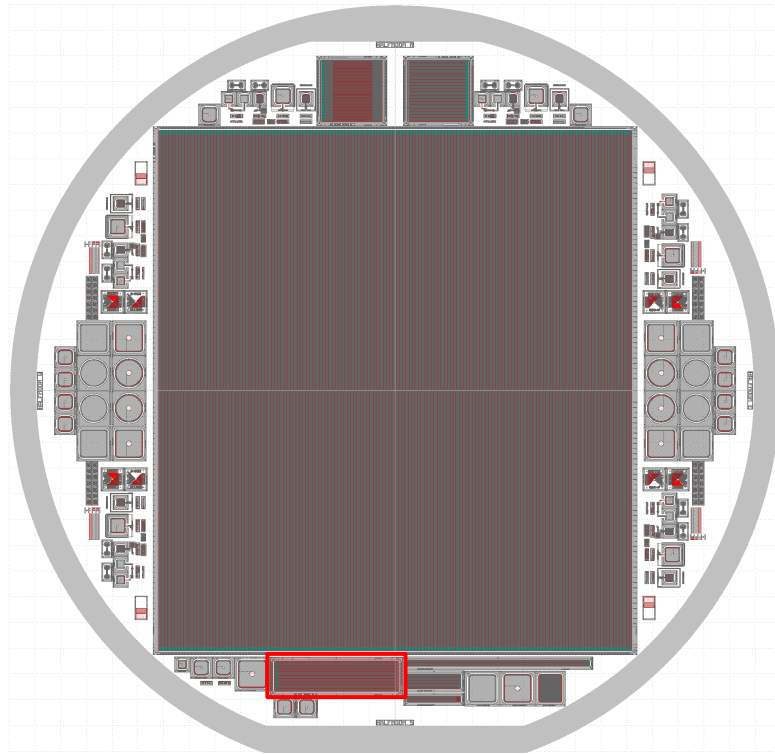
Figure 4.8.: The 2S wafer. The BABYSENSOR layout used in this thesis is marked in red.

4.5.3. Fabrication of Silicon Strip Sensors

Quartz is used as a starting material for silicon sensors. Since silicon can be extracted from natural resources in abundant quantities, it is highly suited for production of these sensors. Prices are therefore mostly defined by the number of processing steps and target qualities during fabrication.

Common processing steps are followed by all major manufacturers in the same manner, while details may vary and often are disclosed as part of company policy. Typical processing steps include

- processing of silicon dioxide to silicon,

- casting of silicon ingots,

- cutting the ingots into thin pieces called *wafers*,

- oxidation, doping, annealing and metallization,

- cutting the sensors out of the wafers.

To maximize cost efficiency, as many sensors and test structures as geometrically possible are fitted into one wafer.

4.5.4. The 2S Wafer

The sensors investigated in this thesis are cut out of a large silicon wafer, produced by Hamamatsu Photonics K.K. (HPK). For the present irradiation campaign, the HPK-2S wafer is used. An illustration of its design is shown in fig. 4.8. The large 2S sensor with 2032 strips is positioned in the mid part of the wafer. It is enclosed by numerous test structures including
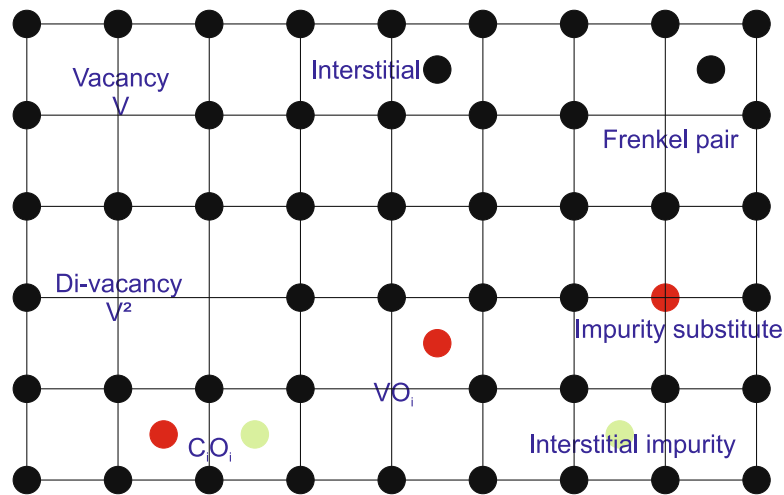
Figure 4.9.: Different kinds of bulk damage. transform the structure of the silicon lattice. All of these defects affect the material's electric properties. Vacancies (V), Di-vacancies (V^2), *Frenkel pairs*, substitutes and more complex defects are possible [Har17].

MOS structures, *mini sensors* and diodes. Strip pitches are fixed at 90 µm among all mini sensors.

Presented in this work are measurements that have been taken using sensors that are referred to as **Babysensors**. With a size of approximately $25\,800\,\text{µm} \times 7400\,\text{µm}$, they incorporate 60 strips.

Test structures such as Babysensors are cut out of the wafer individually. As a consequence of the amorphous structure at the cutting edges of the sensors, unwanted currents arise. To protect the sensitive area from high electric fields, the whole periphery is highly p-doped. The surface of a wafer is covered by an oxide layer which passivates areas that won't be contacted during readout or testing. A passivation increases the robustness of a sensor during the characterization process.

4.6. Radiation Damage

Particles traversing a crystal lattice cause damage to its structure. Radiation damage in silicon crystals can roughly be divided into two types of defects: surface and bulk damage [Mol99]. Most of what will be discussed in this thesis can be attributed to bulk defects. Therefore, this section will only discuss bulk damages.

4.6.1. Bulk Damage

Ionization is not the only process for particles to lose their energy. At sufficiently high energies, they may also interact with the atomic bodies themselves. Radiation damage in the silicon bulk is primarily caused by displacement of *primary knock-on atoms* (PKAs) out of their lattice site. As illustrated in fig. 4.9, PKAs represent interstitials and leave vacancies behind in the crystal structure. Pairs of interstitials and vacancies, called *Frenkel pairs*, may migrate and combine with impurity atoms to form more complex defects or even recombine to repair the damage. All of these defects change not only the form of the lattice but also its electric properties since they introduce different kinds of states within the band gap. Consequently, it is of utmost importance to select detector materials and structures that are sufficiently radiation hard. Radiation hard materials maintain high particle detection efficiency throughout their
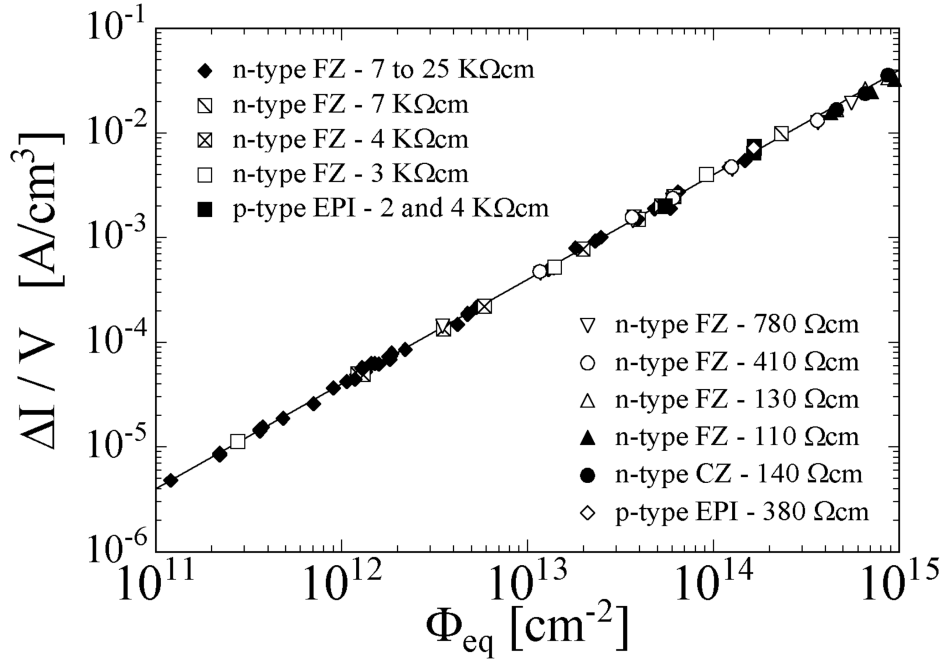
Figure 4.10.: Normalized increase in leakage current after irradiation over irradiation fluence. The linear behavior with the *current-related damage rate* α as its slope can be seen [Mol99].

projected lifetime inside a radiation environment. Since bulk defects make up most of the radiation damage inside a silicon detector, they represent a bottleneck for the operation of silicon detectors.

If the energy of a displaced atom is high enough, cascades of displacements may occur. While low recoil energies typically result in point defects, higher recoil energies may create clusters of displacements at the end of the PKA's track. Heavy, neutral particles interacting with the medium only by the strong force mainly produce long-range cluster defects [Har17].

4.6.2. Electrical Properties of Defects

Depending on their energy within the band gap, different types of bulk defects have different impacts on sensor properties. Since cluster defects cannot be described adequately by Shockley-Read-Hall statistics, following considerations will only cover certain defect levels and their effect on the sensor. For a more detailed explanation, consider [Mol99].

Leakage Current

Defects with energy levels close to the middle of the band gap favor generation of electron-hole pairs. Therefore, they are mainly responsible for the increase in leakage current I_{leak} of a sensor.

The increase in leakage current ΔI of a sensor after irradiation scales linearly with the irradiation fluence ϕ_{eq}

$$\frac{\Delta I}{V} = \alpha_{\mathrm{dmg}} \cdot \phi_{\mathrm{eq}}, \tag{4.7}$$

where $\Delta I = I_{\mathrm{irr}}(V) - I_0(V)$. Typically, the leakage current after irradiation is several magnitudes higher than before irradiation. Therefore it is justified to approximate $\Delta I \approx I_{\mathrm{irr}}$.

The propotionality factor α is called the *current-related damage rate*. To account for different sensor volumes V, the current has been normalized. The damage rate α_{dmg} can be used to monitor irradiation quality since the quantity is independent of particle types or sensor volumes used for irradiation. A depiction of this linear behavior can be seen in fig. 4.10.

Depletion Voltage

Some defect levels have a direct effect on the effective doping concentration N_{eff} and thus on the full depletion voltage V_{dep}. Ionized donors contribute positive space charge, while ionized acceptors contribute negative space charge. At room temperature, donors close to the conduction band and acceptors close to the valence band are ionized. Therefore, defects of this nature change N_{eff}.

Another mechanism of changing N_{eff} is called *acceptor/donor removal*. As already described in section 4.6.1, during irradiation mobile defects are created. These mobile defects may interact with dopant atoms forming complex defects. Since these complexes are usually not ionized, they do not contribute to space charge. Therefore, the effective doping concentration has been changed by effectively *removing* donors or acceptors.

Since the full depletion voltage V_{dep} scales with radiation induced damage, the detector's operation voltage has to be increased to reach full depletion for irradiated sensors. If the fluence is high enough, it may not even be possible to reach full depletion at all. As a consequence, the sensor's *signal to noise ratio* (SNR) is affected.

Charge Collection Deficiency

As explained in section 4.5, generated electrons drift towards the strips — following the applied field — to be read out by external electronics within a defined time frame. However, some of these electrons interact with deep defects and eventually are captured. If the time for reemission out of these defects takes longer than the shaping time of the readout amplifier, this part of the signal is essentially lost. This results in a charge collection deficiency.

4.6.3. The NIEL Scaling Hypothesis

As already established, charged particles like pions or electrons mainly interact with the detector material via the electromagnetic force while neutrons only interact with the atomic bodies by means of the strong force. To compare the radiation induced damage between different particle types with respect to their energy the so-called *Non-Ionizing Energy Loss* (NIEL) hypotheses are employed.

Under the basic assumption that "*any displacement-damage induced change in the material scales linearly with the amount of energy imparted in displacing collisions*" [Mol99], the damage imparted on the detector material may be scaled using a so-called *hardness factor*

$$\kappa := \frac{\int \mathrm{d}E \; D(E) \, \phi(E)}{D(n) \cdot \int \mathrm{d}E \; \phi(E)}, \tag{4.8}$$

where

$D(E)$ denotes the displacement damage cross section and

$\phi(E)$ are the energy spectra of particles used for irradiation of the material.

For the calculations in this thesis, a value of 2 is assumed for the hardness factor of protons with an energy of $23\,\mathrm{MeV}$ ($\kappa_{\mathrm{P}} = 2$).
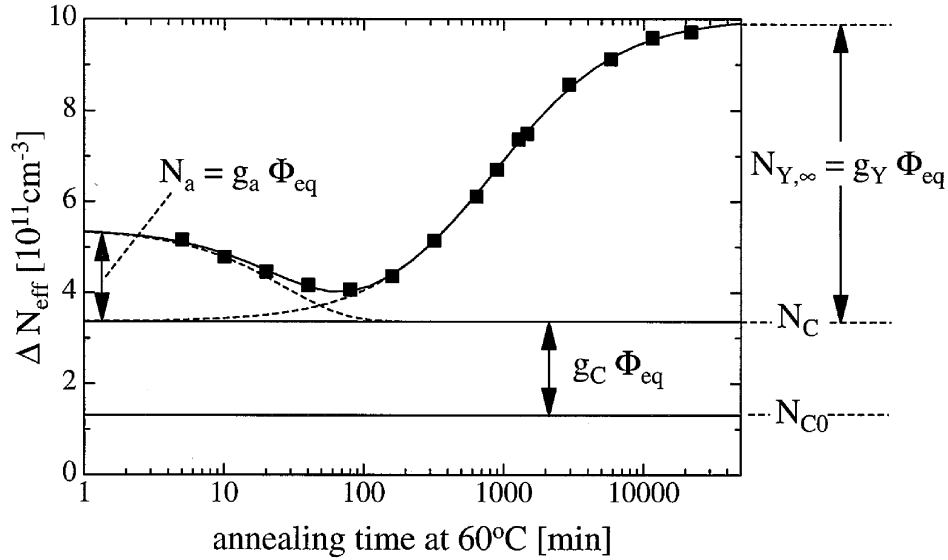
Figure 4.11.: ΔN_{eff} as a function of annealing time t for a temperature of $T = 60\,°\text{C}$. Mind the logarithmic scaling on the time axis. [MFL00]

With the definition in eq. (4.8), an *irradiation fluence* can be defined as

$$\phi_{\text{eq}} = \kappa \int \text{d}E \ \phi(E), \tag{4.9}$$

which is the particle flux for irradiation particles normalized to the displacement damage neutrons with an energy of $1\,\text{MeV}$ would cause. Equation (4.9) defines a useful unit for particle fluence: $[\phi_{\text{eq}}] = \frac{n_{\text{eq}}}{\text{cm}^2}$.

4.7. Annealing of Radiation Damage

All types of defects as they are discussed in section 4.6 show a temperature dependence in their concentration. Defects become mobile with increasing temperature and change the macroscopic properties of the silicon detector via different mechanisms. As a rule of thumb, the diffusion of defects is mostly frozen out below temperatures of $0\,°\text{C}$. Therefore, silicon sensors — as they are characterized in this thesis — should be kept at low temperatures ($-20\,°\text{C}$) during measurement pauses as not to skew the results of the study.

4.7.1. Annealing Mechanisms and the Role of N_{eff}

If the sensor is kept at temperatures above $0\,°\text{C}$, defects are able to diffuse and change the structure of the crystal lattice which is called *annealing*. Damages may be repaired (*beneficial annealing*) or even further amplified (*reverse annealing*) by annealing.

Migration of point defects may lead to recombination of counterparts with each other (Vacancy + Interstitial), repairing damages in the crystal lattice. However, point defects may also migrate to combine with other impurities or defects to form complex defects, as well, increasing damages in the crystal lattice.

If the activation energy becomes high enough by applying a sufficient annealing temperature, the lattice vibrational energy may be able to overcome the binding energy of complex clusters. This results in dissociation of clusters into the constituents, migration occurs.
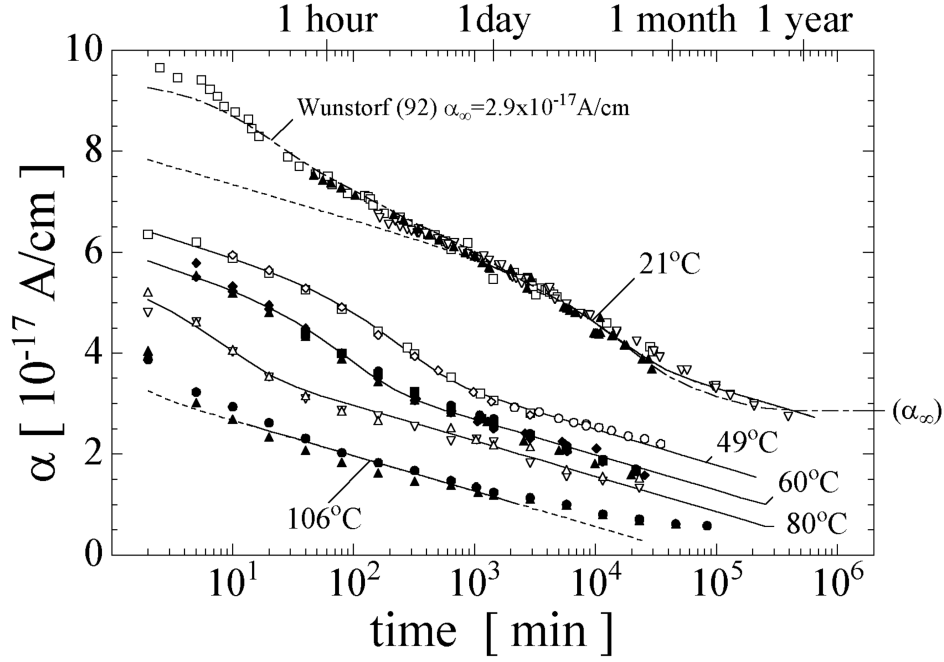
Figure 4.12.: α_{dmg} as a function of annealing time T_{ann}. The current-related damage rate decreases with growing annealing time [Mol99].

Since annealing changes the effective doping concentration N_{eff}, it is a suitable quantity to describe the effects of annealing. A common approach to parameterize annealing is with the ansatz [Mol99]

$$N_{\text{eff}}(t) = N_{\text{eff}}(\phi = 0) - \underbrace{\left(N_{\text{stab}}(\phi) + N_{\text{ben.ann.}}(t, T, \phi) + N_{\text{rev.ann.}}(t, T, \phi)\right)}_{\Delta N_{\text{eff}}}.$$

Decreasing ΔN_{eff} corresponds to beneficial annealing, while increasing ΔN_{eff} corresponds to reverse annealing. In practice this means that to repair radiation damage, one should aim for the minimum of the curve seen in fig. 4.11. The effect of defect annealing is drastic for small annealing times. Therefore, irradiated sensors should be kept at low temperatures as soon as the irradiation procedure has ended.

4.7.2. Parameterization of ΔI and α_{dmg}

Since annealing changes defect properties and how they are distributed throughout the detector material, naturally, the leakage current and current-related damage rate are affected by annealing as well. As depicted in fig. 4.12, the current-related damage rate α_{dmg} decreases with annealing time. An empirical approach to parameterize ΔI is by means of Fourier analysis

$$\Delta I(t) = \Delta I(t = 0) \cdot \sum_i b_i \exp\left(-\frac{t}{\tau_i}\right), \tag{4.10}$$

with $\sum_i b_i = 1$ [Wun92; Gil+92].

Following eq. (4.7) and eq. (4.10), the current-related damage rate may be parameterized like

$$\alpha_{\text{dmg}}(t, T_{\text{ann}}) = \frac{\Delta I(t)}{V \phi_{\text{eq}}} = \alpha_\infty \cdot \sum_i \frac{b_i}{b_\infty} \exp\left(-\frac{t}{\tau_i(T_{\text{ann}})}\right), \tag{4.11}$$

where T_{ann} specifies the time of annealing and ∞ denotes the highest index used for parameterization. However, this relation only holds for small annealing times [Mol99]. In his work, Moll proposes a more suitable parameterization for long-term annealing data by combining the Fourier ansatz with a logarithmic part

$$\alpha_{\mathrm{dmg}}(t) = \alpha_0 + \alpha_{\mathrm{I}} \cdot \exp\left(-\frac{t}{\tau_{\mathrm{I}}}\right) - \beta \cdot \log\left(\frac{t}{t_0}\right), \qquad (4.12)$$

with parameters $\alpha_0, \alpha_{\mathrm{I}}, \tau_{\mathrm{I}}, \beta$ found by best fit to the underlying data.

As can be seen in fig. 4.12, annealing always decreases the damage rate (and thus the leakage current) of a silicon detector. Higher annealing temperatures accelerate the annealing process. This is used in practice to study extended periods of annealing at room temperature in a short amount of time. The average value of the damage rate after $60\,\mathrm{min}$ of annealing at $80\,^\circ\mathrm{C}$ is approximately $4 \times 10^{-17}\,\mathrm{A/cm}$ [Har17].

Design and Concept Validation of the Iterative Irradiation Setup
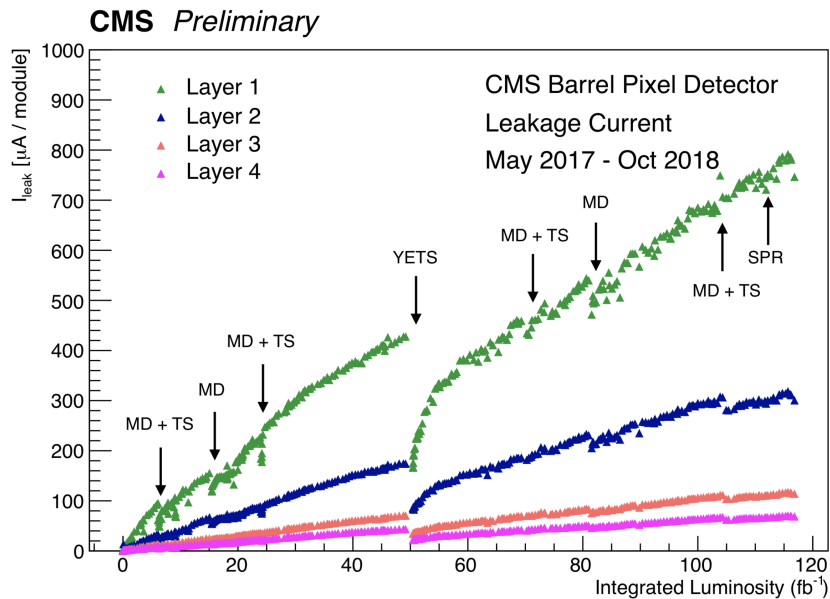

Figure 5.1.: The CMS Outer Tracker leakage current over time. Decreases in leakage current correspond to technical stops during which the silicon tracker has time to anneal damages [Zha19].

The following chapter will describe the conception, simulation and validation of an Iterative Irradiation Setup (IIS). Close attention will be paid to thermomechanical feasibility as well as mechanical design.

5.1. Irradiation Studies: Motivation For the Change of Concepts

The detector has to be sufficiently radiation hard in order to be operable up to a nominal integrated luminosity of $3000\,\mathrm{fb}^{-1}$. This corresponds to a nominal fluence of $1 \times 10^{15}\,n_{\mathrm{eq}}/\mathrm{cm}^2$ for PS modules in the Inner Tracker (see table 2.1). This value will be used as the target fluence in the following — despite the usage of 2S Babysensors for this study — in order to see a clear effect of radiation damage in the sensor. Irradiation and annealing studies are of utmost importance for characterization of the radiation hardness of (new) sensor materials and topologies.

Past irradiation studies pursued the concept of consecutive annealing scenarios: The sensor is irradiated to a nominal fluence at an irradiation facility and transported back to the characterization center for examination. To determine the effects of annealing, studies are conducted post-irradiation. Within the CMS Outer Tracker sensor group, a dedicated annealing
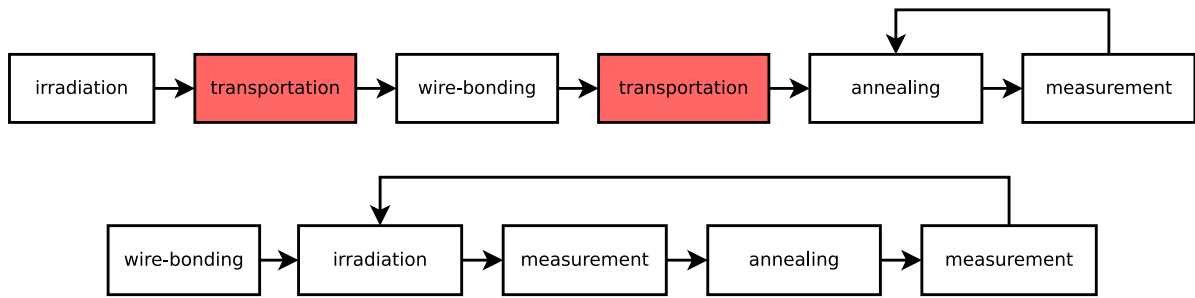
Figure 5.2.: Schematic diagram of different annealing procedures. Back-to-back annealing on the top versus iterative irradiation on the bottom. Sources of unwanted annealing are marked in red.

schedule is used to ensure a comparable and reproducable treatment of the irradiated structures. After each annealing step, a charge collection measurement as well as an IV characteristic curve is recorded.

This type of scenario, however, is not what happens in the real CMS tracker. Figure 5.1 shows the leakage current of the CMS Outer Tracker over time. During physics periods, the leakage current rises as a consequence of irradiation. During technical stops and long shutdowns, the detector must be kept at room temperature. Naturally, during these periods, radiation damages are annealed. Over the course of a year of physics, 2 weeks of annealing are accumulated. It is easy to see that annealing periods are not performed only after irradiation over the course of operation but appear in intermission. Therefore, the annealing study schedule described above is not suitable to reproduce the real-world operation of the detector.

A more suitable annealing scenario would be to reproduce the real-world application: Iterative irradation. In one measurement step, the sensor needs to be irradiated and annealed rather than just being annealed. After completing several measurement steps, the characterization would reproduce the iterative nature of irradiations encountered at the LHC. For better visualization, fig. 5.2 compares the presented measurement plans with each other.

Other than reproducing the real-world scenario, iterative irradiation provides additional benefits. With a consecutive annealing concept, sensors need to be transported back from the irradiation facility to the characterization center. Depending on the geographical distance between these places, logistical challenges emerge. To minimize the impact of unwanted irradiation during transportation and irradiation itself, sensors have to be cooled to temperatures of around $-20\,°C$. Ensuring a cool, safe and undisturbed environment during transportation is virtually impossible throughout the whole procedure. In [Eli19], the amount of unwanted annealing has been estimated to around 1 day of equivalent RT annealing.

With an iterative irradiation concept, sensors are irradiated and annealed *in situ* and, therefore, do not suffer from unwanted transportation annealing. However, iterative irradiation demands a fine control over the irradiated fluence in one step. Dividing the target fluence of $1 \times 10^{15}\,n_{\mathrm{eq}}/\mathrm{cm}^2$ into 10 steps (for 1 step per year of operation) would require irradiating the sensor with $1 \times 10^{14}\,n_{\mathrm{eq}}/\mathrm{cm}^2$ per step. The irradiation facility should be able to provide beam intensities low enough to irradiate the sensor to this fluence in an acceptable amount of time. For this thesis, CYRCé (see section 3.7) has been selected as the irradiation facility for iterative irradiation studies. A dedicated CMS beamline makes the beam time affordable. Furthermore, the machine provides fine enough control over the beam current.
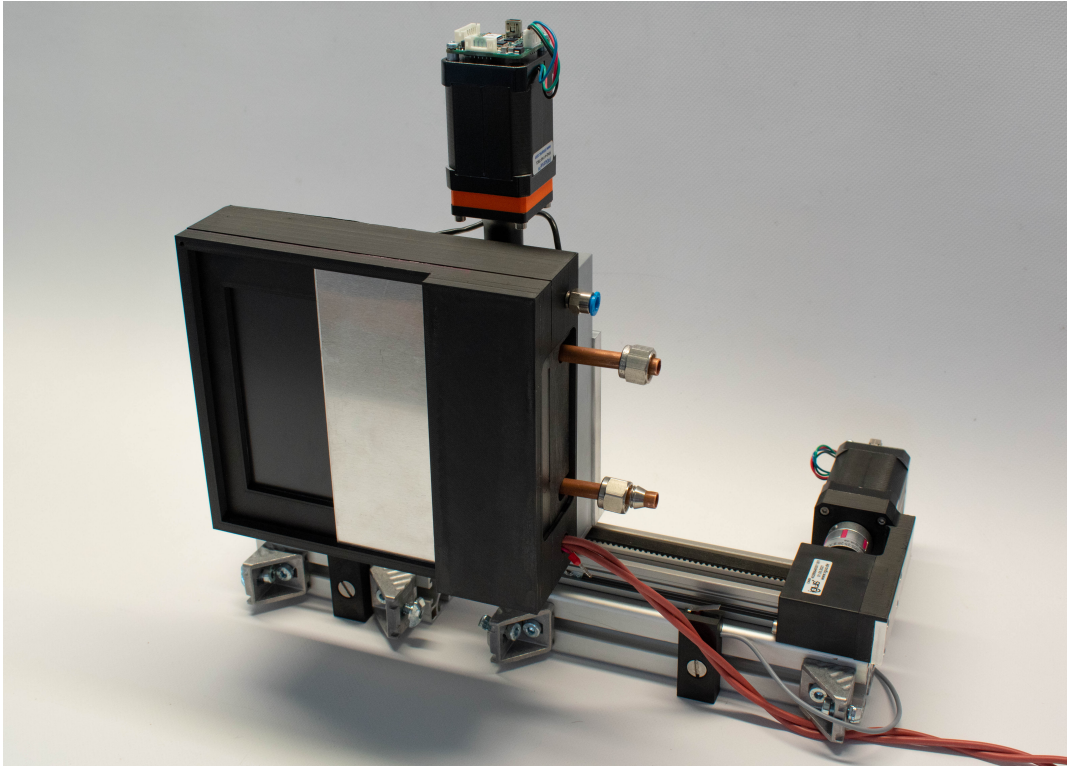
Figure 5.3.: The fully assembled Iterative Irradiation Setup (IIS). The measurement unit (MU) inside of the dry air box (DAB) is mounted onto the motor stage.

5.2. Mechanics

The IIS can roughly be divided into three different parts:

1. **The motor stage (MS)** is used for translation of the measurement unit inside of the dry air box.

2. **The dry air box (DAB)** is needed for environmental control around the sensor.

3. **The measurement unit (MU)** is mounted inside of the DAB and represents the heart of the IIS. It is used for cooling, sensor mounting and readout of data.

For better visualization, the fully assembled IIS is shown in fig. 5.3. More views of the IIS can be seen in appendix A.

5.2.1. Motor Stage

Two stepper motor drivers with hall sensor encoders and integrated step loss detection displace the measurement unit in x and z direction using NEMA-17 stepper motors [Tri21]. To ensure a sufficient scan speed and cost efficiency, translation in x direction is accomplished using a linear guide on a toothed belt. Translation in z direction is performed by usage of a spindle-driven z-table to limit the construction size. The measurement unit is screwed to the z-table by 3 screws and a strain relief, reducing stress on the measurement unit's pre-cooling pipes. Hardware controlled limit switches prevent collisions of the measurement unit with the surrounding aluminium scaffold and irradiation housing. A self-written software controller (see section 5.6) is responsible for coordinating the two axes in order to implement a scanning procedure during irradiation.
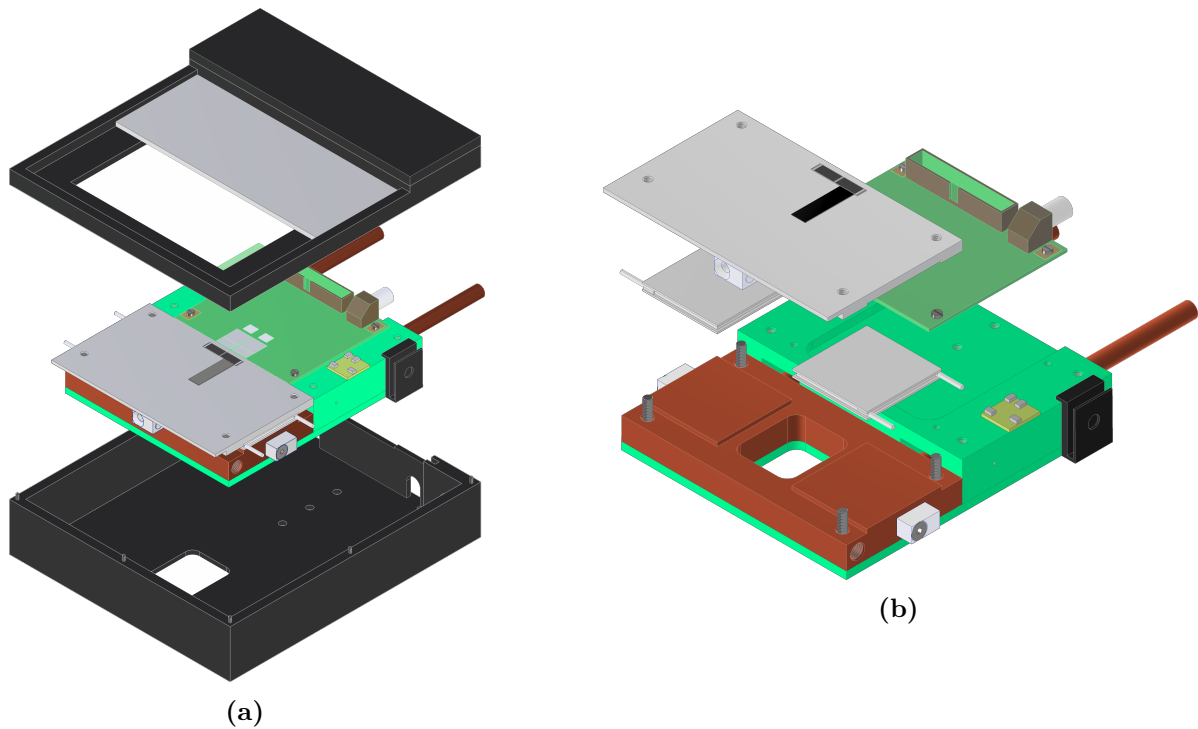
Figure 5.4.: Explosion diagrams of the IIS DAB and MU. a) The MU is screwed to the motor stage along with the DAB. b) The PPA and readout daughter board are mounted onto the GRP carrier.

5.2.2. Dry Air Box

An exploded view of the MU inside of the DAB is shown in fig. 5.4a. Made from ABS, the DAB provides openings for both the proton beam and a β-source. During charge collection and IV characteristic measurements as well as measurement intermissions the sensor on the measurement unit needs to be cooled down to $-20\,°C$. Naturally, the dew point around readout electronics as well as the sensor and its surroundings needs to be low enough to prevent dew from building up. Furthermore, the sensor needs to be kept in a sufficiently dark environment which is accomplished by blackened Kapton$^©$ foil across all openings. A roof made of purified aluminium protects readout electronics from radiation and SEL/SEU. A dry air inlet, cable outlets and openings for the pre-cooling copper pipes are located at the back side of the DAB.

5.2.3. Measurement Unit

An exploded view of the MU is shown in fig. 5.4b. A glass reinforced plastic (GRP) carrier represents the base of the measurement unit. It is used for mounting the ALiBaVa readout daughter board. It also carries a composite consisting of the pre-cooling stage, the Peltier elements and the aluminium chuck. In the following, this composite will be referred to as the PPA. The PPA is fixated onto the GRP carrier using 4 plastic screws to limit heat transfer from the pre-cooling stage to the aluminium chuck.

The sensor chuck is made of purified aluminium to reduce activation of all components of the MU. Two temperature sensors are screwed to the copper bridge to monitor the temperature while one sensor is glued to the aluminium chuck. Insulation material is placed between the aluminium chuck temperature sensor and the pre-cooling copper bridge to limit the effects of
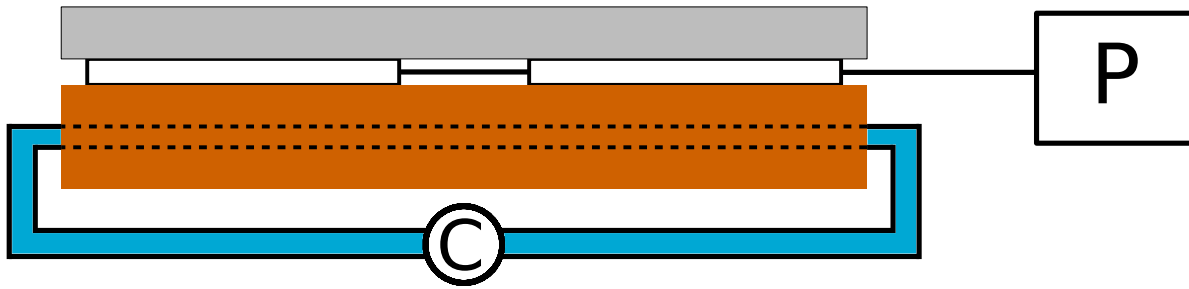
Figure 5.5.: Schematic diagram of the IIS cooling concept. A liquid pre-cooling copper stage removes heat generated by the hot side of two Peltier elements.

convection and radiation to the sensor that could falsify its readings. A dew point sensor is placed next to the measurement unit to monitor the status of the dew point inside of the DAB.

An HV filter located on the near side of the sensor is used for ripple filtering of the biasing rail. The sensor is fixated onto the aluminium chuck using Kapton© tape. A pocket only leaving $300\,\mu m$ of aluminium below the sensor is milled into the sensor chuck to mount the sensor and make it possible for beta rays to penetrate the sensor and chuck. Also for this purpose, beneath the pocket, a window is carved out of the total PPA.

At the side of the measurement unit, cable clips manage cable routing of several components. The motor stage and DAB with the MU inside are transported and integrated into the irradiation box at the CYRCé beamline separately.

5.3. Thermomechanical Requirements

The following section will introduce the thermal concept of the IIS and explain important aspects and challenges that emerged during conception of its design. Results of thermal simulations and a real-world emulation with comparable components will be presented.

The measurement program for iterative irradiation and annealing studies requires

- **cooling to −20 °C** during measurement intermissions, charge collection and IV characteristic measurements as well as

- **heating to 60 °C** during annealing periods.

The cooling concept has to ensure that these temperatures can be reached and stabilized for extended time periods. Mechanical components should be reusable for many iterations to come and long-time performance is of high importance in order to carry out the study with comparable prerequisites for different sensors.

5.3.1. Concept

A feasible thermal concept is paramount to reproducible and stable performance of iterative irradiation tests. Required temperatures need to be reached quickly and be kept reproducibly stable in order to reduce the effects of unwanted annealing. For this purpose, a two staged cooling concept is employed. It consists of a liquid pre-cooling copper bridge and two Peltier elements as primary thermal agents. A schematic diagram of this cooling arrangement is shown in fig. 5.5.

The pre-cooling stage is driven by a chiller providing a coolant circuit. A constant set temperature can be adjusted to stabilize the temperature of the copper bridge. It acts as a heat bath for the primary cooling stage which consists of two Peltier devices and a cooling
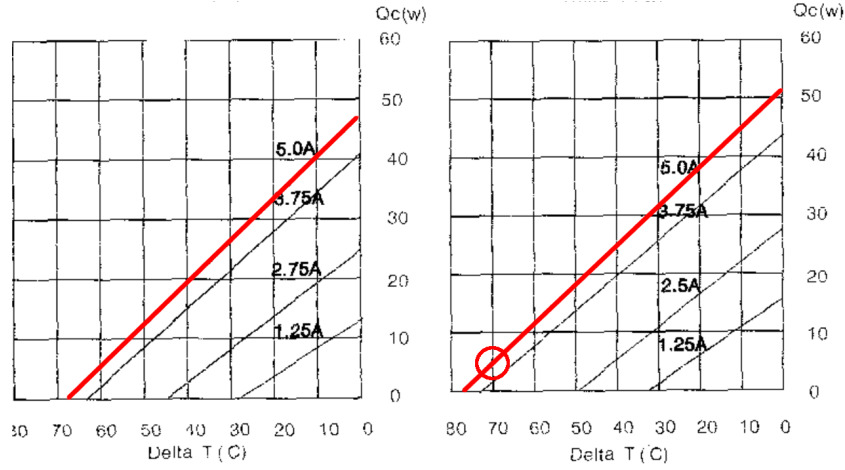
Figure 5.6.: Estimation of the maximum heating power P_{max} of TEC1-12705 thermoelectric devices as a function of the hot side temperature T_h [Eve20].

chuck made of purified aluminium. Cooling/Heating power can be adjusted by controlling the electric power supplied to the thermoelectric cooling agents.

To test the performance of this thermal concept, steady state finite-element simulations as well as a real-world emulation with comparable components are employed.

5.4. Steady State Thermal Simulation

The main thermal agents are TEC1-12705 thermoelectric devices. They operate by the Peltier-Seebeck effect which means that by applying an electric current, the temperature difference $\Delta T = T_h - T_c$ between two sides of a thermocouple is increased. The temperature of the hot side of the Peltier element is denoted as T_h, whereas the temperature of the cold side is T_c. By forcing one side of the thermoelectric device to be at a constant pre-cooling temperature T_{pre}, the temperature of the other side — which is connected to the aluminium chuck in the PPA composite — can be varied.

Past experiences have shown that the critical point of this thermal concept lies in heating up the aluminium chuck to a desired temperature and keeping it stable. In order to evaluate the thermal performance beforehand, steady state thermal simulations are performed for the heating process. Worst case scenarios are assumed which means that all parameters are chosen so that reaching the annealing temperature is as difficult as realistically possible. An annealing temperature of 60 °C is desired.

For symmetry and space constraints, a number of two Peltier elements is chosen. The maximum T_{pre} the chiller at the CYRCé beamline can provide is limited to values below 0 °C. As a worst case assumption (WCA), $T_{pre} = -10$ °C is assumed.

As a point of reference for the thermal power of one thermal agent, its datasheet is consulted. It is shown in fig. 5.6. To estimate the maximum cooling power P_{max}, plots of the cooling power as a function of T_h for $T_h = 25$ °C and 50 °C are used as means of extrapolation since a plot for $T_h = 60$ °C was not available. It is easy to see that plots for higher values of T_h can be obtained by shifting the characteristic curves towards higher ΔT values. For a supplied electric current of 5 A at a voltage of 12 V (= 60 W), an estimation of $P_{max} \approx 7$ W can be made. Therefore, a value of $P_{peltier} = 7$ W will be used for thermal simulations.

Boundary conditions need to be specified in order for the FEA to converge. As covered in section 3.8, parameters for convection, radiation and pre-cooling temperature need to be set.
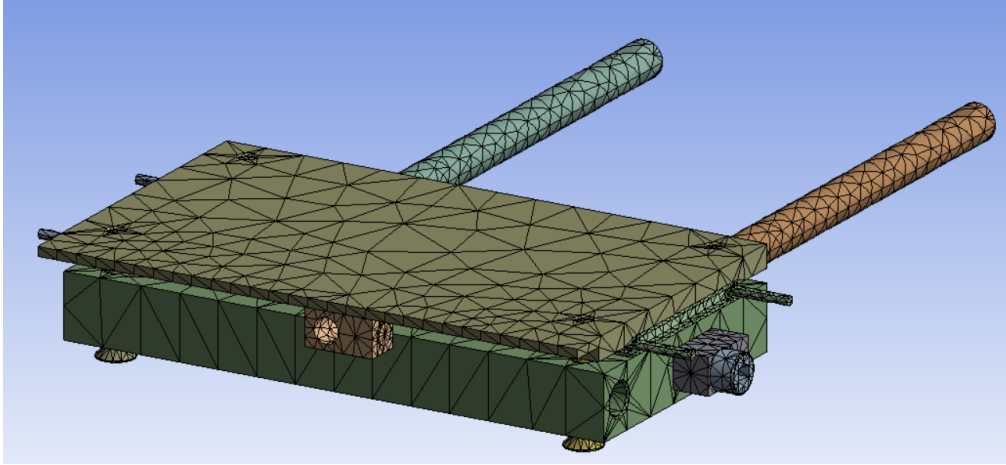
Figure 5.7.: FE model used for thermal analysis of the heating process. The FE representation of the MU has been limited to parts that are relevant to thermal analysis for computation time efficiency.

Table 5.1.: Input material properties used in the FEA

Material	Thermal Conductivity (Isotropic) $\lambda \left(\frac{W}{m\,K}\right)$	Emissivity ϵ
Purif. Al	236	0.2
Cu	300	0.8

The investigated FE model is shown in fig. 5.7. The FE representation of the MU has been limited to parts that are relevant to thermal analysis. The GRP carrier as well as the daughter board have been omitted from the FE model. It represents a good approximation of the whole measurement unit since GRP is a good thermal insulator and thus, heat transfer to the carrier and DB can be neglected.

For heat transfer by thermal radiation, all non-covered surfaces are assigned an emissivity. To model convection, all non-covered surfaces are assigned a heat transmission coefficient λ and an ambient temperature of 8 °C. All input material properties used in the model are listed in table 5.1.

To model the thermal effect of the thermoelectric devices in the simulation, thermal power flows are assigned to flow from the Peltier elements to the aluminium chuck and from the pre-cooling bridge to the Peltier elements. The maximal total thermal power delivered to the aluminium chuck P_{tot} is the sum of Joule heating P_J caused by the flow of electric current in the Peltier element and the thermal power introduced by the Peltier-Seebeck effect P_{th}

$$P_{tot} = n_{Peltier} \cdot (P_J + P_{th}) = 2 \cdot (60\,W + 7\,W).$$

The maximal total thermal power drawn from the pre-cooling bridge is the thermal power introduced by the Peltier-Seebeck effect $P_{th} = 2 \cdot -7\,W = -14\,W$.

To estimate the impact of the heat transmission coefficient α, the aluminium chuck temperature at the location of the silicon strip sensor is simulated as a function of the pre-cooling temperature T_{pre}. Three different values for α are examined. The ambient temperature has been estimated by beamline personnel to be at roughly 8 °C. This value is assumed for the simulation. Depicted in fig. 5.8, as expected the aluminium chuck temperature scales with decreasing convection since stronger convection causes the aluminium chuck to assimilate its
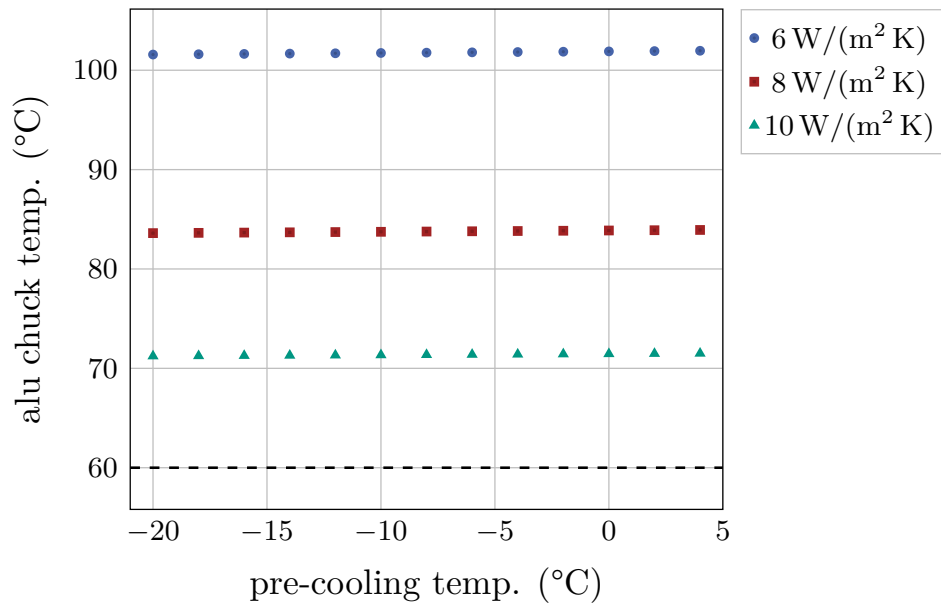
Figure 5.8.: Impact of the heat transmission coefficient α. Three different values of $\alpha = 6,\ 8,\ 10\,\mathrm{W/(m^2\,K)}$ are examined. The desired annealing temperature is indicated by a dashed line.

temperature to the environment quicker. Limitations of the simulation are, however, evident by the constant behavior of the curves with respect to the pre-cooling temperature T_{pre}. A lower pre-cooling temperature should be causing the air around the aluminium chuck to cool down. The cooler air around the chuck should therefore cool it down, which means that the aluminium chuck temperature should scale with the pre-cooling temperature. This second-order effect should be negligibly small since the pre-cooling temperature itself is varied in a range one order of magnitude lower than the temperature increase in the heating process.

A heat transmission coefficient of $10\,\mathrm{W/(m^2\,K)}$ corresponds to a rather strong breeze of dry air and (under normal circumstances) will never be encountered for the real setup. However, it is used as a WCA to estimate the impact of other parameters in the simulation.

In the following, the impact of the pre-cooling temperature T_{pre} and the ambient temperature T_{amb} on the aluminium chuck temperature is investigated. T_{amb} is set equal to T_{pre}. Like this, the WCA of the pre-cooling bridge cooling down all of the air around the setup to its temperature is simulated. A plot of the aluminium chuck temperature as a function of $T_{\mathrm{amb}} = T_{\mathrm{pre}}$ is shown in fig. 5.9. As expected, the aluminium chuck temperature scales with T_{amb}. In the simulation, a temperature of $T_{\mathrm{amb}} = T_{\mathrm{pre}} \approx -5\,°\mathrm{C}$ is needed in order to reach the desired annealing temperature. Therefore, it is advisable to set the pre-cooling temperature to values above $-5\,°\mathrm{C}$ to ensure that the annealing temperature can be reached and kept stable in the real world application.

Considering the steady-state thermal simulations it can be summarized that the desired annealing temperature can be reached with a pre-cooling temperature $T_{\mathrm{pre}} > -5\,°\mathrm{C}$ under all WCAs.

5.5. Real-World Thermal Emulation

To verify the integrity of the presented thermal concept, a mockup PPA has been built. It is built up of materials with comparably large components to model the real PPA as closely
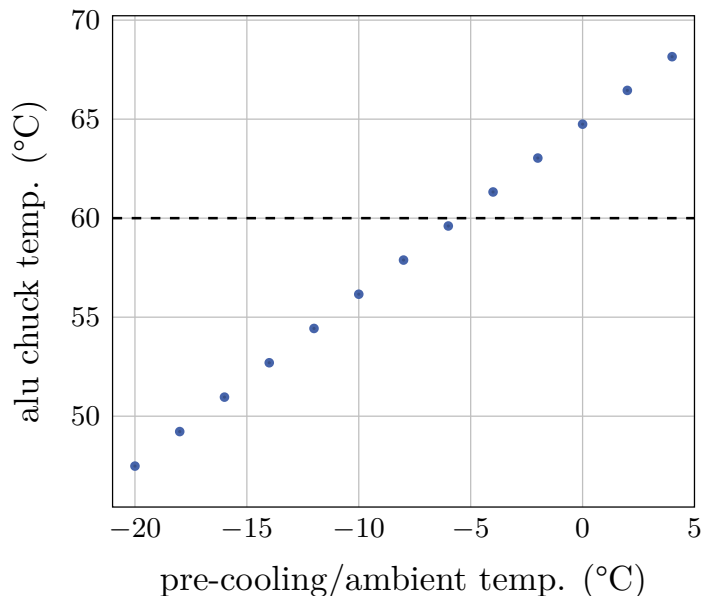
Figure 5.9.: Impact of the ambient temperature T_{amb} and pre-cooling temperature T_{pre} **for** $T_{amb} = T_{pre}$**. The desired annealing temperature is indicated by a dashed line.**

as possible. Using a mockup system to test the thermal concept beforehand saves time and production costs in case of failure.

A picture of the experimental setup can be seen in fig. A.2. The mockup PPA is connected to a chiller, providing a coolant circuit as it will be encountered in the application at the CYRCé cyclotron beamline. It is placed inside of an insulated box with insulator material used to fill empty space around it. A dry air inlet is placed next to the mockup to emulate convection and lower the dew point as in the real application. Apart from being marginally larger than the real PPA, the aluminium chuck is built of AlMg$_3$ rather than purified aluminium. AlMg$_3$ exhibits an isotropic thermal conductivity of around $120 \, W/(m \, K)$ which is 50% smaller than that of purified aluminium. This discrepancy should not be relevant in thermal equilibrium, however, one can expect the real setup to reach equilibrium faster than the mockup PPA.

For evaluation of the mockup, the maximum heating power is adjusted for the Peltier elements. This is accomplished by biasing the Petlier elements at their maximum rated voltage. The aluminium chuck temperature is recorded as a function of time. This is shown in fig. 5.10. Temperature ramps are recorded for both maximal dry air inflow and no dry air inflow. In both cases a plateau temperature of around $84 \, °C$ stabilizes in the recorded time range. As expected, convection does not play a vital role in the final chuck temperature.

Taking the thermal simulations as well as the real-world emulation into account, it can be concluded that the desired annealing temperature can be reached and stabilized with the thermal concept presented in this section.

5.6. Interfacing the Setup

The following subsection will describe key aspects of software used for interfacing the mechanical parts of the IIS.
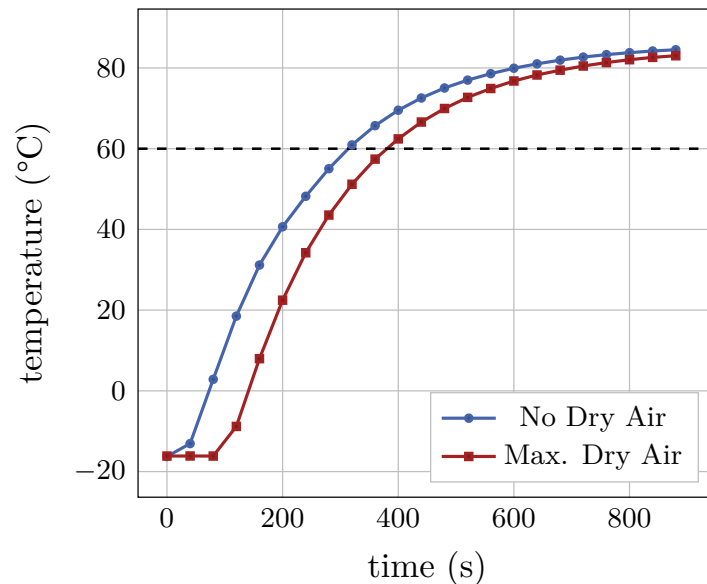
Figure 5.10.: Mockup aluminium chuck temperature as a function of time. A plateau temperature of around 84 °C is reached for the recorded time range.

5.6.1. Back End: MC Devices and the Motor Controller

The MeasurementControl (MC) back end is used to interface the hardware layer of this application.

A new MC device is written (`trinamic.py`) to represent one Trinamic stepper motor driver (as it is described in section 5.6). It implements basic features that allow the safe movement of the stepper motors as well as adjustment of hardware specific parameters. Two `trinamic` MC devices are necessary to drive the stage in the x- and y-direction.

Coordination of these two devices is accomplished by a controller class (`motor_controller.py`). It implements a finite state machine that manages the current path for the scanning procedure of an irradiation as well as the movement of both stages in a specific order to ensure safe movement paths. Microstep-distance translation is done with a dedicated calibration procedure and results are stored in a configuration file. One (adjustable) limit switch per axis provides a stop point for reference drives. The motor controller can be accessed by exposure of Flask endpoints. HTTP requests are sent to the controller and return the internal state of the state machine along with data such as the current irradiation path.

5.6.2. Front End: The Irradiation Interface

The front end application used for monitoring iterative irradiation procedures is the *Irradiation Interface*. It is based on the Javascript framework Vue and is built with scalability in mind. Commands are sent to the back end via HTTP requests as described earlier. The interface consists of 4 tabs, each serving a different purpose.

The first tab is shown in fig. A.3 and is used to provide the IP adresses that will be used to contact the back end and an InfluxDB storing and serving thermal data via a Grafana interface. To reduce the footprint of locally saved session data, IPs are stored as cookies within the session and need to be reentered upon refreshing the site.

The second tab provides thermal control and monitoring. Controls are provided to set the operation temperature of the PID controller that is used to stabilize the aluminium chuck
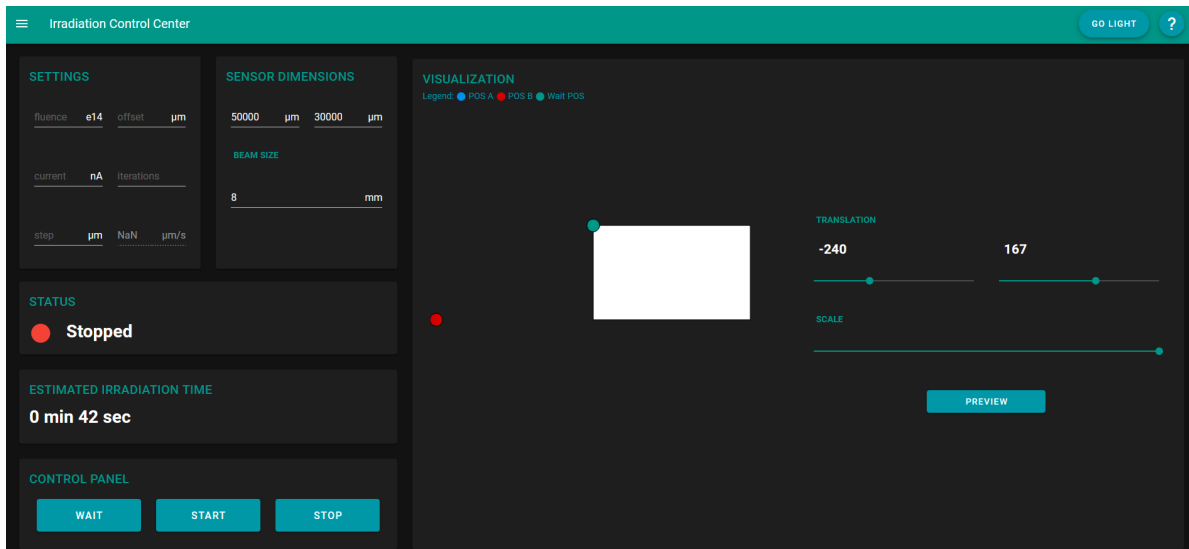
Figure 5.11.: Irradiation tab of the Irradiation Interface. A scalable, visual representation of the irradiation path is shown on the right. Alignment positions are shown as colored marks. Irradiation parameters are adjustable by the user on the left. An estimated irradiation time is shown after entering the irradiation parameters.

temperature. A grafana panel is embedded into an `iframe` to monitor thermal data provided by the InfluxDB.

The third tab is shown in fig. A.4 and is used for alignment and controlling the motor. After a reference drive, the display indicates the physical position of the stage with respect to the origin. Two positions (`A`/`B`) corresponding to the top left and bottom right corner of the irradiation area need to be set in order to calculate the irradiation path using user-defined path parameters in the irradiation tab. The waiting position (`WAIT`) serves as a safe point to turn on the proton beam as well as a return point in case of failure. The `ALiBaVa` position is the position at which the radioactive β-source is located.

The fourth tab, the irradiation tab, is shown in fig. 5.11. It features an input form in which parameters of the irradiation can be entered by the user. After calulation of the irradiation path, it is visualized along with the set alignment position as well as the current position of the proton beam during irradiation. The optical representation of the current beam position is obtained by polling of the motor stage position. Therefore, the displayed position is in agreement with the real position in hardware. An estimation of the irradiation time based on the current irradiation path is displayed once it has been calculated.

With the presented graphical user interface, iterative irradiations implementing a scanning procedure is possible while monitoring all relevant information such as temperatures and the dew point.

5.7. The Charge Collection Mockup

To test the charge collection measurement prior to production of the designed setup, a mockup has been built using readily available materials. The pre-cooling copper bridge as well as the Peltier elements have been omitted since they are not relevant for charge collection measurements of an unirradiated sensor. $AlMg_3$ has been used instead of purified aluminium, since the CCM has no need of being radiation hard as it will not be used with a proton source. Since the β-source cannot penetrate $3\,mm$ of purified aluminium to trigger the scintillator beneath the
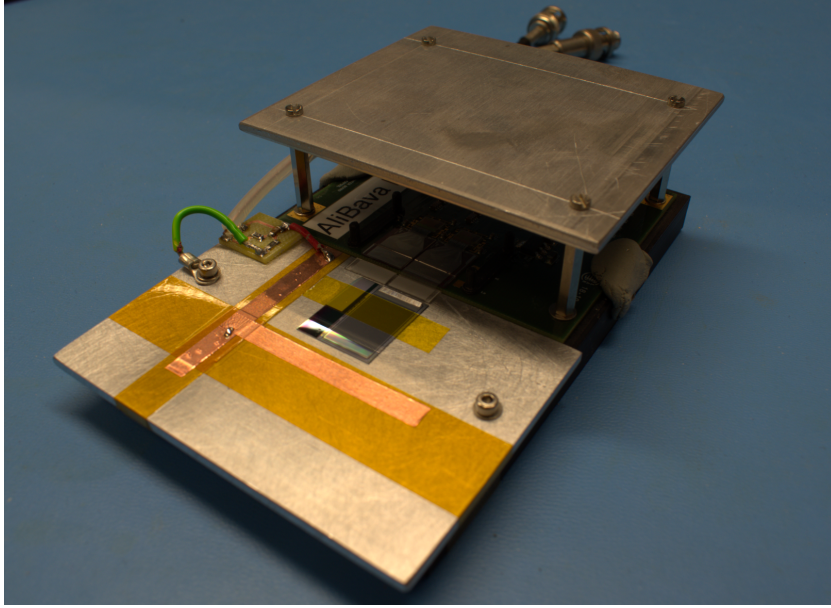
Figure 5.12.: The Charge Collection Mockup (CCM). A hole has been drilled into the aluminium chuck underneath the sensor to make charge collection measurements with a β-source possible.

Table 5.2.: Comparison of parameters obtained with the CCM and ALiBaVa station. Sensor FZ290_27_KIT_Test was used. Measurements were carried out at $T = 20\,°C$ with $n_\text{trig} = 500\,000$.

System	bias voltage (V)	σ_sig (ADC)	CM (ADC)	cluster signal (e⁻)
CCM	−300	3.45	99	25 153
GRP board	−300	3.27	104	25 780
CCM	−600	3.35	92	26 099
GRP board	−600	3.31	113	25 845

aluminium chuck, a hole is drilled into the chuck. The silicon strip sensor is placed above the hole. For the real setup, such a solution is not suitable. Instead, a thinned out portion of aluminium will be carved out of the block material, which will be thin enough for beta rays to penetrate.

The mockup is placed inside of the ALiBaVa station at ETP. A Sr-90 β-source is placed above the sensor. The readout is triggered by usage of a PMT placed beneath the mockup, providing a NIM signal that can be connected to the ALiBaVa mother board without discrimination.

Figure 5.13 shows the Landau-Gauss distributed signal that has been obtained with the CCM. For reference, all parameters that have been obtained by the measurement using the CCM have to be compared to parameters obtained by the already established ALiBaVa readout station. The usage of the same sensor with both systems increases the significance of the comparison. Parameters obtained for both systems are compared in table 5.2. As expected, the acquired cluster signals are consistent among both systems within the declared measurement uncertainty. The RMS common mode subtracted noise value σ_sig is marginally lower for the GRP board. However, the effect is negligibly small and could be originating from different bonding lengths, varying the input capacitance to the Beetle channels. The common mode noise is systematically lower for the CCM. Factors that could lead to this effect are the larger
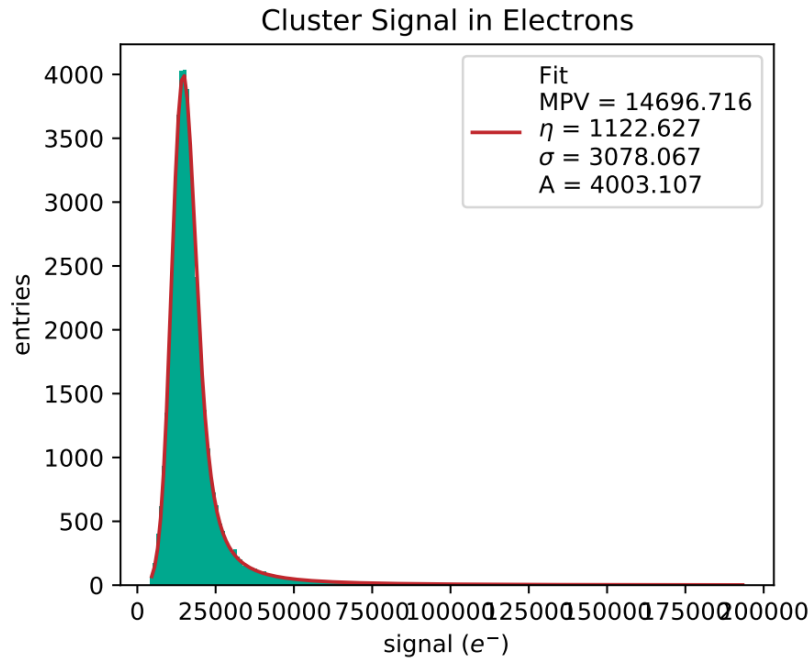
Figure 5.13.: Landau-Gauss distributed signal obtained with the CCM. A KIT_Test sensor has been biased to 100 V for the measurement.

HV chuck and ungrounded aluminium roof that is placed on top of the daughter board to emulate a radiation protection. Since the effect could also vary with external electromagnetic disturbances that would not remain the same for both measurement series (CCM $\leftrightarrow$ GRP board), an explanation remains unconclusive.

All in all, the CCM confirms the conceptual design of a measurement unit to be used in an iterative irradiation scenario. Charge collection remains unchanged with respect to the stationary ALiBaVa setup used at ETP.

5.8. Testing the IIS

In this section, the fully assembled IIS is tested with regard to its mechanical and thermal properties.

Table 5.3.: Verification of the motor speed. A good agreement of the measured and theoretical speed is necessary in order to ensure that the desired irradiation fluence is reached. For all measurements $d = 48\,650\,\mathrm{\mu m/s}$.

$v_{x,\mathrm{des}}\left(\frac{\mathrm{\mu m}}{\mathrm{s}}\right)$	t (s)	$v_{x,\mathrm{meas}}\left(\frac{\mathrm{\mu m}}{\mathrm{s}}\right)$
1872	25.86	1881.28 ± 0.35
	25.42	1913.85 ± 0.36
	25.61	1899.65 ± 0.36
3744	12.89	3774.24 ± 1.41
	12.92	3765.48 ± 1.40
	12.88	3777.17 ± 1.41

(a)   (b)
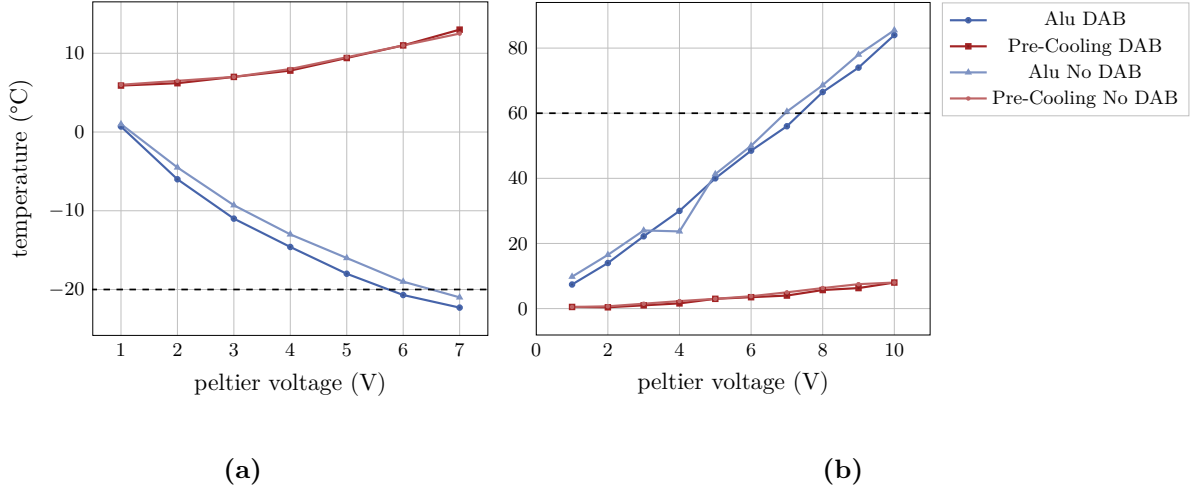
Figure 5.14.: Comparison of alu chuck and pre-cooling plateau temperatures as a function of the applied peltier voltage. a) shows the cooling test at a pre-cooling temperature of $5\,°C$. b) shows the heating test at a pre-cooling temperature of $0\,°C$.

Mechanical Testing

As established in [Die03], the irradiated fluence ϕ_{eq} using a scanning procedure is given by

$$\phi_{\text{eq}} \approx \frac{n \cdot I \cdot \kappa}{v_x \cdot q_{\text{el}} \cdot \Delta z}.$$

So in order to irradiate a sensor to a desired fluence ϕ_{eq}, the scanning speed in x-direction v_x has to be known as precisely as possible. After calibration of the microstep-distance translation of the motor stage, v_x is verified by taping a piece of paper to the z-table and shining a laser with a beam width of $20\,\mu m$ onto it. Two points on the sheet of paper are marked beforehand and their distance from each other d is measured using a vernier caliper. d is chosen to be as large as possible to reduce systematic uncertainties. The laser is moved from one point to the other by driving the stepper motor with a desired speed $v_{x,\text{des}}$. To measure the time it takes for traversing d, video analysis of this procedure is performed at a rate of $60\,\frac{\text{frames}}{\text{s}}$. Assuming that the probability to pinpoint the location of the laser above the marked point within one frame is uniformly distributed, this yields an uncertainty of $\sigma_t = \frac{1}{2\sqrt{3}} \cdot \frac{1}{60}$ second $= 4.81\,\text{ms}$. Propagating this error into v_x gives $\sigma_{v_x} = v_x \frac{\sigma_t}{t}$. The uncertainty on d is negligibly small. Recorded data for two values of $v_{x,\text{des}}$ is listed in table 5.3. For a desired speed of $1872\,\frac{\mu m}{s}$, a speed of

$$v_{x,\text{meas}} = (1898.26 \ \pm 0.36 \ (\text{sys.}) \ 13.33 \ (\text{stat.})) \ \mu m/s$$

and for a desired speed of $3744\,\frac{\mu m}{s}$, a speed of

$$v_{x,\text{meas}} = (3772.30 \ \pm 1.41 \ (\text{sys.}) \ 4.97 \ (\text{stat.})) \ \mu m/s$$

is determined. Judging by the data obtained by this method, the error on the irradiation fluence should be on the sub-percent level.

Thermal Testing

The thermal performance of the IIS needs to be ensured. For this purpose, a constant voltage is applied to the Peltier elements. Pre-cooling and aluminium chuck temperatures are recorded after a plateau temperature has been reached. For the cooling process, a range of $V_{\text{peltier}} = 0\,\text{V}$

to 7 V is examined, since higher values for V_{peltier} would cause the impact of Joule heating on the aluminium chuck temperature to be greater than the Peltier-Seebeck effect. For the heating process, this is not a problem and a range of $V_{\text{peltier}} = 0\,\text{V}$ to $10\,\text{V}$ is examined. This measurement program is performed for both the MU **without DAB** as well as **with the DAB**. For the cooling test, the pre-cooling temperature was set to $5\,°\text{C}$, while for heating tests, a temperature of $0\,°\text{C}$ was selected.

The acquired data is shown in fig. 5.14a and fig. 5.14b. It is easy to see that the DAB has little impact on the plateau temperatures reached. Furthermore, both desired temperatures are reached within the recorded ranges and can be kept stable. As expected, higher plateau temperatures can be reached for the heating process than simulated, since the WCAs lead to a lower estimate on the possible operation temperature. The maximum recorded heating temperature is in accordance with the thermal emulation presented in section 5.5. To preserve the IIS for as long as possible, it is not advisable to operate the Peltier elements at temperatures higher than the annealing temperature for extended time periods.

All in all, the thermal performance of the IIS is sufficient for this application.

6

Experimental Results

This section describes the measurement plan for the iterative irradiation program as well as experimental results obtained during the course of a beam test at the CYRCé cyclotron. The outlined measurement program represents one examplary irradiation procedure with practical orientation out of many procedures that could be performed.

6.1. Measurement Program

The expected fluence for PS modules in the Outer Tracker of CMS at an integrated luminosity of $3000\,\mathrm{fb}^{-1}$ lies at $1 \times 10^{15}\,n_{\mathrm{eq}}/\mathrm{cm}^2$. This integrated luminosity will be reached over the course of (nominally) 10 years of runtime. Per year, it is planned to anneal for 2 weeks during technical stops, totalling 20 weeks over the total runtime.

To model this scenario during iterative irradiation, one iteration consists of one irradiation to a fluence of $1 \times 10^{14}\,n_{\mathrm{eq}}/\mathrm{cm}^2$. With 10 iterations, this sums up to the expected fluence for PS modules in the OT. After each irradiation, the sensor will be annealed at $60\,°\mathrm{C}$ for $85\,\mathrm{min}$ which translates to roughly 2 weeks of annealing at RT. Between all steps, the leakage current and charge collection are measured.

Technical difficulties that emerged during beam testing the IIS have caused a deviation from this measurement plan. Instead of $1 \times 10^{14}\,n_{\mathrm{eq}}/\mathrm{cm}^2$ of fluence per step, $2 \times 10^{14}\,n_{\mathrm{eq}}/\mathrm{cm}^2$ needed to be used. Furthermore, charge collection measurements could not be recorded because of a technical fault in the readout electronics.

The iterative irradiation procedure as well as leakage current measurements have been performed. Results of charge collection measurements in an unirradiated state as well as leakage current measurements for iterative irradiations will be presented.

6.2. Validation of the Irradiation Quality of the CYRCé Cyclotron

Since CYRCé is a recently established cyclotron and no prior work with ETP has been done at the CMS beamline, the irradiation quality has to be verified. Two Babysensors have been sent to the IPHC and irradiated using an xy-stage already present at the facility. The nominal irradiation fluence for both CYRCé samples is $5 \times 10^{14}\,n_{\mathrm{eq}}/\mathrm{cm}^2$.

For comparison, three samples have been irradiated at the already known KAZ cyclotron. The nominal irradiation fluence for all KAZ samples is $4.7 \times 10^{14}\,n_{\mathrm{eq}}/\mathrm{cm}^2$ since no data was available for a fluence of $5 \times 10^{14}\,n_{\mathrm{eq}}/\mathrm{cm}^2$.

During the irradiation process, a scanning procedure is performed at both beamlines. Technical difficulties regarding the xy-stage present at the CYRCé beamline emerged. Only half of the area of Babysensor 34359_029 has been irradiated. The irradiation for the remaining sample (34353_033) was successful.

In order to compare the irradiated samples with data already present in the ETP database, the ALiBaVa setup has been employed to measure the charge collection of all irradiated samples.
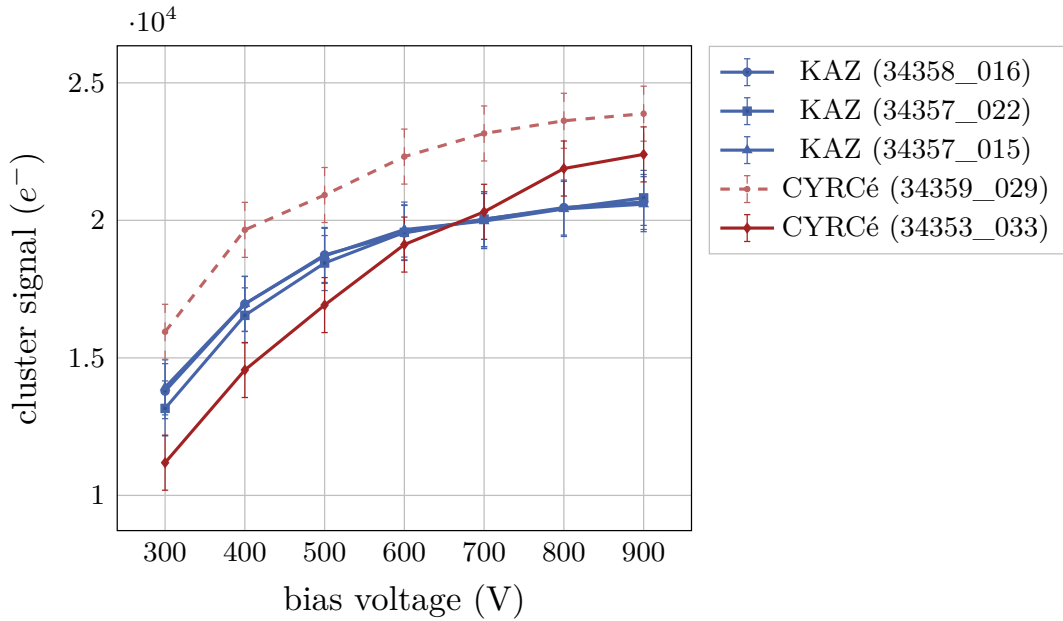
Figure 6.1.: Verification of the irradiation quality at the CYRCé cyclotron. Three samples have been irradiated to a fluence of $4.7 \times 10^{14}\, n_{\mathrm{eq}}/\mathrm{cm}^2$ at the KAZ cyclotron. Two samples have been irradiated to a fluence of $5 \times 10^{14}\, n_{\mathrm{eq}}/\mathrm{cm}^2$ at CYRCé. The failed irradiation is marked in pale dashed red.

A bias scan of the charge collection with these samples is shown in fig. 6.1. For the sake of completeness, the charge collection for the failed sample is indicated in pale red.

The samples irradiated at KAZ show a low variation regarding their charge collection. The total values are consistent with already known values for the charge collection at this fluence. As expected, the charge collection for CYRCé samples shows a strong relative deviation and the charge collection for the failed sample is higher than expected for a nominal fluence of $5 \times 10^{14}\, n_{\mathrm{eq}}/\mathrm{cm}^2$. The signal for the successful CYRCé sample lies close to the signal obtained for the KAZ samples, which is expected. However, the CYRCé sample's signal value is slightly lower than the values of the KAZ samples for voltages below 600 V but saturates at a higher value for higher voltages. No statement can be made about this phenomenon within the scope of this thesis since the number of samples is too low.

All in all, the CYRCé beamline provides a beam that delivers a fluence that is comparable to reference measurements obtained with the KAZ beamline despite a signal saturation value that is higher than expected. It can be used for iterative irradiation studies.

6.3. Leakage Current

IV curves are recorded during the course of iterative irradiation using the IIS. All presented measurements have been carried out at a temperature of $-20\,^{\circ}\mathrm{C}$ to prevent thermal runaway.

Figure 6.2 shows the obtained IV characteristics before each annealing step. As expected, the current rises after each irradiation step. For a fluence greater than $4 \times 10^{14}\, n_{\mathrm{eq}}/\mathrm{cm}^2$ a saturation behavior in the overall current is visible that diminishes for higher voltage values.

Figure 6.3 shows the obtained IV characteristics after each annealing step. Contrary to the IV characteristics before annealing, each curve after annealing saturates at $\approx 200\,\mathrm{V}$. The curve for $6 \times 10^{14}\, n_{\mathrm{eq}}/\mathrm{cm}^2$ shows a significant increase in current. This is likely due to this last annealing step being performed at ETP rather than the IIS. Consequently, the leakage
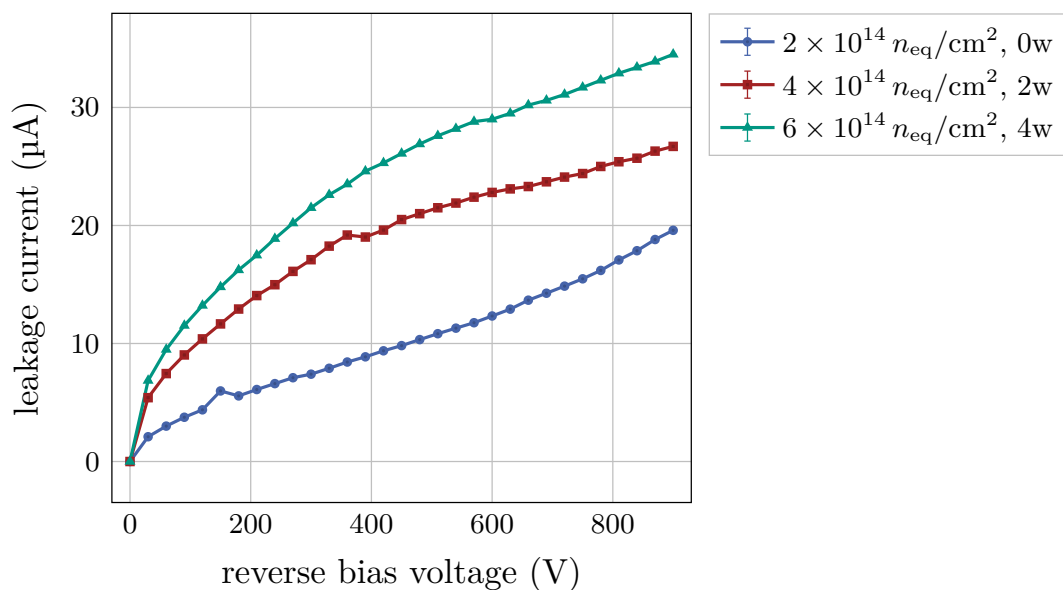
Figure 6.2.: IV characteristic curves before each annealing step at a temperature of $T = -20\,°\mathrm{C}$.
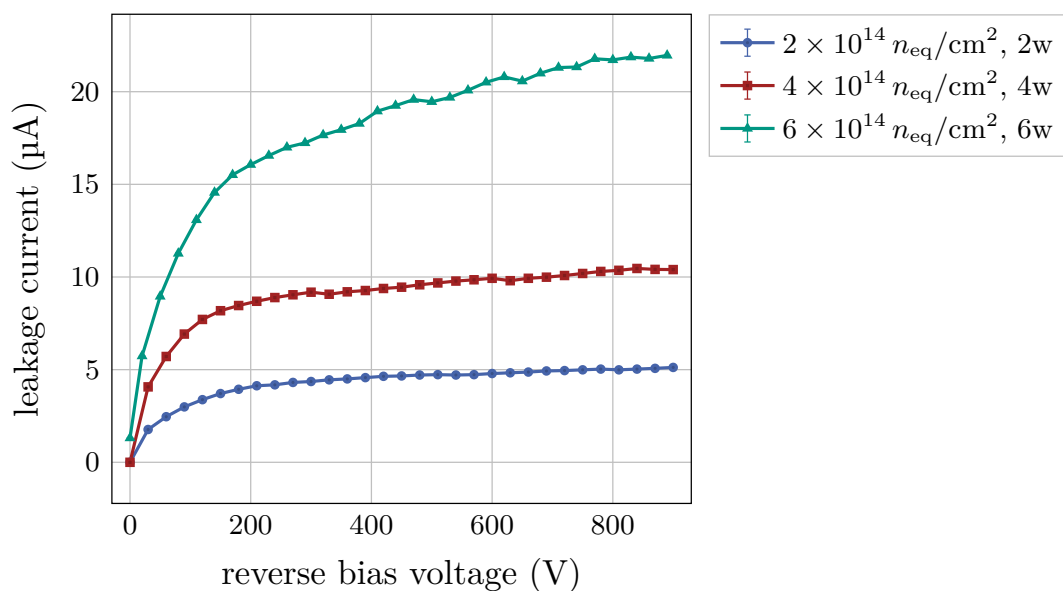

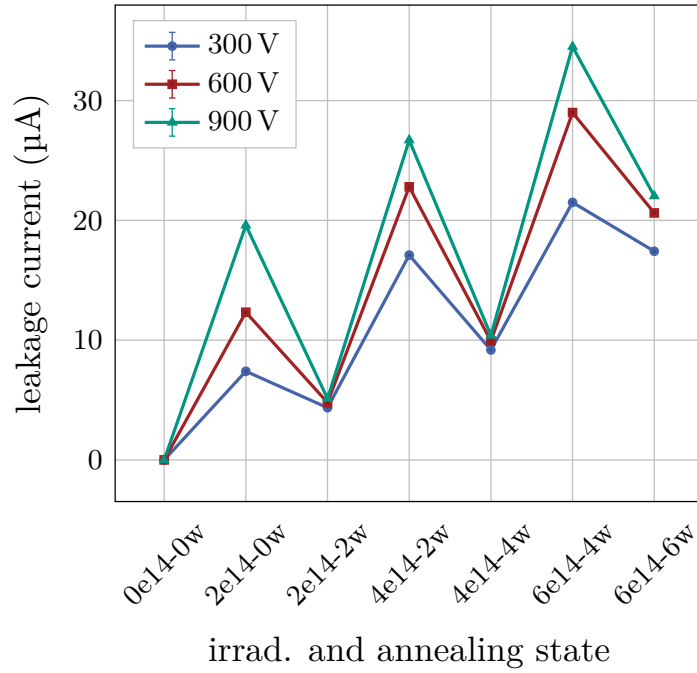**Figure 6.3.: IV curves after each annealing step** at a temperature of $T = -20\,°\mathrm{C}$.

Figure 6.4.: IV curves after each measurement step at a temperature of $T = -20\,°\mathrm{C}$. The x-labels state the irradiation fluence (in $n_{\mathrm{eq}}/\mathrm{cm}^2$) and annealing time (in weeks) for each data point.

current measurement of the last step has been performed using the ALiBaVa station. Change of setups, electrical connections/devices and using an oven rather than the IIS aluminium chuck for annealing could all affect the last measurement. A high voltage source with built-in picoammeter that was present at the CYRCé beamline has been used to record the presented leakage current measurements. The stationary ALiBaVa setup at ETP uses a dedicated picoamperemeter connected in series with the sensor and high voltage source. A calibration regarding the leakage current measurement needs to be performed in order to characterize this anomaly. Furthermore, one could benefit from measuring the temperature distribution of the IIS aluminium chuck for a given temperature. However, it is not expected to encounter a high temperature gradient throughout the aluminium chuck that could explain this kind of deviation.

Figure 6.4 illustrates the leakage current for selected bias voltages after each measurement step during the course of iterative irradiation. As expected, the leakage current decreases after each annealing step and increases after each irradiation step. The leakage current shows an overall uptrend during iterative irradiation, indicating that annealing for two weeks does not repair all irradiation damages inflicted upon the sensor. As previously described, a slight saturation behavior is visible for voltages below $900\,\mathrm{V}$. The data lacks statistical significance and does not allow for any interpretation regarding this saturation behavior. Future iterative irradiation studies need to increase statistics and the number of measurement steps.

The current related damage rate as a function of the equivalent annealing time can be parameterized with eq. (4.12). This parameterization is only valid for an annealing scenario with successive annealing periods after irradiation to a target fluence (*consecutive* scenario) Thus, it only applies to measurement steps where no irradiation has been performed after annealing. This only corresponds to the data point with a fluence of $2 \times 10^{14}\,n_{\mathrm{eq}}/\mathrm{cm}^2$ and $t_{\mathrm{ann}} = 2$ weeks. The experimentally determined damage rate in saturation (at $600\,\mathrm{V}$) for

Table 6.1.: Common mode and σ_{sig} values for different grounding configurations. The thermoelectric devices were turned off for all measurements. **PSU**: Exchanged mother board power supply, **DB**: Connected daughter board GND with HV GND, **Cu**: Connected pre-cooling copper bridge to GND.

Configuration	bias voltage (V)	CM (ADC)	σ_{sig} (ADC)
-	600	293	3.908
PSU	600	105	3.922
PSU+DB	500	44	4.667
PSU+Cu+DB	600	16	3.908

this step is $\alpha_{\text{dmg,ex}} = 3.457(203) \times 10^{-17}\,\text{A/cm}$ and is in accordance with the literature value $\alpha_{\text{dmg,lit}} = 3.454 \times 10^{-17}\,\text{A/cm}$.

To estimate the deviation of the theoretical consecutive damage rate $\alpha_{\text{dmg,lit}}$ from the experimentally determined iterative damage rate $\alpha_{\text{dmg,ex}}$, the datapoint with $4 \times 10^{14}\,n_{\text{eq}}/\text{cm}^2$ at an annealing time of 4 weeks is considered. This is the last data point that has been recorded using the IIS and can therefore be compared best. The experimentally determined damage rate $\alpha_{\text{dmg,ex}} = 3.584(211) \times 10^{-17}\,\text{A/cm}$ is 12% higher than the literature value of $\alpha_{\text{dmg,lit}} = 3.203 \times 10^{-17}\,\text{A/cm}$.

To compare the experimentally determined damage rate to literature, the measured current value has been scaled up to room temperature using eq. (4.5). The systematic uncertainty introduced by the PT1000 temperature sensors is specified as $0.5\,°\text{C}$ (full-range). To cope with non-linearities while propagating the error with eq. (4.5), a Monte-Carlo based method is employed. $1\,000\,000$ nomally distributed random numbers have been generated around the temperature value with a standard deviation that corresponds to the specified systematic error. The standard error of the resulting $I(T_0, I_0, T)$ - distribution is taken to be the systematic uncertainty of the current value used to calculate the damage rate. The asymmetry of the T_0 distribution is negligibly small and thus, has been omitted above.

Damage rates for the remaining steps are not comparable to any literature values and lack significance to develop a model describing the underlying data. As previously, future iterative irradiation studies need to increase statistics in order to develop a parameterization of the current-related damage rate with respect to the equivalent annealing time.

6.4. Charge Collection

Charge collection of Babysensors has been measured prior to irradiations using the IIS.

During development and characterization of the IIS, an unusually wide common mode (CM) noise distribution has been noticed. To investigate this phenomenon, different grounding configurations were attempted. In the following, the CM value is defined as the standard deviation of the Gaussian CM noise distribution (shown in fig. 6.5). All examined grounding configurations are listed in table 6.1. It is easy to see that the IIS is sensitive to proper grounding connections and a properly interference-supressed power supply unit for the ALiBaVa motherboard. Grounding does not raise the noise for charge collection measurements σ_{sig} significantly and thus, the PSU+Cu+DB configuration should be employed at all times. Furthermore, common mode seems to be influenced by electromagnetic interference caused by Peltier power cables running underneath the aluminium chuck. Future upgrades of the IIS should respect appropriate routing of unshielded cables in order to reduce noise at the readout
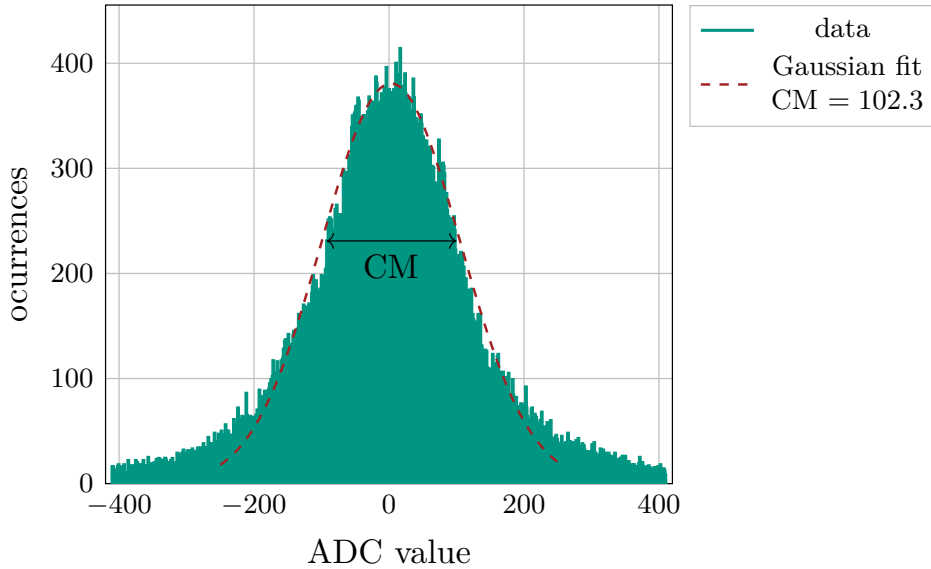
Figure 6.5.: Examplary common mode distribution for the PSU grounding scheme (see table 6.1 for a list of all grounding schemes). The standard deviation of the fitted gauss function is taken to be the CM value.

electronics. Different *RC*-values for HV filtering have to be investigated in future studies in order to characterize the influence of ripple filtering of the HV PSU.

Using the PSU+Cu+DB grounding scheme, a bias scan of signals ranging from a bias voltage of $300\,\text{V}$ to $600\,\text{V}$ is measured. The measurements are carried out at room temperature, with no temperature control enabled, since the sensor has not yet been irradiated. A cluster signal of $22\,773(500)\,\text{e}^-$ is measured and is compatible with the expected signal value for a sensor of active thickness $290\,\mu\text{m}$ (see section 4.5).

7
Summary and Outlook

To investigate the effects of iterative irradiation and annealing compared to consecutive annnealing scenarios, an Iterative Irradiation Setup (IIS) has been designed. With a dedicated XZ stage, it features spatial translation on two axes. This to uniformly irradiate larger sensors with a small beam spot by applying a scanning procedure.

A feasible thermal concept is paramount to reproducible and stable performance of iterative irradiation tests. In order to estimate the thermal performance of the cooling and annealing concept prior to production, steady-state finite-element thermomechanical simulations are employed. A test of thermal performance was performed using a real-world mockup. Comparable components regarding size and material properties were used. The results obtained with the simulation and real-world emulation indicate, that the annealing temperature can be reached with sufficient stability. After production of the IIS, as expected, the thermal performance for cooling and heating was satisfactory.

User interaction with the setup is accomplished by means of a self-written web interface based on the VueJS framework and the already present MeasurementControl back end. The graphical user interface features views for controlling and monitoring thermal performance, translation and other relevant telemetry.

In order to irradiate a sensor to a desired fluence, the scanning speed in x-direction v_x has to be known as precisely as possible. After calibration of microstep to distance translation of the motor stage, v_x is verified using a dedicated calibration procedure. The error on the irradiation fluence caused by the uncertainty on v_x was found to be on the sub-percent level.

Before carrying out the iterative irradiation procedure as part of a beam test at the CYRCé CMS beamline, properties of irradiations with the CYRCé cyclotron was verified by irradiating two sensors to a target fluence of $5 \times 10^{14} \, n_{eq}/cm^2$ and comparing the charge collection of theses sensors with reference measurements. Because of a technical fault, it was not possible to conduct charge collection measurements after irradiation. However, the scanning irradiation and annealing procedure, as well as IV curve measurements were carried out successfully. Prior to irradiation, signal measurements yield the charge expected for the type of sensor that was examined. IV measurements prior to and after the iterative irradiation procedure were obtained. As expected, the leakage current rises after each irradiation step and falls after each annealing step, exhibiting an overall uptrend over the course of the measurements.

In conclusion, iterative irradiation procedures were successful, albeit missing charge collection measurements. The proof of concept has been demonstrated and future iterations of the setup should aim for streamlining the conceptual design, safer handling of sensors and electronics, as well as increasing statistics for existing measurements.

Part II.

Online Beam Monitoring with an Ionization Chamber

8

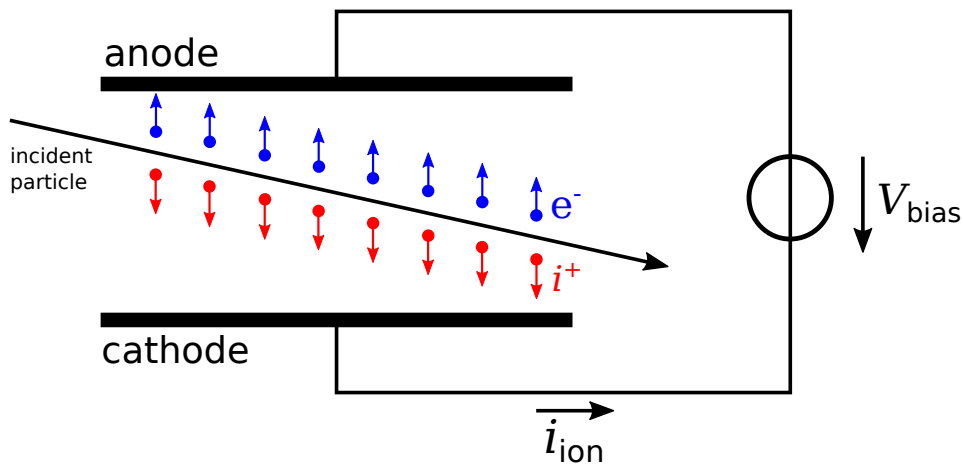# Theory of Particle Detection with Ionization Chambers

Figure 8.1.: Schematic of a parallel plate ionization chamber. The bias voltage is applied across two parallel plate electrodes. Ion pairs drift along the electric field and are detected by external readout electronics. An ion current i_{ion} is measured.

This chapter briefly discusses the theoretical background that is needed to understand the results obtained in this part of the thesis. Although there is a multitude of different gaseous detector types, each useful for different purposes, this part is centered around ionization chambers.

8.1. Introduction to Ionization Chambers

Charged particle detection with silicon devices has already been covered in the first part of this thesis. As for silicon devices, detection of radiation using ionization chambers is based on separation of ionized charges created by the incident particle. Depending on the medium's ion pair generation energy w and incident particle properties, a certain number of ion pairs per unit length is ionized along the path of the particle. For dry air at room temperature, the ion pair generation energy is $w = 34\,\mathrm{eV/ion}$ pair. A polarization voltage (referred to as *bias voltage* from here on out) is responsible for separation of these ion pairs. Ion pairs can drift along the electric field generated by this bias voltage and be collected at the electrodes. The voltage potential is applied across two electrodes. Their form is dictated by the geometry of the ionization chamber. The simplest case is the parallel plate ionization chamber (PPIC). A schematic of such a PPIC is shown in fig. 8.1. Two parallel plate electrodes define the electric field. The active volume consists of a certain medium, which may or may not be pressurized.
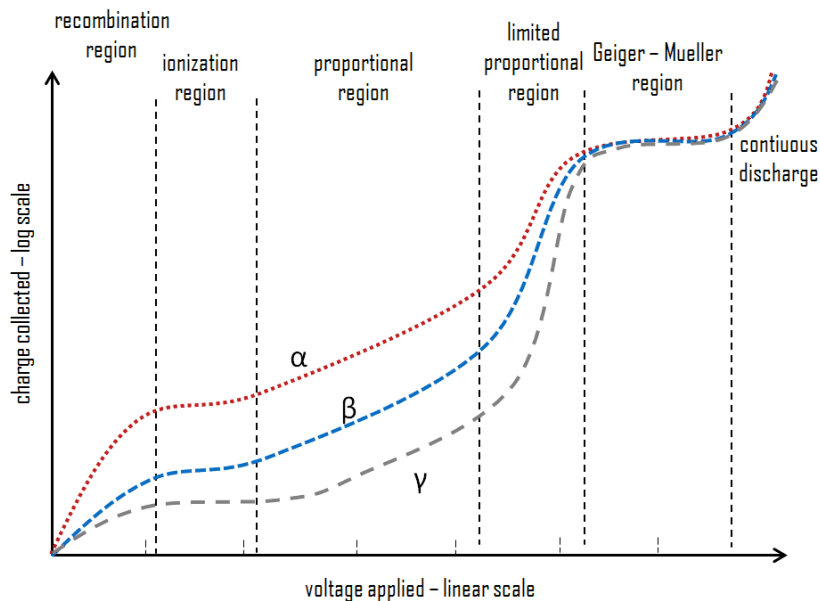
Figure 8.2.: Theoretical ionization current against the applied bias voltage. An ionization chamber is typically operated in the *saturation region*. For low bias voltages, the detector is operated in the *recombination region* [Eve].

Ionization currents supplied by the ionization chamber are dependent on beam properties and the active chamber width but, typically, are very small (1 nA or even less). Therefore, low-noise pre-amplifiers are paramount to their operation.

8.2. Operation Modes of Gaseous Detectors

Charge collection in a gaseous detector such as an ionization chamber is dependent on the strength of the electric field generated by the electrodes. For ionization chambers, only two modes of operation are encountered. For the sake of completeness, however, all possible operation modes will be covered in the following.

Figure 8.2 shows the theoretical ionization current against the applied bias voltage. Depending on the applied bias voltage, different modes of operation are possible for a gaseous detector.

In the **recombination region**, the electric field is not strong enough, to separate the constituents of all ion pairs. Ion recombination is predominant and only a small fraction of charges reach their respective electrodes.

The current saturates if the detector is operated in the **saturation** or **ion chamber region**. Ion recombination becomes negligible and all charges may be collected without loss. An increase in voltage does not cause a significant increase in collected ion charge since the voltage is not high enough to cause secondary ionization. Typically, ionization chambers are operated in this mode.

In the **proportional region**, the applied bias voltage is large enough to accelerate primary ions to sufficient energies so that they can ionize additional atoms of the medium. The detector is typically operated at a constant and well-defined voltage so that the number of secondary ions is proportional to the number of primary events. Let n be the number of ion pairs collected at the electrodes and n_{prod} denote the number of produced ion pairs. Then, the

gas amplification factor g (or *gain*) is

$$g = \frac{n}{n_{\text{prod}}}.$$

If the voltage is increased to even higher values, every primary ionization causes multiple so-called *Townsend avalanches* to occur. This region is called the **Geiger-Müller region**. Primary avalanches cause secondary avalanches to emerge by ultraviolet photonic emission. The result is the generation of a signal with strong amplitude, which is independent of the primary ionization.

Increasing the voltage substantially, the immensely high electric field will cause the active medium to discharge continuously. This mode is called the **discharge region** and is not used for detection of ionizing radiation.

In the following, the **recombination and saturation regions** will be encountered during the discussion of experimental results.

8.3. Ion Recombination in Continuous Beams

The main cause of ion collection deficiency of ionization chambers is ion (pair) recombination loss. Ion recombination is a process in which mobile charge carriers created by incident particle tracks are eliminated. The phenomenon is usually divided into two categories: initial and general (volume) recombination.

In the theory of columnar recombination, Jaffé assumes that the clouds of positive and negative charges created by one incident particle are distributed cylindrically symmetric around its track [Jaf40]. Later on, the charges diffuse and undergo initial recombination, therefore the partial differential equation

$$\frac{\mathrm{d}n}{\mathrm{d}t} = D\nabla^2 n - \alpha n^2,$$

where

n is the charge carrier density and

α and D denote the recombination and diffusion coefficients respectively,

has to be solved.

With regards to initial recombination, Jaffé finds initial recombination to be inversely proportional to the applied electric field E

$$\frac{i_{\text{sat}}}{i_V} \propto E^{-1} \propto V^{-1},$$

with i_{sat}, the saturation current of the ionization chamber, i_V the ionization current measured near saturation at a bias voltage V. Based on this theory, a so-called *Jaffé plot* may be employed in order to characterize intial recombination of the ionization chamber in question. If initial recombination dominates the recombination process, the obtained Jaffé plot should be linear.

General recombination is assigned to volume recombination of charges and thus is not limited to one particle track only. In general, the effect is dependent on many different parameters such as medium properties, incoming beam intensity and chamber type and may be approximated by an inversely quadratic relationship with respect to the bias voltage V,

$$\frac{i_{\text{sat}}}{i_V} \propto E^{-2} \propto V^{-2}.$$

If general recombination dominates the recombination process, plotting $1/i_V$ against $1/V^2$ should yield a straight line.

8.4. Introduction to the SRIM Software Suite

SRIM (short for *The **S**topping and **R**ange of **I**ons in **M**atter*) is a software suite that is used to simulate the stopping power and range of ions in matter [Zie]. The problems are treated quantum mechanically. Targets may be defined layer-wise with each layer being characterized by its density, depth along the incident particle beam, atomic properties and state of matter. The incident particle beam is characterized by its energy and intensity in the simulation. In the following, the energy loss of protons in air will be calculated using the SRIM software suite.

8.5. Introduction to SPICE

SPICE (or ***S**imulation **P**rogram with **I**ntegrated **C**ircuit **E**mphasis*) is an analog electronic circuit simulator. It features different kinds of analyses, including (but not limited to) small-signal linearized frequency domain analysis (AC analysis), quiescent point analysis (DC analysis) and time domain large-signal analysis (transient analysis) [Vla21]. Integrated circuits are described by their macromodels that implement all relevant properties to model their behavior.

In the following, transient as well as DC analyses are employed to model the voltage response of a transimpedance amplifier circuit to a test current.

Conception and Simulation
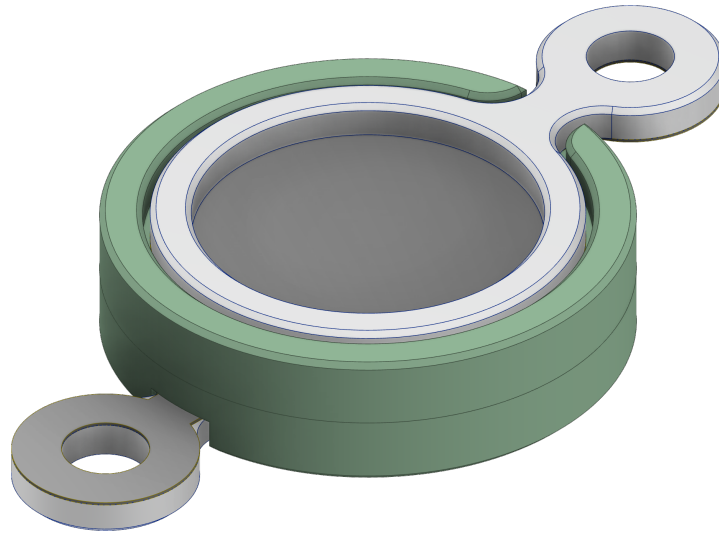
Figure 9.1.: Mechanical design of the PPIC. The simple design provides robustness and production efficiency.

9.1. Motivation

Past experiences at the KAZ beamline with regard to current stability during irradiation procedures have emphasized the need for non-destructive online beam monitoring. Various possibilities are eligible to accomplish this goal. Beam pickups that work by induction of a current proportional to the beam current cannot be installed in close proximity to the sample to be irradiated. Furthermore, they need to be installed very close to the beam which requires very fine control over the proton beam and a sufficiently high beam current, which makes this solution unattractive.

Instead, beam monitoring by usage of an ionization chamber has been selected. Advantages of this solution include (but are not limited to)

- customized chamber and pre-amplifier production,

- time and cost efficiency and

- suitable solutions for different beamlines and fields of application.

New challenges emerge from the employment of an ionization chamber, albeit its versatility. As discussed in section 8.1, ionization chambers generally generate a very faint signal, and thus, require low-noise amplification. Typically, amplifiers that are capable of detecting such a low current are expensive. Therefore, operating them at a proton beamline where stray neutrons
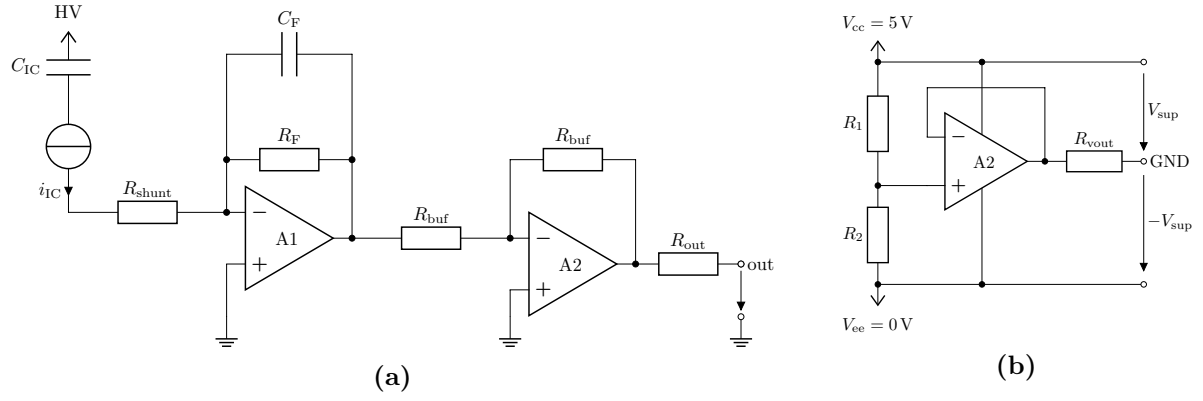
Figure 9.2.: The ion current amplification circuit. a) The transimpedance stage amplifies the ion current in an inverting configuation. The following buffer stage inverts the signal and yields a low-impedance output. b) Circuit providing a virtual ground for all OpAmps.

may lead to SEL or even activation of the device is out of the question. A low-cost solution has to be invented that yields a linear amplification and can be read out externally during operation of the particle beam.

In summary, an online beam monitoring device with a low-noise, cost effective amplifier circuit has to be invented.

9.2. Conception

A parallel-plate ionization chamber (PPIC) will be used to carry out the measurements. It is shown in fig. 9.1. Depending on the chamber version during R&D and its field of application, the chamber housing is made from either 3D-printed acrylonitrile butadiene styrene (ABS) (ICv1 and ICv2) or glass-reinforced plastic (GRP) (ICv3). The plate electrodes are either made from PET encoated with graphite (ICv1) or aluminium-encoated Kapton$^{©}$ foil (ICv2 and ICv3).

Readout of the ion chamber will be accomplished by cascading

- electronic amplification of the read out ion current,

- digitization of the amplified signal and

- transmission of telemetry to the outer world.

The amplification circuit is shown in fig. 9.2a. It consists of two stages. The first stage is a transimpedance amplifier (TIA) in an inverting configuration. R_{shunt} converts the ion current i_{IC} into a voltage that is amplified by a factor of

$$g_{TIA} = -\frac{R_{shunt}}{R_F}.$$

Therefore, it pre-amplifies the ion current from the PPIC with a gain of g_{TIA}. Usage of the feedback capacitance C_F shifts the cutoff frequency towards higher values and provides transient stabilization. The following buffer stage inverts the TIA signal at unity gain and yields a low-impedance output with a range that is suitable for following analog-to-digital conversion (ADC). Biasing all used operational amplifiers is accomplished by means of a virtual ground circuit shown in fig. 9.2b. Loading effects should be negligibly small.

Table 9.1.: Target geometry used for SRIM simulation.

Layer	width	phase
Kapton foil	25 μm	solid
Aluminium	65 nm	solid
Dry Air	6 mm	gaseous
Aluminium	65 nm	solid
Kapton foil	25 μm	solid

The ADC is accomplished by usage of a Raspberry Pi Pico™ microcontroller. It features a 12 bit successive approximation (SAR) ADC (quantization level: 4096). With a 96 CPU clock cycle approximation rate and a CPU frequency of 48 MHz, the sampling frequency is approximately 500 kS/s. The input-inferred noise lies at ≈ 1.1 mV and will be used as the uncertainty of the digitized signals.

9.3. Simulation

The produced ionization chamber shall be tested at the CYRCé beamline. At a maximum beam current of 100 nA and proton energy of 23 MeV, the ion current generated in the chamber may be calculated by simulating the ionization energy loss using SRIM.

Constituents of the target geometry are listed in table 9.1. In the simulation

$$\frac{\mathrm{d}E}{\mathrm{d}x} = 2.4 \, \frac{\mathrm{eV}}{\mathrm{\mu m}},$$

is obtained for the energy loss of 23 MeV protons in dry air at room temperature. Using an air ionization energy of $w_{\mathrm{air}} = 35$ eV, for a chamber with an active width of d

$$i_{\mathrm{IC}} = \frac{\mathrm{d}E}{\mathrm{d}x} \cdot \frac{d}{w_{\mathrm{air}}} \cdot i_{\mathrm{beam}} \tag{9.1}$$

holds for the expected ion current. At active widths of $d = 3, 6$ and 8 mm, the ideally expected ion currents i_{IC} are 20.57, 41.1 and 54.9 μA respectively. Recombination effects could not be simulated using the SRIM software suite.

For the amplifier circuit, a SPICE simulation is performed. The input models for both revisions used in this thesis are shown in table 9.2. To model the ionization chamber in the SPICE simulation, it has been substituted by a capacitance C_{IC} and an ideal current source, sourcing the ion current i_{IC}. The capacitance C_{IC} has been calculated by considering the dimensions of the CAD model. The magnitude of recombination effects could not be estimated beforehand. Therefore, the resistor values of Revision C have been chosen, so that the maximum ion current for an active chamber width of 6 mm covers the full ADC range without clipping. This means that an ion current of $i_{\mathrm{IC,max}} = 41$ μA (see eq. (9.1)) corresponds to the maximum ADC voltage of 2.31 V. Resistor values for Revision B of the circuit have been determined empirically.

The simulated characteristic of the amplifier circuit (Rev. C) is shown in fig. 9.3. For the characteristic, a transient simulation has been performed. A current source simulating the ion current is swept from 0 μA to 41 μA and the signal output of the amplifier is displayed. The characteristic does not clip in the selected signal region.

Table 9.2.: Input model to the SPICE simulation.

Component	Rev. B	Rev. C
R_{shunt}	$30\,\text{M}\Omega$	$68\,\text{k}\Omega$
R_{F}	$1\,\text{G}\Omega$	$56\,\text{k}\Omega$
R_{buf}	$15\,\text{k}\Omega$	$68\,\text{k}\Omega$
R_{out}	$0\,\Omega$	$100\,\Omega$
C_{IC}	$0.76\,\text{pF}$	$0.76\,\text{pF}$
C_{F}	$12\,\text{pF}$	$12\,\text{pF}$
R_1	$100\,\text{k}\Omega$	$100\,\text{k}\Omega$
R_2	$100\,\text{k}\Omega$	$100\,\text{k}\Omega$
R_{vout}	$0\,\Omega$	$100\,\Omega$
$A1$	LMP7721	LMP7721
$A2$	TS912	TS912
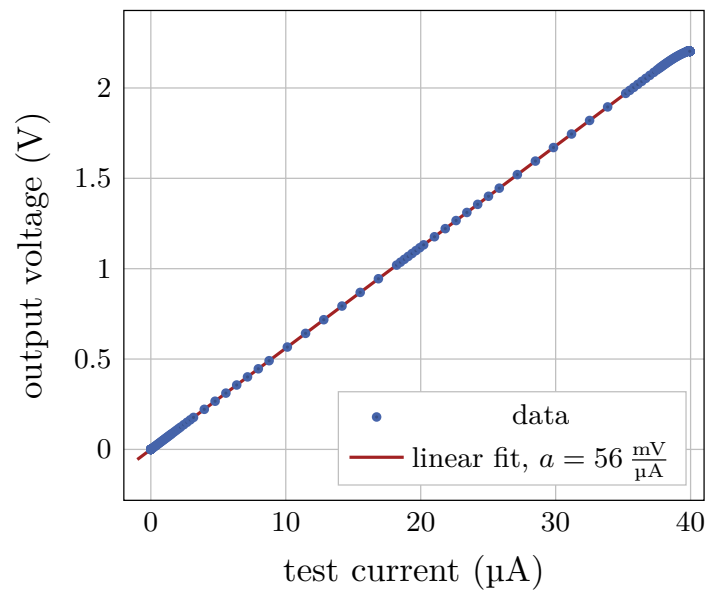
Figure 9.3.: Simulated characteristic of the amplifier (Rev. C). It is easy to see that the signal response is linear over the full ADC range and does not clip.

Experimental Results

(a)

(b)
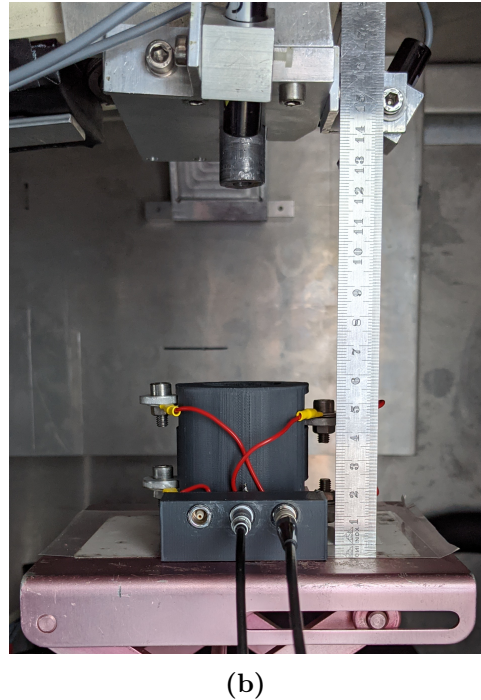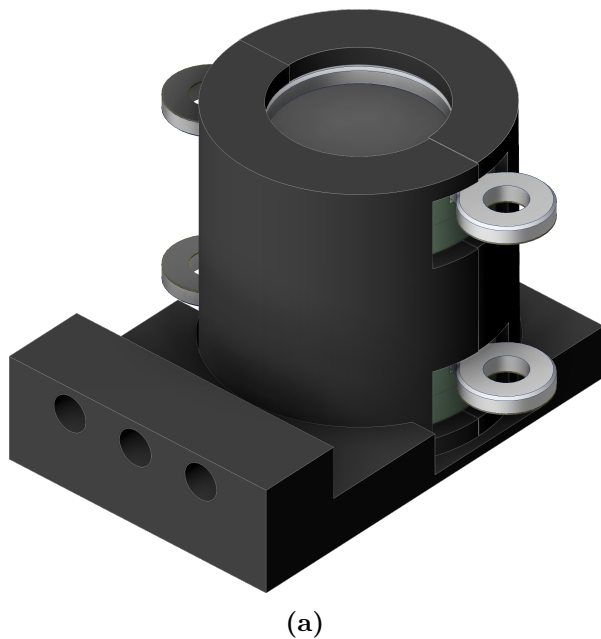
Figure 10.1.: a) CAD drawing of the characterization support structure. b) Two ionization chambers (ICv2) inside of the characterization support structure positioned below the X-ray tube's colimator.

This chapter will present the results obtained for the previously presented ionization chamber and amplifier circuit.

10.1. Setup

A brief description of the experimental setups used at both irradiation facilities will be given in the following section.

10.1.1. X-Rays

The X-ray tube at ETP is used to irradiate the ionization chambers with X-rays. For fixation and characterization of transmitted intensity loss, a characterization support structure was built. Transmitted intensity should be characterized to ensure that the device under test, which is located behind the ionization chamber, receives the desired irradiation fluence. It is shown in figures 10.1a and 10.1b. It is able to hold two chambers with maximum active widths of 12 mm. The X-ray beam is aligned with the ion chambers by eye using a flourescent target. It

(a)

(b)
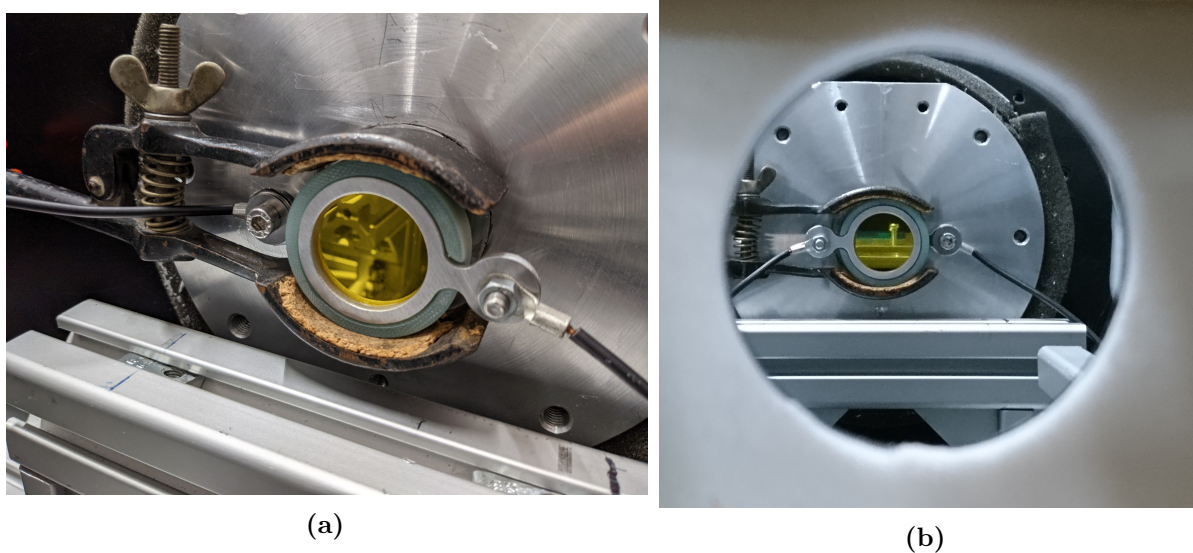
Figure 10.2.: a) An ionization chamber mounted in front of the beam entrance to the irradiation box. A beam dump made of tantalum is inserted behind the chamber (not visible in the picture). b) An IC aligned with the beam.

is aligned perpendicular to the X-ray beam. The chambers that were used have a diameter of 30 mm, which is significantly wider then the X-ray beam spot, which has a width of 1 cm to 2 cm [Gut+12]. The distance between the upper edge of the characterization support structure and the X-ray collimator is 8 cm.

10.1.2. Protons

For the characterization of one chamber, it is inserted into a vice which is positioned in close proximity to the beam entrance into the irradiation box present at the beamline (as seen in fig. 10.2a). It is aligned with the beam spot by usage of an optical telescope whose line of sight is aligned with the beam, which is shown in fig. 10.2b. A 23 MeV proton beam with variable intensity is directed at the chamber. The chambers that were used have a diameter of 30 mm, which is significantly wider then the proton beam spot, which has a FWHM of approximately 8 mm. The center of the IC is aligned perpendicular to the proton beam using the vice and the walls of the irradiation box as alignment aids. A low-side current measurement using the HV supply's built-in picoammeter as well as an amplifier readout is performed.

10.2. Amplifier Response

Before application in the beam the custom amplifier has to be validated. For this purpose, a constant current source is connected to the input of the amplifier and the output is recorded. Two revisions of the amplifier circuit are characterized.

10.2.1. Revision B

Revision B of the amplifier circuit has been developed for use with the X-ray setup only. As it has been developed early on in the R&D process, with just the proof of concept in mind, the chosen resistor values needed improvement. Since the feedback resistance R_F has been set to a high value, the strong feedback path led to high frequency instabilities. Ripples of
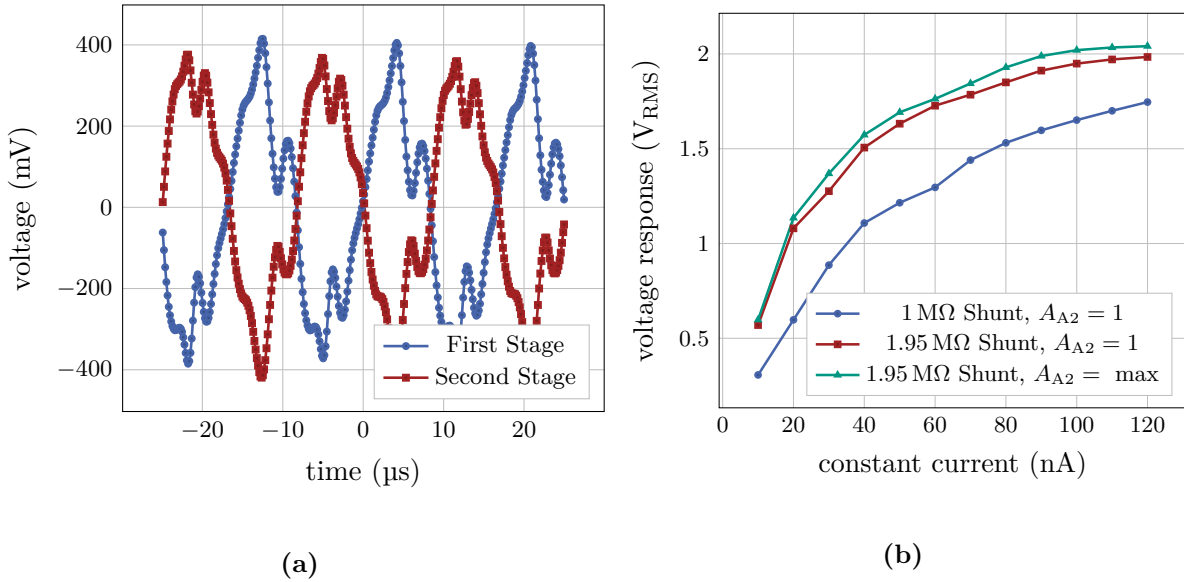
(a)

(b)

Figure 10.3.: Oscillation issues with Rev. B of the amplifier circuit. a) Voltage response over time at the output of both amplifier stages at no input. b) RMS VI characteristic of Revision B. Nonlinearities are clearly visible.

the HV supply and grounding issues led to oscillations in the output at a flat input, as can be seen in fig. 10.3a. As expected, however, the output voltages of both stages are mirrored with respect to each other. Nonlinearities in the voltage response over the input current (VI characteristic) are clearly visible for all different edge cases regarding the gain factors of both stages. These nonlinearities are remedied by proper grounding and ripple filtering. The result is a distortion-free, linear characteristic shown in fig. 10.4a. Minor clipping effects occur at the edge of the recorded range.

10.2.2. Revision C

Revision C of the amplifier circuit has been developed to primarily fix the oscillation issues of Revision B. Decoupling capacitors have been added to the power rails of all operational amplifiers. They have been omitted from the schematics for the sake of clarity. Additionally, different resistor values have been chosen in adjustment to the increased ion current protons generate in the detector. X-rays (produced with the tube at ETP) only generate a maximum ion current of around 80 nA. As shown in eq. (9.1), 100 nA of 23 MeV protons (produced at CYRCé), however, are expected to generate a signal of up to 41 µA. Revision B of the circuit only included the analog amplifier circuit on its PCB, relying on external digitization. Revision C fixed this by integrating digitization and analog amplification on the same PCB.

The VI characteristic of the Revision C amplifier can be seen in fig. 10.4b. Its voltage response is linear with no saturation effects visible even close to output voltage swing. Within component tolerances, the experimentally determined gain of 58.45(1) mV/µA is in accordance with the simulated gain of 56 mV/µA seen in fig. 9.3.

In summary, both Revision B (after fixing the oscillation issues) as well as Revision C are operable and sufficiently linear in the relevant range. The experimentally determined gain factor of Revision C confirms the simulation.
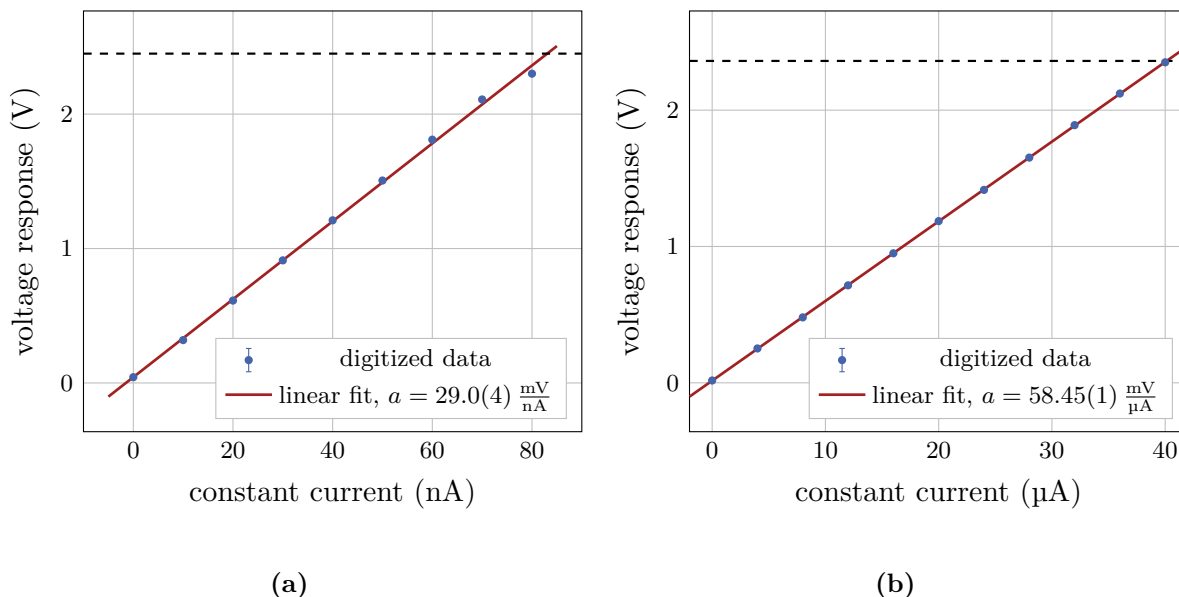
(a)

(b)

Figure 10.4.: Digitized VI characteristics of the amplifier circuit. The output voltage swing is indicated by a black dashed line. The voltage responses are linear. a) shows the characteristic for Rev. B. Minor saturation effects occur due to clipping. b) shows the characteristic for Rev. C.

10.3. Chamber Characteristics

This section presents results obtained for the characterization of ionization chambers at two different irradiation facilities.

10.3.1. X-Rays

Irradiations with X-rays have been carried out using the X-ray tube at ETP (see section 3.2). The presented characterizations have been performed for ICv2 and Rev. B of the amplifier. Two ionization chambers with an active width of 6 mm are inserted into the characterization support structure (IC_v2_01 on the top, IC_v2_02 on the bottom level) and read out simultaneously.

Bias Voltage Scans

The bias voltage of both chambers is scanned and the digitized voltage response is recorded in fig. 10.5a. A fixed tube current of 30 mA is used. Both ionization chambers saturate in the recorded range. Different saturation currents can not be explained by intensity loss after the first chamber, since the top chamber has a lower saturation current than the bottom chamber. Most likely, production quality as well as connection to the readout electronics cause an offset between the saturation currents. The saturation curve for IC_v2_02 hits upper voltage swing at a bias voltage of approximately 220 V. The signal is therefore clipped.

Tube Current Scans

The X-ray tube current is scanned and the digitized voltage response for both chambers is recorded in fig. 10.5b. To operate both chambers at peak collection efficiency, a fixed bias voltage of 350 V is set. As expected, both chambers yield a linear output. IC_v2_01 exhibits a
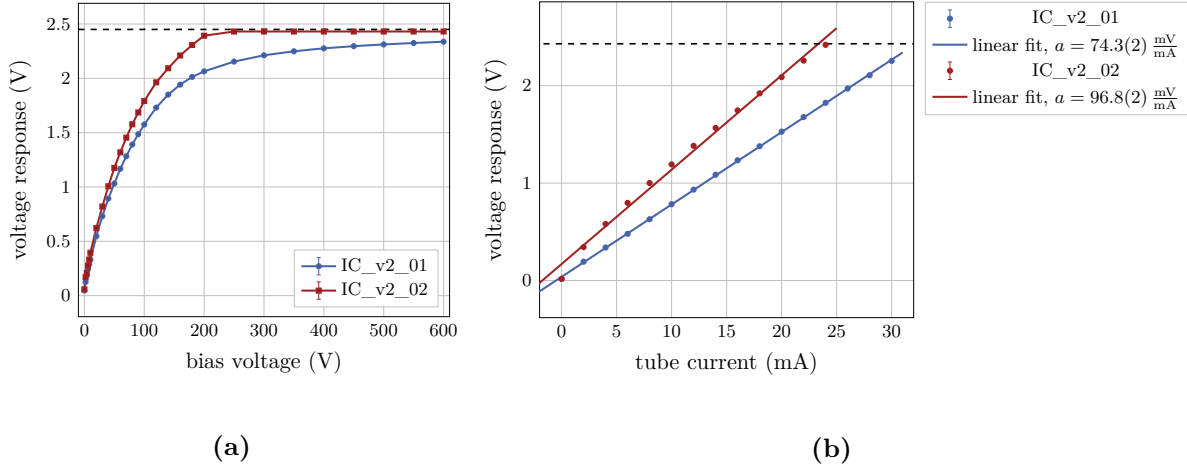
Figure 10.5.: Characterization of two cascaded ICv2. An active width of 6 mm is used. a) shows a bias voltage scan at constant X-ray tube current of 30 mA. b) shows a tube current scan at a constant bias voltage of 350 V.

smaller slope than IC_v2_02. This corresponds to the offset in saturation current discussed in the previous section. A greater saturation current means that the charge collection is higher.

Summing up, both chambers as well as the amplifier circuit perform as expected. The difference in saturation currents between the characterized chambers could be a remnant of production quality as well as differences in how the chambers are connected to the readout electronics.

10.3.2. Protons

Irradiations with 23 MeV protons have been carried out over the course of a beam test at the CMS beamline of CYRCé. Two different active widths (3 mm and 8 mm) were examined.

Bias Voltage Scans

Bias scans for the 3 mm chamber are performed and the digitized voltage response as well as the picoammeter reading is recorded in figures 10.6a and 10.6b. The beam current is fixed at $i_{\text{fix}} = 50$ nA. Intermittently, a faradey cup is inserted into the beam path to monitor its intensity during the measurement. Deviations from i_{fix} are corrected for. Measurement points at which such corrections were performed are indicated in the plots.

In contrast to the measurements conducted with X-rays, the chamber current does not saturate in the recorded range. The ammeter and amplifier readings are in agreement with each other. Under the assumption that the ammeter provides an accurate reading, the amplifier seems to yield an undistorted measurement of the ion current.

Bias scans for the 8 mm chamber are performed and the digitized voltage response as well as the picoammeter reading is recorded in figures 10.7a and 10.7b. The beam current is fixed at either $i_{\text{fix}} = 50$ nA or $i_{\text{fix}} = 75$ nA. A faradey cup did not need to be inserted since the measurement was conducted at a fast enough pace.

As in the case of the 3 mm chamber, the 8 mm chamber does not saturate in the recorded region. At a beam current of 50 nA, the 8 mm chamber induces a smaller ion current than the 3 mm chamber. This indicates that the electric field is too low to separate the generated charges properly for a larger active width. In saturation, the 8 mm chamber would — in
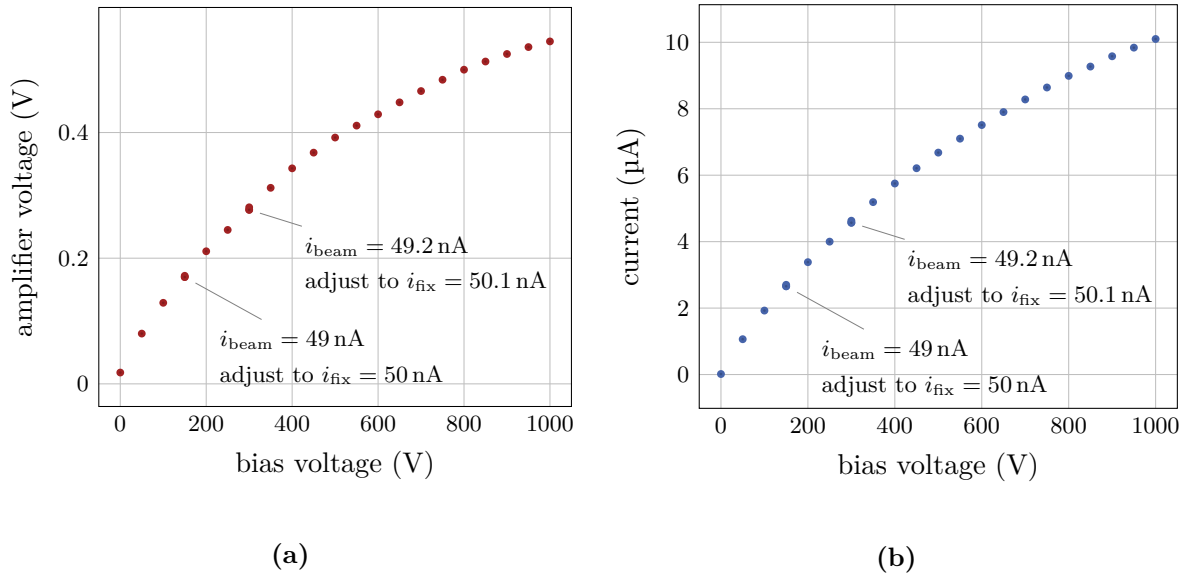
(a)

(b)

Figure 10.6.: Bias voltage scan of the 3 mm chamber. The beam current is fixed at 50 nA. Annotations indicate the correction of the beam intensity at selected measurement points. The error bars are smaller than the measurement points. a) shows the amplifier voltage response. b) shows the picoammeter reading.
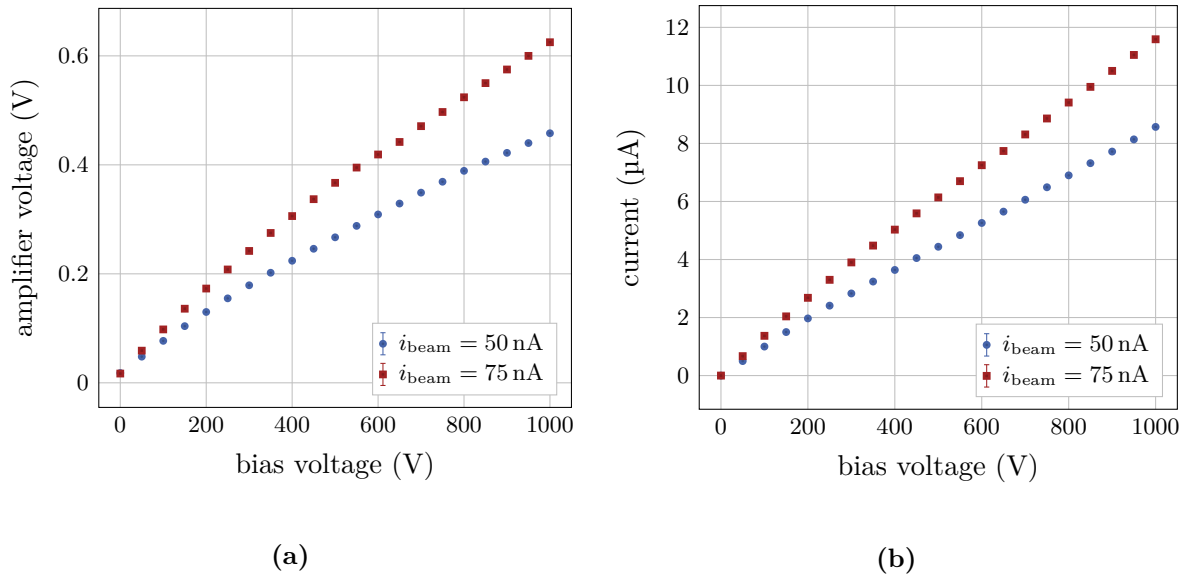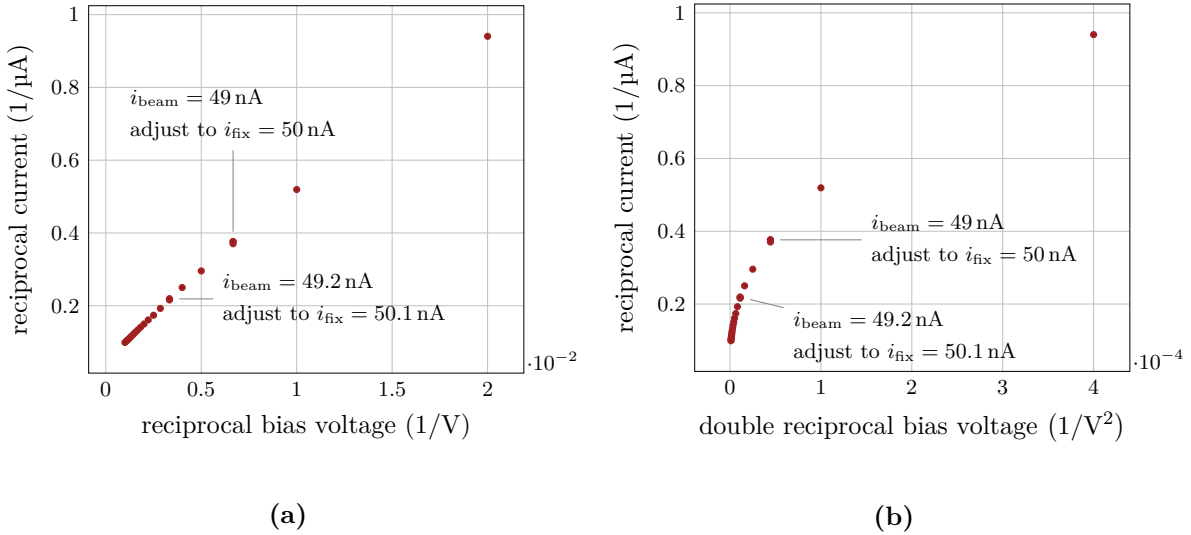

(a)

(b)

Figure 10.7.: Bias voltage scan of the 8 mm chamber for beam currents of 50 and 75 nA. The error bars are smaller than the measurement points. a) shows the amplifier voltage response. b) shows the picoammeter reading.

(a)

(b)

Figure 10.8.: Recombination processes for the 3 mm chamber. The error bars are smaller than the measurement points. a) shows the Jaffé plot. b) shows the $(1/V^2)$-plot. The Jaffé plot is linear, which means that intitial recombination is predominant.

theory — provide a much greater ion current than the 3 mm chamber. The ammeter and amplifier readings are, again, in agreement with each other.

Recombination

As outlined in section 8.3, it is possible to tell recombination mechanisms apart by the usage of Jaffé- and $(1/V^2)$-plots. Data obtained by the bias scan presented in the previous section has been taken for this purpose. For a chamber width of 3 mm, these plots are shown in figures 10.8a and 10.8b. A straight line could be fitted through the data presented in the Jaffé plot, while for the $(1/V^2)$-plot it cannot. Therefore, initial recombination seems to dominate the recombination process for the 3 mm chamber.

The recombination plots for the 8 mm chamber are shown in figures 10.9a and 10.9b. As is the case for the 3 mm chamber, recombination for the 8 mm chamber seems to be mainly due to initial recombination. The recombination rate for a beam current of 50 nA is slightly higher than for 75 nA, since the the slope is greater.

Comparing the Jaffé plot slopes of both active widths (shown in fig. 10.8a and fig. 10.9a) by eye, it can be concluded that the recombination rate for the 8 mm chamber is higher.

Beam Current Scans

In figures 10.10a and 10.10b, the proton beam current is scanned from 0 nA to 100 nA and the amplifier voltage response is recorded. Since — as already discussed — no saturation can be reached for both examined chambers, the bias voltage is set to the maximum value of 1000 V. Therefore, peak collection efficiency cannot be achieved.

The 3 mm chamber exhibits a mostly linear response with respect to the beam current. Deviations from an exactly linear behavior can be explained by operation of the chamber in the recombination region.

For a beam current of 100 nA, an ion current of

$$i_{\mathrm{IC}} = \frac{V_{\mathrm{3mm}}}{V_{\mathrm{ADC,max}}} \cdot i_{\mathrm{IC,max}} = \frac{1\,\mathrm{V}}{2.31\,\mathrm{V}} \cdot 41.1\,\mu\mathrm{A} = 17.8\,\mu\mathrm{A}$$

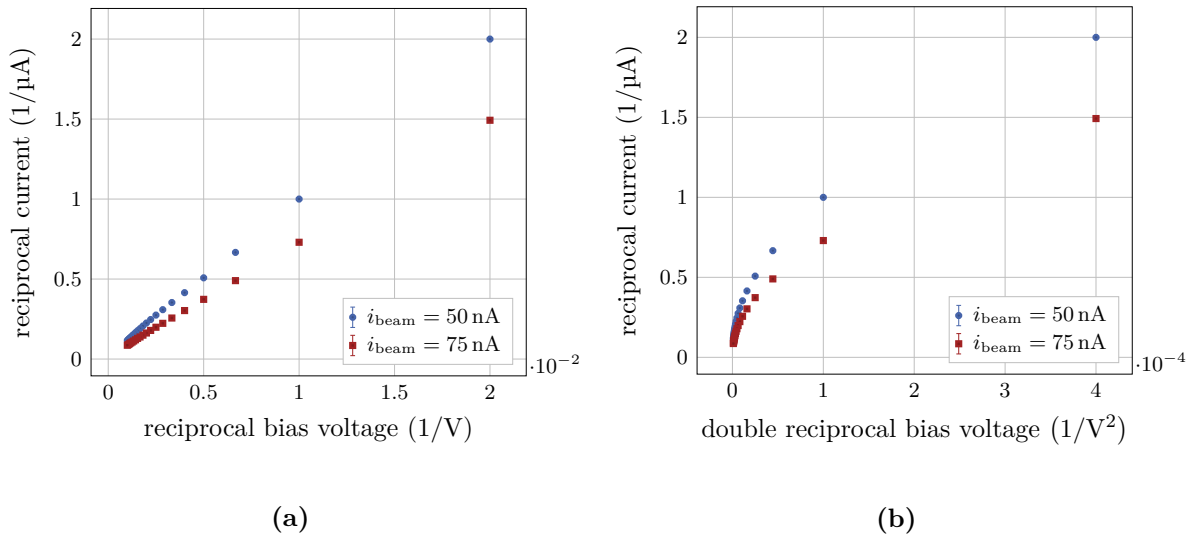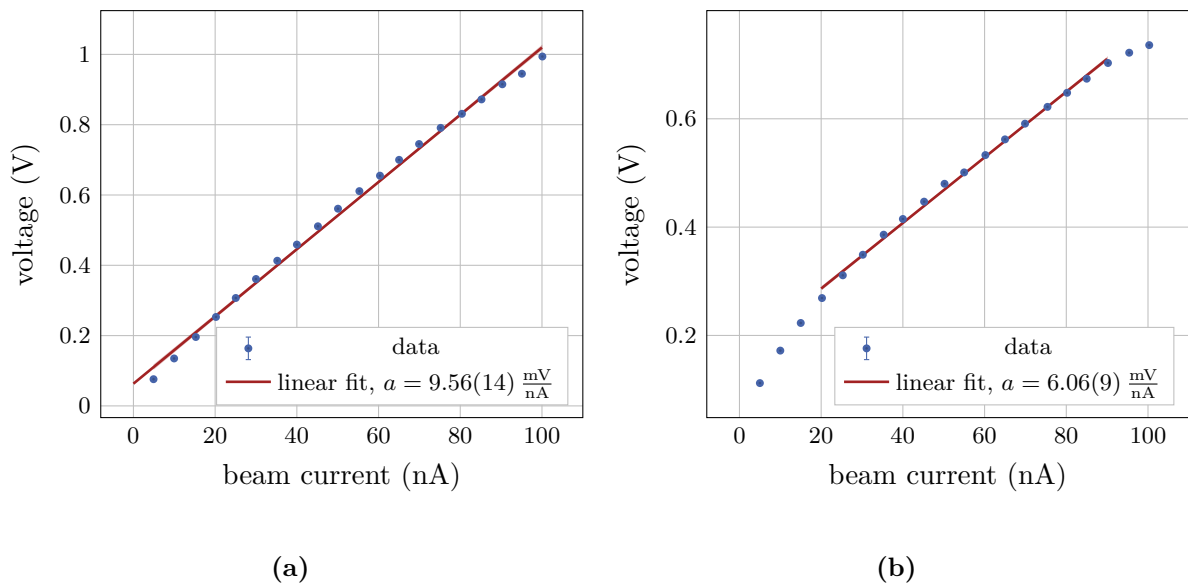**(a)**   **(b)**

Figure 10.9.: Recombination processes for the 8 mm chamber for two different beam currents. The error bars are smaller than the measurement points. a) shows the Jaffé plot. b) shows the $(1/V^2)$-plot. The Jaffé plot is linear, which means that intitial recombination is predominant.

(a)   **(b)**

Figure 10.10.: Beam current scans for both chambers At a bias voltage of 1000 V. a) shows a scan for the 3 mm chamber. b) shows a scan for the 8 mm chamber.

(a)

(b)
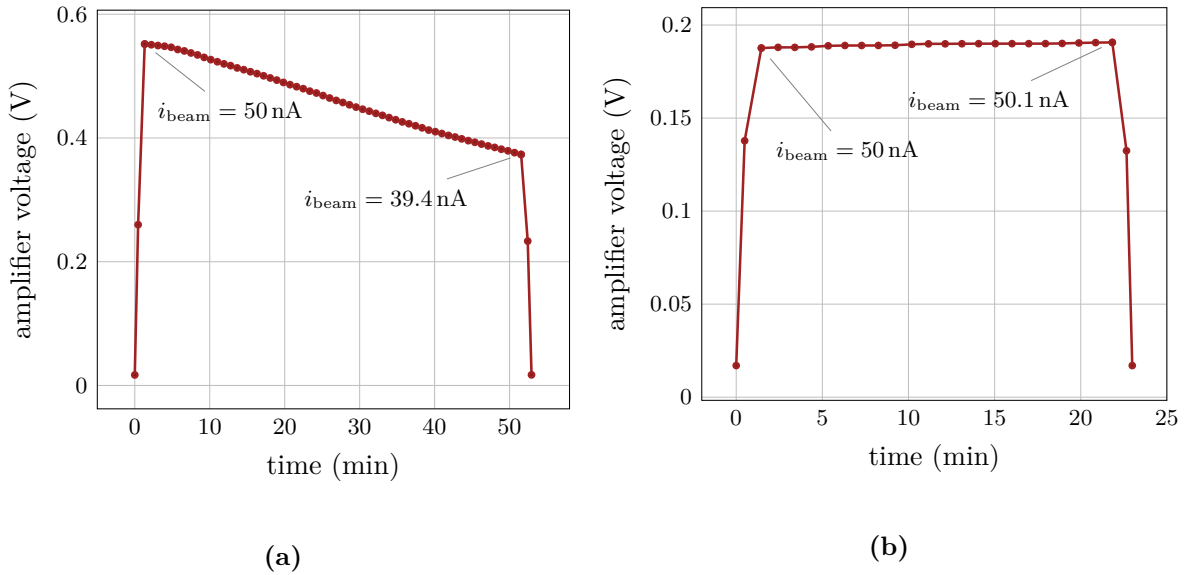
Figure 10.11.: Long term tests For a beam current of 50 nA. a) shows the test for the 3 mm chamber. A bias voltage of 1000 V was used. b) shows the test for the 8 mm chamber. Because of a failure seen with the 3 mm chamber, a lower bias voltage of 300 V was used for the 8 mm chamber.

can be calculated from the amplifier voltage response. This is close to the ideally expected ion current of 20.57 µA (see section 9.3). Including the effects of initial ion recombination and operation of the chamber in the recombination region, this result seems satisfactory.

The 8 mm chamber only exhibits a behavior that resembles linearity in a selected region. Since the collected charges are significantly lower than the expectation (and than the charges collected with the 3 mm chamber for a given beam current), it is concluded that the electric field is substantially lower than the saturation field strength E_{sat}. Being operated in a highly non-saturated region as well as an increased recombination rate discourage from usage of a chamber with this active width. For the sake of brevity, plots showing the intensity scan of the 8 mm chamber at a bias voltage of 300 V are included in appendix A.

In theory, the recorded curves could be used as calibration curves for both chambers. This would require a careful calibration for every chamber that will be used at the beamline. However, operating the chambers in the saturation region would reduce the sensitivity of the device to recombination effects and thus atmospheric effects such as air humidity and temperature. Future designs should try to reduce the active width of the ionization chamber to ensure operation in the saturation region.

Long Term Test

To test the online beam monitor in practice, long term tests are conducted. The beam current is adjusted to 50 nA and the chambers are read out over time. At the start and ending of the measurement periods, reference measurements with a faradey cup are conducted. During operation of the beam, both chambers show a voltage response to the beam current. Turn on rises and turn off falls are visible.

Figure 10.11b shows the long term test for the 8 mm chamber. The beam current was stable over the course of approximately 23 min of operation. Both the initial beam current as well as the final beam current are in accordance with the expected voltage response when compared to the calibration curve in fig. 10.10b.

Figure 10.12.: Visual inspection of the 3 mm chamber after the long term measurement. A deteriorated spot on one electrode is visible. It compromised the charge collection efficiency of the chamber significantly.

Figure 10.11a shows the long term test for the 3 mm chamber. It is easy to see that the beam current continously decreased from 50 nA to 39.4 nA during the course of approximately 50 min. The faradey cup reference measurement at the ending of the measurement period confirms that the beam current, indeed, decreased drastically. The initial beam current i_{beam} is in accordance with the expected voltage response when compared to the calibration curve in fig. 10.10a. The voltage response to the final beam current of 39.4 nA is expected to be 0.45 V. However, in the long term test, a voltage response of 0.37 V is measured. This can be explained by a fault with the 3 mm chamber that has been discovered after this long term measurement.

After the long term measurement was recorded, the chamber is removed from the irradiation box and inspected visually. This is shown in fig. 10.12. A deteriorated spot is visible on one electrode of the chamber which compromised the charge collection efficiency of the chamber significantly. It can safely be assumed that the spot emerged during the course of the long term measurement and not before because the voltage response to the intital beam current was as expected. It was only until after the long term measurement that the reference measurement was not in accordance with the voltage response anymore. To protect the 8 mm preemptively, a lower bias voltage has been selected for its long term test. No issues arised with this chamber. However it should be noted that the measurement period was significantly shorter and that the electrodes are further apart. At the moment, no explanation can be found for this failure. Future irradiation tests need to reproduce the issue and compensate for it.

In summary, long term tests have been successful in giving an online feedback about the beam current. A technical fault has to be investigated further.

11
Summary and Outlook

An ionization chamber for online beam monitoring has been designed. To read out the generated ion current, a two-staged transimpedance amplifier circuit has been designed. To calculate the expected ionization current a proton beam with an energy of 23 MeV would generate, a SRIM simulation was utilized. Consequently, resistor values of the circuit have been determined using a SPICE simulation.

The ionization chamber was tested at two different irradiation facilities. Both amplifier revisions (Rev. B and Rev. C) were characterized with a constant current source injecting a test current that should simulate the ion current. X-ray irradiation was conducted using the X-ray tube that is present at ETP. Revision B of the amplifier is employed to characterize the produced ionization chamber ICv2 in response to an X-ray beam with tube currents of up to 30 mA. For alignment and interfacing purposes, a characterization support structure has been constructed for use with the X-ray setup at ETP. Both examined ionization chambers saturate at a bias voltage of approximately 220 V and show a linear response to an X-ray current at a constant bias voltage of 350 V.

Proton irradiation was conducted at the CMS beamline of the CYRCé cyclotron at IPHC, Strasbourg. Two chambers with active widths of 3 and 8 mm were examined. Revision C of the amplifier was employed to characterize the produced ionization chamber ICv3 in response to a proton beam with beam currents of up to 100 nA. Both examined ionization chambers did not saturate up to a bias voltage of 1000 V and the 3 mm chamber showed a linear response to a proton beam at a constant bias voltage of 1000 V. The electric field of the 8 mm chamber was too low to saturate the chamber sufficiently and only exhibited a linear behavior within a selected beam current region. Columnar recombination was qualitatively characterized for both chambers. Long term testing of a set beam current over time was carried out. Both chambers performed well, however, the 3 mm was visibly damaged after 50 min of testing.

The results that have been obtained are promising. Future iterations of the ionization chamber should aim for improvements with regard to handling, electrical connection and robustness. Either guarding structures or lower active widths seem like reasonable design choices to investigate. Revision D of the amplifier circuit should aim for variable gain factors by implementation of various measurement ranges that are selectable by the user.
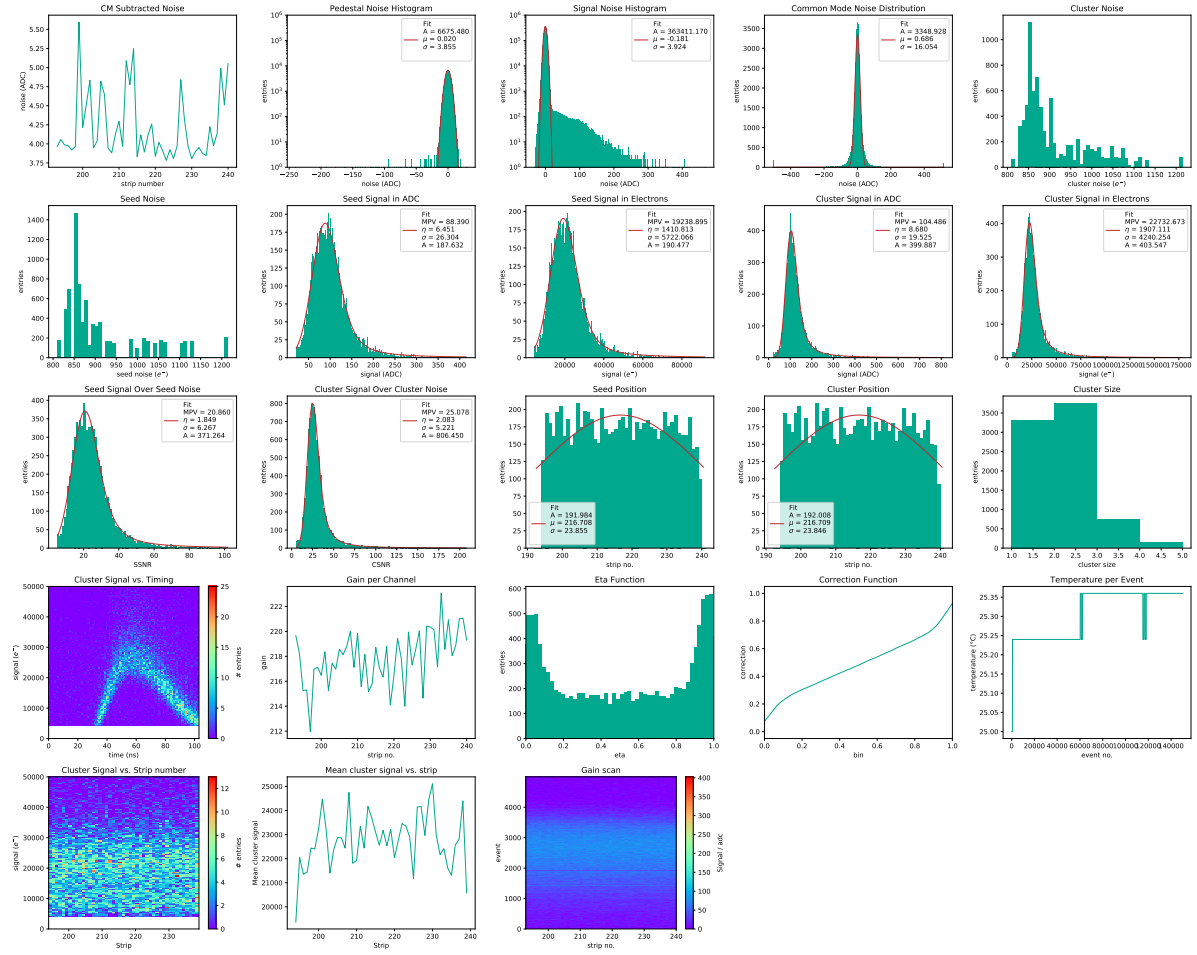
A

Appendix

Figure A.1.: Exemplary output plot generated by `alibava-analysis`. This summary plot was generated from data acquired with a Babysensor at a bias voltage of 500 V at room temperature. An uncollimated Sr-90 source was positioned in front of the sensor under test.
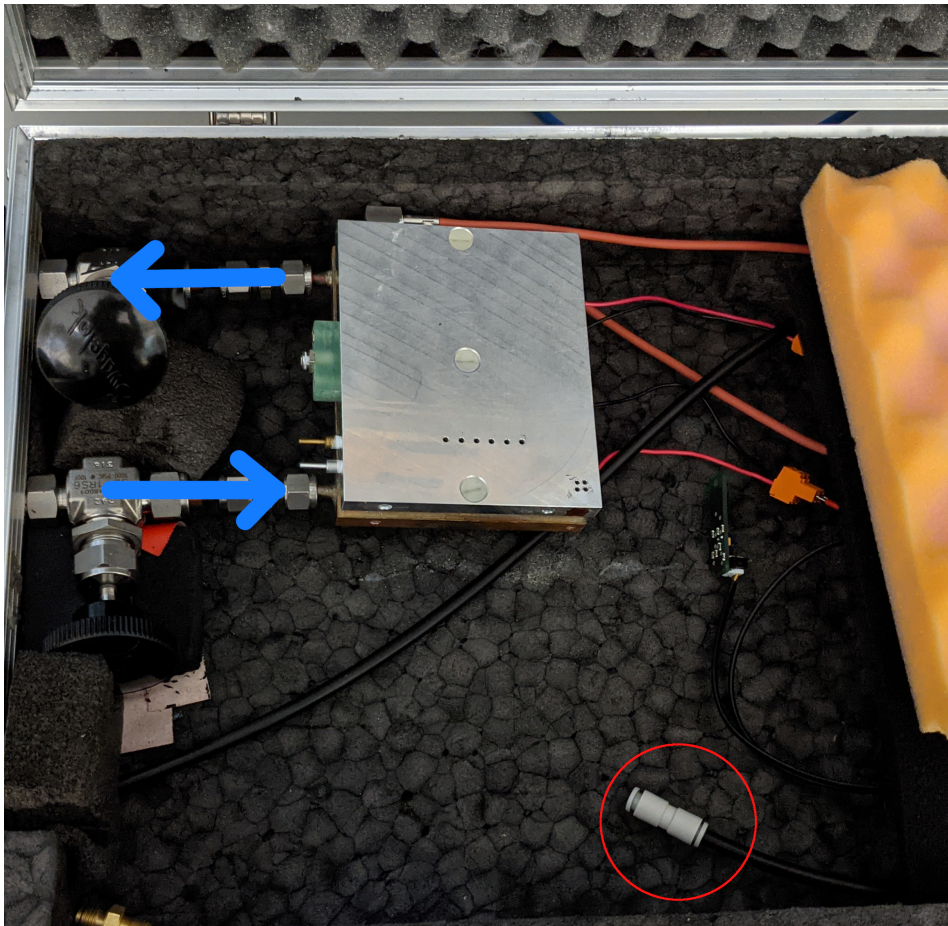
Figure A.2.: Experimental setup for thermal cycles with the PPA mockup. Blue
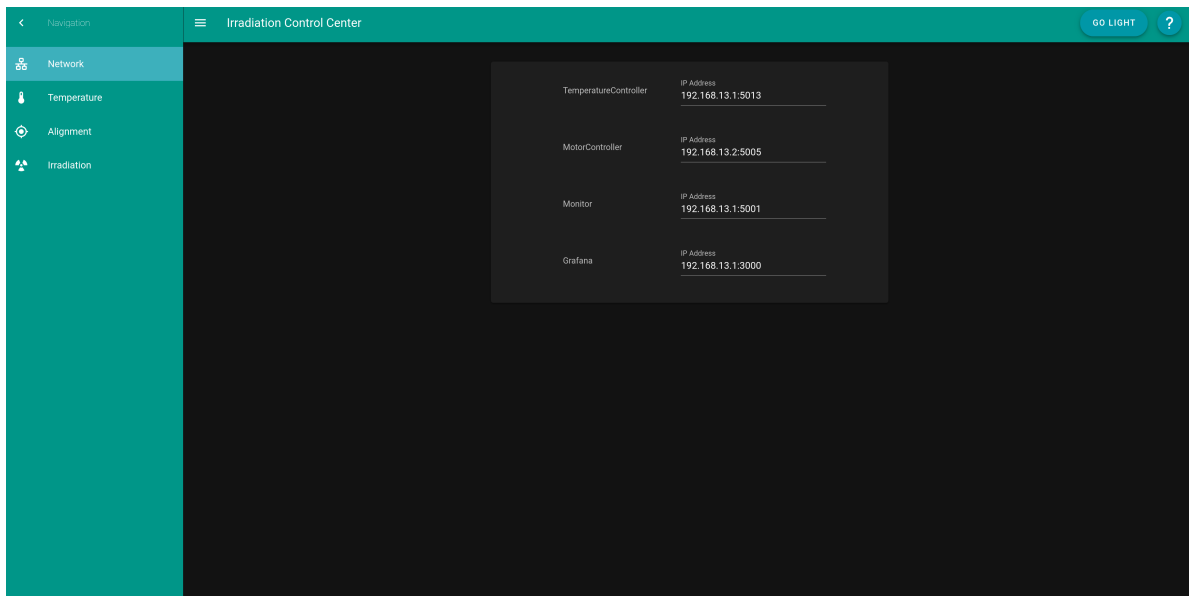arrows indicate the flow of liquid coolant. A red circle marks a dry air inlet.

Figure A.3.: Network tab of the Irradiation Interface. IP addresses that need to be
configured may be entered in the form and will be stored as session-wide cookies.
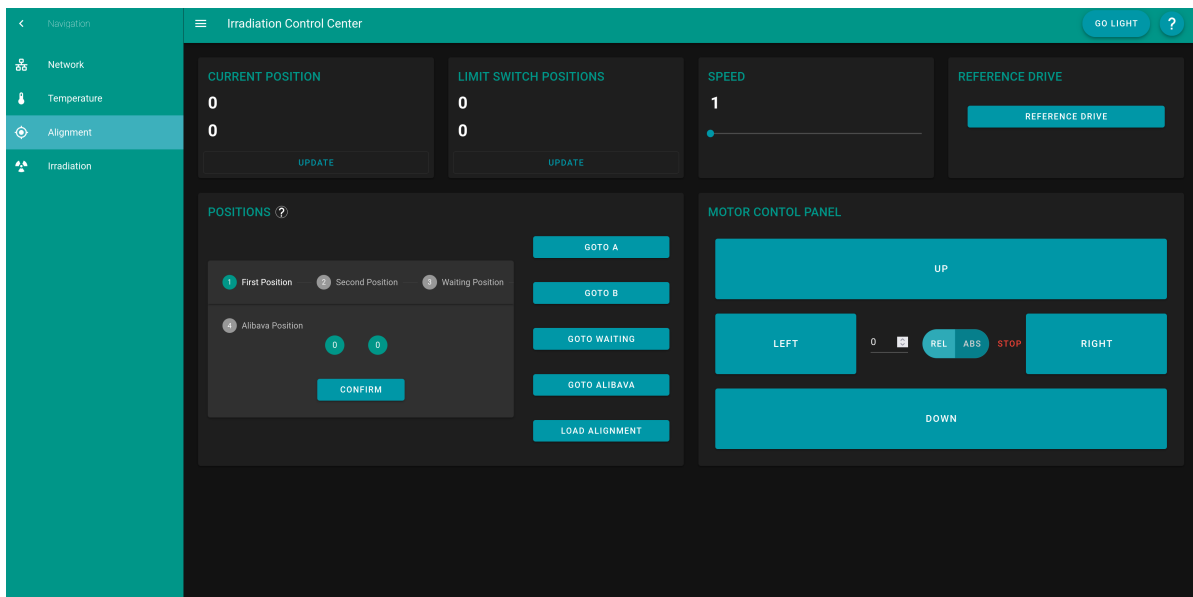
Figure A.4.: Alignment tab of the Irradiation Interface. Motor control and reference drives can be performed using the provided controls. Relevant positions can be stored and loaded from a local file (specified in the back end application).

Bibliography

[ABB20]   W. Adam, T. Bergauer, and D. Blöch. *Experimental study of different silicon sensor options for the upgrade of the CMS Outer Tracker*. In: 15.04 (Apr. 2020), P04017–P04017. DOI: 10.1088/1748-0221/15/04/p04017 (cited on p. 6).

[ALi21]   ALiBaVa Systems. *Alibava Systems Instruments for Detection*. Visited: 22.09.2021. 2021. URL: https://alibavasystems.com/ (cited on p. 11).

[Ans21]   Ansys Inc. *Ansys Engineering Simulation Software*. Visited: 22.09.2021. 2021. URL: https://www.ansys.com/ (cited on p. 16).

[Bou+19] E. Bouquerel et al. *Transverse beam emittance studies of the CYRCé TR24 cyclotron*. In: Nuclear Instruments and Methods in Physics Research A 931 (July 2019), pp. 151–157. DOI: 10.1016/j.nima.2019.04.028 (cited on p. 14).

[Chi13]   A. Chilingarov. *Generation current temperature scaling*. Tech. rep. Lancaster University, UK, Jan. 30, 2013. URL: https://cds.cern.ch/record/1511886 (cited on p. 27).

[CMS18]   CMS Collaboration. *The Phase-2 Upgrade of the CMS Tracker*. Tech. rep. CERN-LHCC-2017-009. CMS-TDR-014. CERN, Apr. 16, 2018. URL: https://cds.cern.ch/record/2272264 (cited on pp. 4–7).

[Dem16]   W. Demtröder. *Experimentalphysik 3*. Springer Berlin Heidelberg, 2016. DOI: 10.1007/978-3-662-49094-5 (cited on pp. 19, 20).

[Die03]   A. Dierlamm. *Untersuchungen zur Strahlenhärte von Silizium- Sensoren*. Karlsruhe Institute of Technology (KIT), 2003 (cited on pp. 14, 15, 48).

[Eli19]   U. Elicabuk. *Charakterisierung von n-in-p Streifensensoren für das Phase-2-Upgrade des CMS-Detektors*. Karlsruhe Institute of Technology (KIT), 2019 (cited on p. 36).

[EN20]   U. Elicabuk and A. Nürnberg. *alibava-analysis*. 2020. URL: https://git.scc.kit.edu/zv9408/alibava-analysis (cited on p. 13).

[Eve]   N. P. for Everybody. *Operating Regions of Ionizing Detectors – Detector Voltage*. URL: https://www.nuclear-power.com/nuclear-engineering/radiation-detection/gaseous-ionization-detector/operating-regions-of-ionizing-detectors-detector-voltage (cited on p. 62).

[Eve20]   L. Everredtronics. *Thermoelectric Module: TEC1-12705T125*. Shanghai: Everredtronics Ltd., 2020. URL: http://www.everredtronics.com/files/TEC1-12705T125_40x40x3.9mm.pdf (cited on p. 40).

[Fur05]   A. Furgeri. *Qualitätskontrolle und Bestrahlungsstudien an CMS Siliziumstreifensensoren*. Karlsruhe Institute of Technology (KIT), 2005 (cited on p. 14).

[Gil+92] K. Gill et al. *Radiation damage by neutrons and photons to silicon detectors*. In: Nucl. Instrum. Meth. A 322 (1992), pp. 177–188. DOI: 10.1016/0168-9002(92)90027-2 (cited on p. 33).

[Goe20]   U. Goerlach. *Test-beam and irradiation facility at the 25 MeV proton cyclotron CYRCé at Strasbourg*. 2020. URL: https://indico.cern.ch/event/813822/contributions/3648330/attachments/1975935/3288811/CYRCe-27-1-2020-UG_final.pdf (cited on p. 15).

[Gut+12] M. Guthoff et al. *Geant4 simulation of a filtered X-ray source for radiation damage studies*. In: Nuclear instruments & methods in physics research / A 675.118 - 122 (Aug. 2012), 10.1016/j.nima.2012.01.029. URL: https://doi.org/10.1016/j.nima.2012.01.029 (cited on pp. 10, 70).

[Har17] F. Hartmann. *Evolution of Silicon Sensor Technology in Particle Physics*. 2nd ed. Springer, Nov. 3, 2017. ISBN: 978-3-319-64434-9. DOI: 10.1007/978-3-319-64436-3 (cited on pp. 23–25, 29, 30, 34).

[IPH14] IPHC. *Présentation générale de Cyrcé*. Visited: 22.09.2021. 2014. URL: http://www.iphc.cnrs.fr/Presentation-generale.html (cited on p. 14).

[Jaf40] G. Jaffé. *On the Theory of Recombination*. In: Phys. Rev. 58 (11 Dec. 1940), pp. 968–976. DOI: 10.1103/PhysRev.58.968 (cited on p. 63).

[KW16] H. Kolanoski and N. Wermes. *Teilchendetektoren: Grundlagen und Anwendungen*. Springer, 2016. ISBN: 978-3-662-45349-0, 978-3-662-45350-6. DOI: 10.1007/978-3-662-45350-6 (cited on p. 21).

[LS06] S. Löchner and M. Schmelling. *The Beetle Reference Manual - chip version 1.3, 1.4 and 1.5*. Geneva: CERN, Nov. 2006. URL: https://cds.cern.ch/record/1000429 (cited on p. 12).

[Met20] M. Metzler. *Irradiation studies on n-in-p silicon strip sensors in the course of the CMS Phase-2 Outer Tracker Upgrade*. Karlsruhe Institute of Technology (KIT), 2020 (cited on p. 12).

[MFL00] M. Moll, E. Fretwurst, and G. Lindström. *Investigation on the improved radiation hardness of silicon detectors with high oxygen concentration*. In: Nuclear Instruments and Methods in Physics Research Section A: Accelerators, Spectrometers, Detectors and Associated Equipment 439.2 (2000), pp. 282–292. ISSN: 0168-9002. DOI: https://doi.org/10.1016/S0168-9002(99)00842-6 (cited on p. 32).

[Mob19] E. Mobs. *The CERN accelerator complex - 2019. Complexe des accélérateurs du CERN - 2019*. In: (July 2019). General Photo. URL: https://cds.cern.ch/record/2684277 (cited on p. 3).

[Mol99] M. Moll. *Radiation Damage in Silicon Particle Detectors*. PhD thesis. University of Hamburg, 1999. URL: https://mmoll.web.cern.ch/mmoll/thesis/ (cited on pp. 29–31, 33, 34).

[Nür18] Nürnberg, A. and Schell, D. *Measurement Control 0.1 documentation*. Visited: 22.09.2021. 2018. URL: http://cms-ka.fzk.de/software/MeasurementControlDocumentation/auto/index.html (cited on p. 11).

[PHS14] D. Pohl, T. Hemperek, and H. Schreiner. *pylandau*. 2014. URL: https://github.com/SiLab-Bonn/pylandau (cited on p. 14).

[Ram39] S. Ramo. *Currents Induced by Electron Motion*. In: Proceedings of the IRE 27.9 (1939), pp. 584–585. DOI: 10.1109/jrproc.1939.228757 (cited on p. 26).

[Sho38] W. Shockley. *Currents to Conductors Induced by a Moving Point Charge*. In: Journal of Applied Physics 9.10 (1938), pp. 635–636. DOI: 10.1063/1.1710367 (cited on p. 26).

[Tri21] Trinamic. *PD42-x-1140*. 2021. URL: https://www.trinamic.com/products/drives/details/pd42-x-1140 (cited on p. 37).

[Vla21] Vladimirescu, A. and Zhang, K. and Newton, A. R. and Pederson, D. O. *The SPICE Circuit Simulator*. 2021. URL: https://www.eecg.utoronto.ca/~johns/spice/part1.html#1 (cited on p. 64).

[Wun92]   R. Wunstorf. *Systematische Untersuchungen zur Strahlenresistenz von Silizium-Detektoren für die Verwendung in Hochenergiephysik-Experimenten.* Notional starting date. The scanned file is too big to be uploaded; University of Hamburg, Diss., 1992. Dr. Hamburg: University of Hamburg, 1992. URL: `https://bib-pubdb1.des y.de/record/153817` (cited on p. 33).

[Zha19]   F. Zhang. *Development of the CMS Phase-1 Pixel Online Monitoring System and the Evolution of Pixel Leakage Current.* In: Journal of Instrumentation 14 (May 2019), pp. C05008–C05008. DOI: `10.1088/1748-0221/14/05/C05008` (cited on p. 35).

[Zie]   J. F. Ziegler. *SRIM Introduction.* URL: `http://www.srim.org/SRIM/SRIMINTRO.h tm` (cited on p. 64).

Danksagungen